2-4-2015

Coherent Digital Holographic Adaptive Optics

Changgeng Liu
University of South Florida, changgengliu@mail.usf.edu

Coherent Digital Holographic Adaptive Optics

by

Changgeng Liu

A dissertation submitted in partial fulfillment
of the requirements for the degree of
Doctor of Philosophy
Department of Physics
College of Arts and Sciences
University of South Florida

Major Professor: Myung K. Kim, Ph.D.
David Richards, Ph.D.
Martin Muschol, Ph.D.
Andreas Muller, Ph.D.

Date of Approval:
February 4, 2015

Keywords: Aberration sensing, Wavefront correction, Confocal imaging, Scanning imaging, Ophthalmoscope.

Dedication

To my wife and my parents

Acknowledgments

I would first like to express my great gratitude to my thesis advisor Prof. Myung K. Kim. He is first a very nice and helpful instructor. His lectures on electromagnetism could not be clearer. As a researcher, he has demonstrated his devotion, his creativity and far vision during his development of incoherent digital holography and adaptive optics by this technique. As my thesis advisor, his patience in guiding, his vision in the trend of the research field and his strictness in technical presentations leave a deep mark in my mind and will benefit me in the future while continuing my research interest. Without his guidance, this dissertation is far from possible.

I would like to thank Prof. David Richards for serving as my committee member, for his advice throughout this project and his generosity of lending me books on the ophthalmology and optometry. I would also like to thank Prof. Martin Muschol and Prof. Andreas Muller for their time and patience in serving as my committee members, attending my technical presentations and reading my dissertation. Dr. Bin Xue is kind enough to chair my dissertation defense. I really appreciate his help.

I would like to thank Dr. Stefano Marchesini at Lawrence Berkeley National Laboratory for teaching me x-ray optics and phase retrieval algorithms. His work on Ptychography encouraged me to try digital line-scanning confocal imaging system.

I would like to thank my colleague David Clark for his help in mechanical stuff and movies he share with me. I would also like to thank former members of our lab, Xiao Yu and

Jisoo Hong for the joy they brought to me, and thank my other numerous friends for their help and the fun we have together. My gratitude also goes to the department staff members Daisy, Candice, Luisa, and Mary Ann for their help throughout my Ph.D. career.

My parents deserve my deep appreciation for their constant support and encouragement on whatever I pursue. I hope I will not let them down. My sister and my bother-in-law are always the ones I can count on to help take care of the family. I very much appreciate their support.

Finally, too much gratitude is owed to my wife Kankan. Her encouragement when I am stuck, her constant support when I am on a new mission, her pushing when I am lazy and her happiness when I achieve something have become and will always be the driving force behind me.

Table of Contents

List of Figures

Abstract

A new type of adaptive optics (AO) based on the principles of digital holography (DH) is proposed and developed for the use in wide-field and confocal retinal imaging. Digital holographic adaptive optics (DHAO) dispenses with the wavefront sensor and wavefront corrector of the conventional AO system. DH is an emergent imaging technology that gives direct numerical access to the phase of the optical field, thus allowing precise control and manipulation of the optical field. Incorporation of DH in an ophthalmic imaging system can lead to versatile imaging capabilities at substantially reduced complexity and cost of the instrument. A typical conventional AO system includes several critical hardware pieces: spatial light modulator, lenslet array, and a second CCD camera in addition to the camera for imaging. The proposed DHAO system replaces these hardware components with numerical processing for wavefront measurement and compensation of aberration through the principles of DH.

We first design an image plane DHAO system which is basically simulating the process the conventional AO system and replacing the hardware pieces and complicated control procedures by DH and related numerical processing. In this original DHAO system, CCD is put at the image plane of the pupil plane of the eye lens. The image of the aberration is obtained by a digital hologram or guide star hologram. The full optical field is captured by a second digital hologram. Because CCD is not at the conjugate plane of the sample, a numerical propagation is necessary to find the image of the sample after the numerical aberration compensation at the CCD plane. The theory, simulations and experiments using an eye model have clearly

demonstrated the effectiveness of the DHAO. This original DHAO system is described in Chapter 2.

Different from the conventional AO system, DHAO is a coherent imaging modality which gives more access to the optical field and allows more freedom in the optical system design. In fact, CCD does not have to be put at the image plane of the CCD. This idea was first explored by testing a Fourier transform DHAO system (FTDHAO). In the FTDHAO, the CCD can directly record the amplitude point spread function (PSF) of the system, making it easier to determine the correct guide star hologram. CCD is also at the image plane of the target. The signal becomes stronger than the image plane DHAO system, especially for the phase aberration sensing. Also, the numerical propagation is not necessary. In the FTDHAO imaging system, the phase aberration at the eye pupil can be retrieved by an inverse Fourier transform (FT) of the guide star hologram and the complex amplitude of the full field optical field at the eye pupil can be obtained by an inverse FT of the full field hologram. The correction takes place at the eye pupil, instead of the CCD plane. Taking FT of the corrected field at the eye pupil, the corrected image can be obtained. The theory, simulations, and experiments on FTDHAO are detailed in chapter 3.

The successful demonstration of FTDHAO encourages us to test the feasibility of putting CCD at an arbitrary diffraction plane in the DHAO system. Through theoretical formulation by use of paraxial optical theory, we developed a correction method by correlation for the general optical system to perform the DHAO. In this method, a global quadratic phase term has to be removed before the correction operation. In the formulation, it is quite surprising to find that the defocus term can be eliminated in the correlation operation. The detailed formulations, related simulations, and experimental demonstrations are presented in Chapter 4.

To apply the DHAO to the confocal retinal imaging system, we first transformed the conventional line-scanning confocal imaging system into a digital form. That means each line scan is turned into a digital hologram. The complex amplitude of the optical field from each slice of the sample and aberration of the optical system can be retrieved by digital holographic process. In Chapter 5, we report our experiments on this digital line-scanning confocal imaging system. This digital line-scanning confocal image absorbs the merits of the conventional line-scanning confocal imaging system and DH. High-contrast intensity images with low coherent noise, and the optical sectioning capability are made available due to the confocality. Phase profiles of the samples become accessible thanks to DH. The quantitative phase map is even better than that from the wide field DH.

We then explore the possibility of applying DHAO to this newly developed digital line-scanning confocal imaging system. Since optical field of each line scan can be achieved by the DH, the aberration contained in this field can be eliminated if we are able to obtain the phase aberration. We have demonstrated that the phase aberration can be obtained by a guide star hologram in the wide field DHAO systems. We then apply this technique to acquire the aberration at the eye pupil, remove this aberration from the optical fields of the line scans and recover the confocal image. To circumvent the effect of phase aberration on the line illumination, a small collimated laser beam is shone on the cylindrical lens. Thus the image is solely blurred by the second passage through the aberrator. This way, we can clearly demonstrate the effect of DHAO on the digital line-scanning confocal image system. Simulations and experiments are presented in chapter 6, which clearly demonstrates the validity of this idea. Since line-scanning confocal imaging system using spatially coherent light sources has proven an effective imaging tool for retinal imaging, the presented digital adaptive optics line-scanning confocal imaging

system is quite promising to become a compact digital adaptive optics laser scanning confocal ophthalmoscope.

Chapter One:

Introduction

1.1 Introduction to Adaptive Optics

The concept of adaptive optics (AO) was first proposed by Babcock to address the distortion caused by the atmospheric turbulence in astronomy [1]. In 1977, Hardy and colleagues successfully demonstrated an adaptive optics system in astronomy [2]. Most of major ground based telescopes are now equipped with AO [3, 4]. Like ground based telescopes, the human eye also suffers from many monochromatic aberrations, due to the irregularity of the cornea and eye lens, which degrade the retinal image quality. To improve the quality of the retinal images, the Shack–Hartmann sensor was first incorporated into an AO system for vision science in 1997 by Liang and colleagues [5]. Retinal images with unprecedented resolution capable of resolving individual photoreceptors were obtained using the AO system. Since then the field of AO in vision science has been rapidly growing with more and more systems being developed [6-11]. Recently, AO system has also been applied in microscopy to reduce the aberrations induced by variations of refractive index through the sample [12]. Using AO system, high-resolution in-depth microscopic images of some biological samples are achieved [13].

A conventional AO system includes several critical hardware pieces: spatial light modulator or deformable mirror, lenslet array and a second CCD camera in addition to the camera for imaging. A flood illumination AO ophthalmoscope is illustrated in Fig.1.1 which is adapted from ref. [7]. A narrow collimated laser beam is sent into the eye and focused at the

retina. This focus spot is termed as guide star. The reflected light from the guide star is then collimated by the eye lens and cornea. Due to the aberration caused by the eye lens and cornea, the output wavefront at the pupil plane is distorted. This aberration can be measured by the Shack–Hartmann wavefront sensor that is put at the conjugate plane of the pupil plane of the eye. With the aberration in hand, the computer then controls the shape of a deformable mirror to cancel this aberration as shown in Fig.1.1. After correction, improved retinal images can be achieved. However, this achievement is obtained at a high price. First, the wavefront sensor is not able to get access to the phase aberration. Instead, an array of shifted spots are captured and evaluated by Zernike fitting procedure [14]. Therefore, the accuracy is hard to guarantee. Second, the deformable mirror consists of several dozens to hundreds segments. The correction can take place at most hundreds locations. Based on these two reasons, a few feedbacks are necessary to compensate for the aberration.

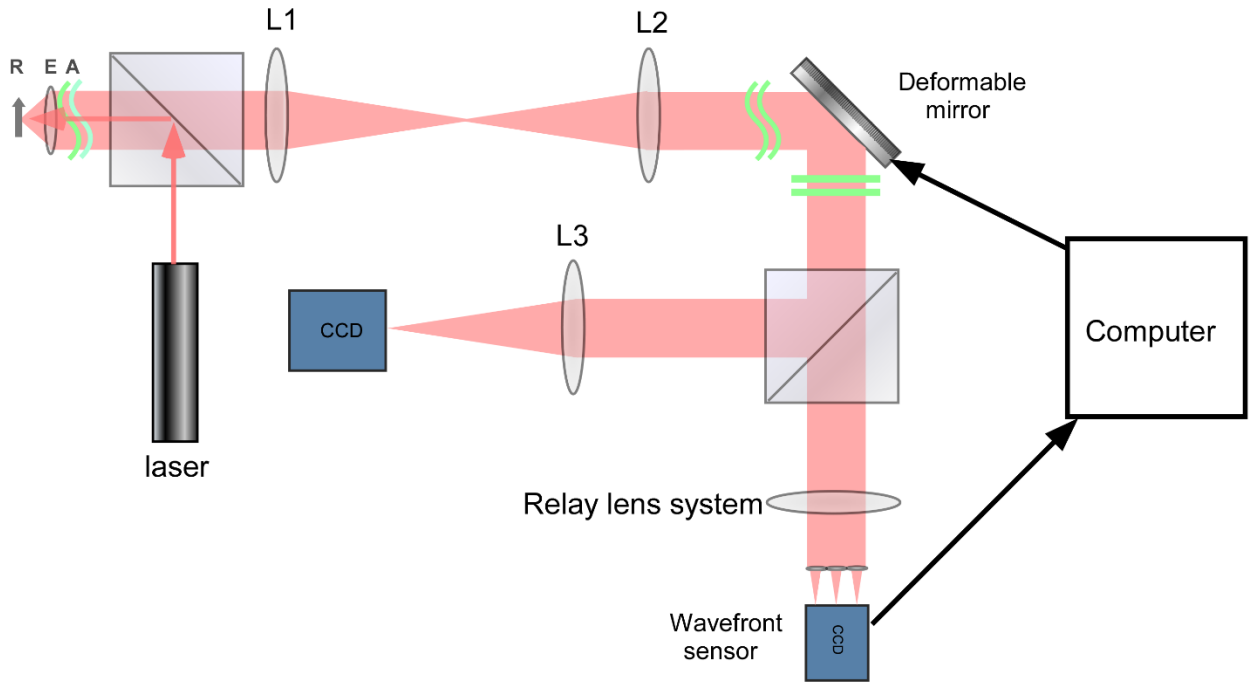

Figure 1.1. Diagram of a flood illumination AO system for ophthalmoscope, adapted from [7]. E: eye lens. R: retina. L1-L3: lens. Relay lens system will image the aberration A on the lenslet of the wavefront sensor.

In this dissertation, we propose a new AO system that dispenses with the wavefront sensor and corrector. These are essential elements of the current AO technology, but they are also the components that require a high degree of delicate alignment and maintenance, constraining the resolution, dynamic range, and speed, as well as driving up the cost. The new system, named digital holographic adaptive optics (DHAO), is based on the ability of digital holography to quantitatively measure and numerically manipulate phase profiles of optical wavefronts [15-17]. It substantially reduces complexity, and very likely the cost, of the optomechanical system. The wavefront sensing and correction by DHAO have almost the full resolution of the CCD camera [15-17]. It does not involve electronic-numerical-mechanical feedback. Numerical computation of holographic images is faster than the conventional AO feedback loop.

The principle of aberration compensation is a well-known characteristics of holography, as clearly demonstrated by Leith and Upatnieks in 1966 [18]. Numerical processing of the complex wavefronts measured by digital holography offers a new level of flexibility and versatility in sensing and control of aberration. Compensation of low-order aberrations, including tilt, spherical aberration, and astigmatism, have been demonstrated in digital holographic microscopy (DHM), either by double exposure of the field with and without the specimen, or by assuming a portion of the object field to be flat [19]. Automatic compensation of higher order terms of the Zernike polynomials has been demonstrated and the concept of numerical parametric lens has been introduced that can shift, magnify, and compensate for aberrations [20].

1.2 Introduction to Digital Holography

The proposed DHAO system is based on the principles of DH. Before we introduce this

system, it is necessary to give a brief introduction of DH. DH can be generally categorized into two classes: off-axis DH and on-axis DH. In the off-axis DH configuration, the optical field from the object and reference beam arrive at the CCD with an angle as shown in Fig.1.2, while in on-axis DH system, the object field and reference field are parallel. Since off-axis DH will be adopted throughout this dissertation, we will present the principle of DH based on off-axis configuration. The readers can consult refs. [21-22] for the details of the on-axis DH.

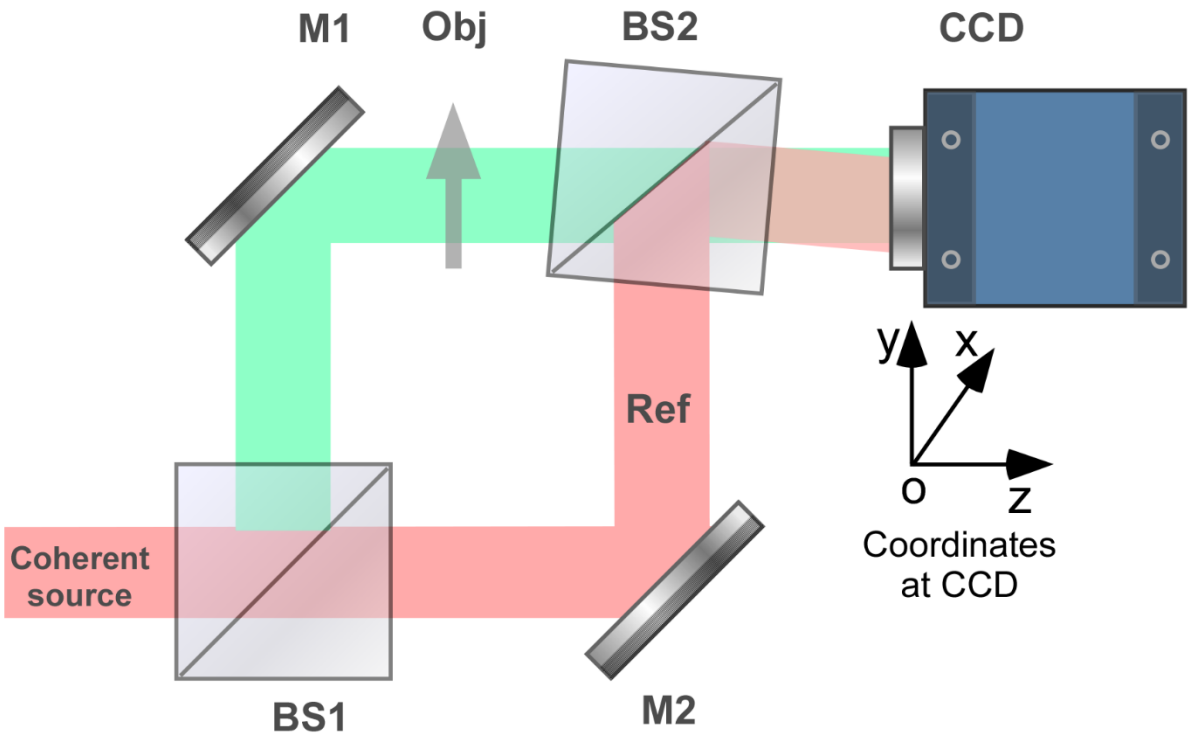

Figure 1.2. The schematic diagram of an off-axis DH setup. BS1-BS2: beamsplitters. M1-M2: mirrors.

Assuming the optical field of the object at the CCD plane is given by

$$O(x,y) = A_o(x,y)\exp[j\varphi_o(x,y)] \tag{1.1}$$

where $A_0(x,y)$ is the amplitude and $\varphi_o(x,y)$ the phase. The collimated reference beam at the CCD plane is assumed to be of the form as

$$
\begin{aligned}
R(x,y) &= A_r(x,y)\exp[j\varphi_r(x,y)] \\
&= \exp[j2\pi(\frac{\cos(\theta_x)}{\lambda}x + \frac{\cos(\theta_y)}{\lambda}y)]
\end{aligned}
\tag{1.2}
$$

where λ is the wavelength of the light source. θ_x and θ_y represent the angles of the wave vector of the reference beam with respect to x and y axis respectively. The off-axis digital hologram captured by the CCD can be given by

$$
\begin{aligned}
H(x,y) &= \left|O(x,y) + R(x,y)\right|^2 \\
&= \left|A_r(x,y)\right|^2 + 1 \\
&\quad + O\exp[-j2\pi(\frac{\cos(\theta_x)}{\lambda}x + \frac{\cos(\theta_y)}{\lambda}y)] \\
&\quad + O^*\exp[j(+2\pi(\frac{\cos(\theta_x)}{\lambda}x + \frac{\cos(\theta_y)}{\lambda}y))]
\end{aligned}
\tag{1.3}
$$

where a global coefficient related to the quantum efficiency of the sensor is ignored. To retrieve the object field O(x,y) from this hologram, a Fourier transform FT) is performed on Eq.(1.3), resulting in the angular spectrum of this hologram as follows,

$$
\begin{aligned}
AS(f_x, f_y) &= FT\{H(x,y)\} \\
&= S(f_x, f_y) \odot S(f_x, f_x) + \delta(f_x, f_y) \\
&\quad + S(f_x + \frac{\cos(\theta_x)}{\lambda}, f_y + \frac{\cos(\theta_y)}{\lambda}) \\
&\quad + S^*(f_x - \frac{\cos(\theta_x)}{\lambda}, f_y - \frac{\cos(\theta_y)}{\lambda})
\end{aligned}
\tag{1.4}
$$

where f_x and f_y are coordinates of spatial frequency, $S(f_x, f_y)$ denotes the FT of the object field O(x,y), and $\odot$ represents correlation operation. From this angular spectrum, the third term can be filtered out and shifted to the center at the spectral plane to obtain $S(f_x, f_y)$, from which the object field can be obtained by performing a FT operation. To illustrate this mathematical process of off-axis DH, we present one simulation example, as shown in Fig. 1.3.

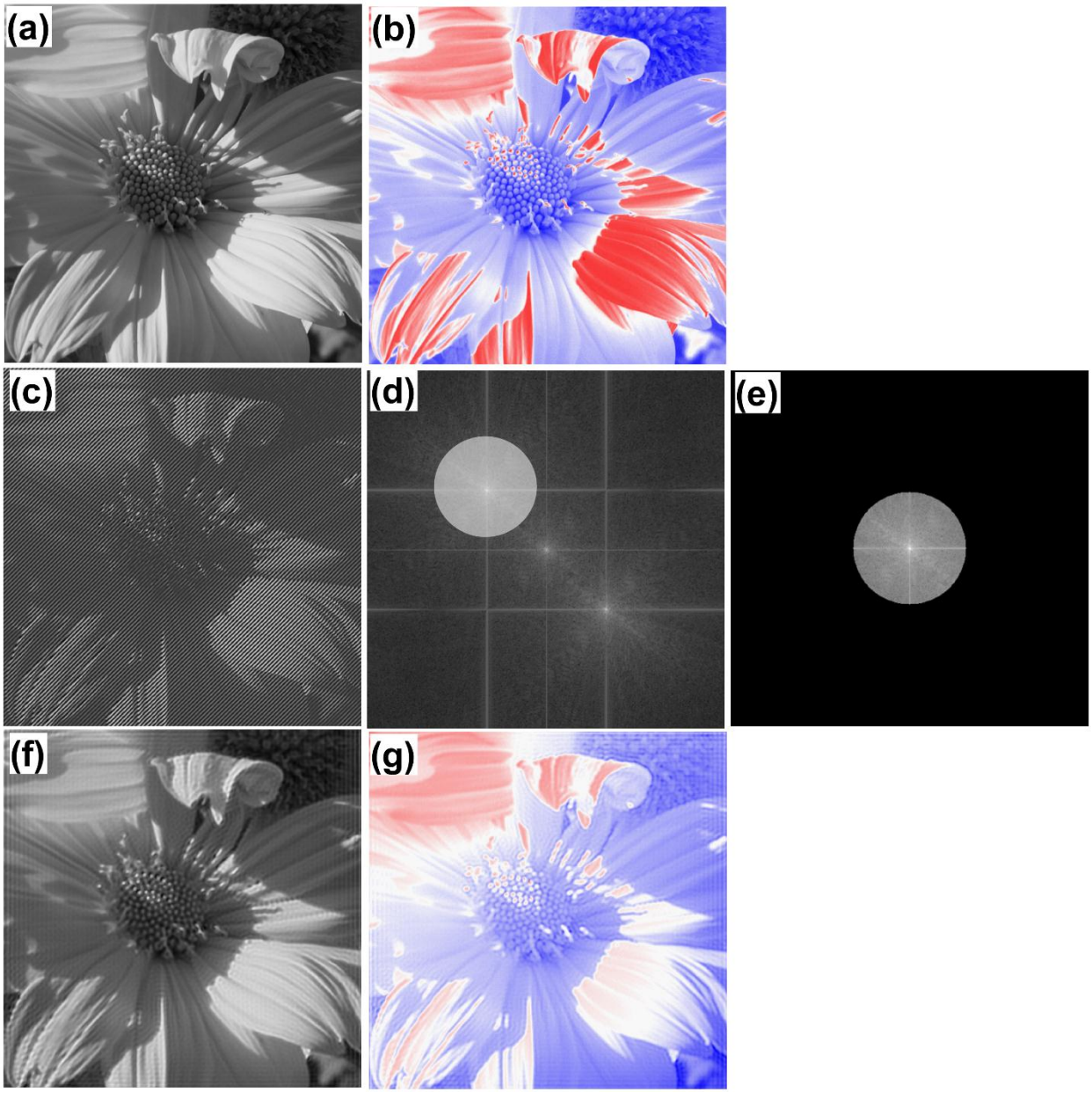

Figure1.3. Demonstration of basic process of off-axis DH. (a) Simulated amplitude. (b) Simulated phase in blue-white-red color map, ranging from $-\pi$ to π. (c) Digital off-axis hologram. (d) Angular spectrum. (e) Filtered image order. (f) Reconstructed amplitude. (g) Reconstructed phase.

Figure 1.3(a) and 1.3(b) show the simulated amplitude and phase of the object field O(x,y). Figure 1.3(c) is the off-axis digital hologram as given by Eq.(1.3), where both θ_x and θ_y are set to be 88°. The angular spectrum of this digital hologram is shown in Fig. 1.3(d), where the highlighted region represents the image order as given by the term

$S(f_x + \frac{\cos(\theta_x)}{\lambda}, f_y + \frac{\cos(\theta_y)}{\lambda})$ in Eq.(1.4). After filtering out and spatially centering this term, we can obtain the FT of the object field as shown in Fig. 1.3(e). Taking inverse FT of the spectrum shown in Fig. 1.3(e), the object field can be reconstructed. The reconstructed amplitude and phase are shown in Figs. 1.3(f) and 1.3(g) respectively.

1.3 Dissertation View

In this dissertation, we first presented the concept of digital holographic adaptive optics(DHAO) which realizes the phase aberration by a digital hologram and aberration correction by numerical processing, thus eliminating the lenslet array for aberration sensing, deformable mirror for wave corrector and complicated control procedures.

We then introduced an image plane DHAO system in which the CCD is put at the image plane of the pupil plane of the eye lens. The image of the aberration is obtained by a digital hologram or guide star hologram. The full optical field is captured by a second digital hologram. Because CCD is not at the conjugate plane of the sample, a numerical propagation is necessary to find the image of the sample after the numerical aberration compensation at the CCD plane. This original DHAO system is described in Chapter 2.

Different from the conventional AO system, DHAO is a coherent imaging modality which gives more access to the optical field and allows more freedom in optical system design. This idea was first explored by testing a Fourier Transform DHAO system (FTDHAO). In the FTDHAO, the CCD can directly record the amplitude point spread function (PSF) of the system, making it easier to determine the correct guide star hologram. The CCD is also put at the image plane of the target. The signal will be stronger than the original image plane DHAO system, especially for the phase aberration sensing. Numerical propagation is not necessary. In the

FTDHAO imaging system, the phase aberration at the eye pupil can be retrieved by the inverse Fourier transform (FT) of the guide star hologram and the complex amplitude of full optical field at the eye pupil can be obtained by the inverse FT of the full field hologram. The correction takes place at the eye pupil, instead of the CCD plane. Taking FT of the corrected field at the eye pupil, the corrected image can be obtained. Numerical propagation is not necessary. The theory, simulations and experiments on FTDHAO are detailed in chapter 3.

The successful demonstration of FTDHAO inspired us to explore the feasibility of putting CCD at an arbitrary diffraction plane in the DHAO system. Through theoretical formulation by use of paraxial optical theory, we developed a correction method by correlation for the general optical system to perform the DHAO. In this method, a global quadratic phase term has to be removed before the correction operation. In the formulation, it is quite surprising to find that the defocus term can be naturally eliminated after the correlation operation. The detailed formulations and related simulation and experimental demonstrations are presented in Chapter 4.

To apply the DHAO to confocal retinal imaging system, we first demonstrate that the conventional line-scanning confocal imaging system can be converted into a digital form. That means each line scan is turned into a digital hologram. The complex amplitude of the optical field from each slice of the sample and aberration of the optical system can be retrieved by digital holographic process. In Chapter 5, we report our experiments on this digital line-scanning confocal imaging system. This digital line-scanning confocal image absorbs the merits of the line-scanning confocal imaging system and DH. High-contrast intensity images with low coherent noise, and the optical sectioning capability are made available due to the confocality. Phase profiles of the samples become accessible thanks to DH.

We then explored the possibility of applying DHAO to this newly developed digital line-scanning confocal system. Since optical field in each line scan can be achieved by the DH, the aberration contained in this field can be eliminated if we are able to obtain the phase aberration. We have demonstrated that the phase aberration can be obtained by a guide star hologram as in the wide field DHAO systems. We then apply this technique to acquire the aberration at the eye pupil, remove this aberration from the optical fields of the line scans and recover the confocal image. To circumvent the effect of phase aberration on the line illumination, a small collimated laser beam is shone on the cylindrical lens. Thus the image is solely blurred by the second passage. This way, we can clearly demonstrate the effect of DHAO on the digital line-scanning confocal image system. Simulations and experiments are presented in chapter 6. A summary and the outline of future work on the basis of this dissertation will be presented in Chapter 7.

1.4 References

1. H.W. Babcock, "The possibility of compensating astronomical seeing," Publ. Astron. Soc. Pac. **65**, 229-236(1953).

2. J.W. Hardy, J. E. Lefebvre, and C. L. Koliopoulos, "Real-time atmospheric compensation," J. Opt. Soc. Am. **67**, 360-369(1977).

3. M. A. van Dam, D. Le Mignant, and B. A. Macintosh, "Performance of the keck observatory adaptive optics system," Appl. Opt. **43**, 5458-5467(2004).

4. M. Hart, "Recent advances in astronomical adaptive optics," Appl. Opt. **49**, D17-D29(2010).

5. J. Liang, D. R. Williams, and D. Miller, "Supernormal vision and high-resolution retinal imaging through adaptive optics," J. Opt. Soc. Am. A **14**, 2884-2892(1997).

6. A. Roorda, F. Romero-Borja, W. J. Donnelly III, H. Queener, T. J. Herbert, and M. C. W. Campbell, "Adaptive optics scanning laser ophthalmoscopy," Opt. Express **10**, 405-412 (2002).

7. K. M. Hampson, "Adaptive optics and vision," J. Mod. Opt. **55**, 3425-3467 (2008).

8. I. Iglesias, R. Ragazzoni, Y. Julien, and P. Artal, "Extended source pyramid wave-front sensor for the human eye," Opt. Express **10**, 419-428(2002).

9. N. Doble, G. Yoon, L. Chen, P. Bierden, B. Singer, S. Olivier, and D. R. Williams, "Use of a microelectromechanical mirror for adaptive optics in the human eye," Opt. Lett. **27**, 1537-1539(2002).

10. S. R. Chamot, C. Dainty, and S. Esposito, "Adaptive optics for ophthalmic applications using a pyramid wavefront sensor," Opt. Express **14**, 518-526(2006).

11. Q. Mu, Z. Cao, D. Li and L. Xuan, "Liquid crystal based adaptive optics system to compensate both low and high order aberrations in a model eye," Opt. Express **15**, 946-1953(2007).

12. M. J. Booth, "Adaptive optics in microscopy," Phil. Trans. R. Soc. **A 365**, 2829-2843(2007).

13. M. J. Booth, D. Debarre, and A. Jesacher, "Adaptive optics for biomedical microscopy," Opt. Photonics News **January**, 22-29(2012).

14. J. Z. Liang, B. Grimm, S. Goelz, and J. F. Bille, "Objective measurement of wave aberrations of the human eye with the use of a hartmann-shack wave-front sensor," J. the Opt. Soc. Am. A **11**, 1949-1957 (1994).

15. E. Cuche, P. Marquet, and C. Depeursinge, "Digital holography for quantitative phase-contrast imaging," Opt. Lett. **24**, 291-293 (1999).

16. C. Mann, L. Yu, C. Lo, and M. K. Kim, "High-resolution quantitative phase-contrast microscopy by digital holography," Opt. Express. **13**, 8693-8698 (2005).

17. M. K. Kim, "Principles and techniques of digital holographic microscopy," SPIE Reviews **1**, 1-50 (2010).

18. J. Upatnieks, A. V. Lugt, and E. N. Leith, "Correction of lens aberrations by means of holograms," Appl. Opt. **5**, 589-593 (1966).

19. L. Miccio, D. Alfieri, S. Grilli, P. Ferraro, A. Finizio, L. De Petrocellis, and S. D. Nicola, "Direct full compensation of the aberrations in quantitative phase microscopy of thin objects by a single digital hologram," Appl. Phys. Lett. **90**, 3 (2007).

20. T. Colomb, F. Montfort, J. Kuhn, N. Aspert, E. Cuche, A. Marian, F. Charriere, S. Bourquin, P. Marquet, and C. Depeursinge, "Numerical parametric lens for shifting, magnification, and complete aberration compensation in digital holographic microscopy," J. Opt. Soc. Am. A **23**, 3177-3190 (2006).

21. I. Yamaguchi, and T. Zhang, "Phase-shifting digital holography," Opt. Lett. **22**, 1268-1270(1997).

22. T. Zhang, and I. Yamaguchi, "Three-dimensional microscopy with phase-shifting digital holography," Opt. Lett. **23**, 1221-1223(1998).

Chapter Two:

Image Plane Digital Holographic Adaptive Optics

2.1 Introduction

Imaging of the eye is important both in order to understand the process of vision and to correct or repair any defects in the vision system. Imaging of the eye is also inherently difficult in several respects. For example, the relatively small aperture of the pupil and the low reflectivity of the retina limit the amount of light available for imaging with an external instrument to about $10^{-5} \sim 10^{-3}$ of the input, depending on the wavelength [1]. Highly directional lasers and high sensitivity detectors are used in modern instruments such as a scanning laser ophthalmoscope (SLO) [2] or optical coherence tomography (OCT) [3]. These and conventional fundus cameras provide a macroscopic view of the living retina, but they usually do not have the transverse resolution needed to reveal retinal features on the spatial scale of single cells (~2μm). With typical values of the pupil aperture of 3 mm, retinal distance 22mm, and index of refraction 1.33, the numerical aperture of the eye is less than 0.1, which corresponds to diffraction-limited resolution of 3.3μm at wavelength 0.6μm. The pupil can be dilated to 5 mm or more, but then imperfections, i.e. aberrations, of the cornea and lens prevent diffraction-limited imaging.

Adaptive optics (AO), originally developed for astronomical telescopes, reduces the effect of atmospheric turbulence by measuring the distortion of the wavefront arriving from a point source (guide star) and using the information to compensate for the distortions in the objects to be imaged. When applied to ocular imaging, the “guide star” is provided by a narrow

laser beam focused on a spot on the retina [4]. Most commonly a Shack-Hartmann wavefront sensor is used to measure the wavefront of the reflected light [5]. The wavefront distortion is then compensated for using a wavefront corrector, such as deformable mirror or liquid-crystal spatial light modulator [6]. The sensor and corrector typically have a few hundred elements, allowing for adjustment of a similar number of coefficients in the Zernike aberration polynomials. Several iterations of sensing, computation, and corrections are carried out in a feedback loop to reach a stable state. AO has been incorporated in SLO [7, 8], OCT [9-11], and laser refractive surgery [12].

We propose a new AO system that dispenses with the wavefront sensor and corrector. These are essential elements of the current AO technology, but they are also the components that require a high degree of delicate alignment and maintenance, constraining the resolution, dynamic range, and speed, as well as driving up the cost. The new system, named digital holographic adaptive optics (DHAO), is based on the ability of digital holography to quantitatively measure and numerically manipulate phase profiles of optical wavefronts. The wavefront sensing and correction by DHAO have almost the full resolution of the CCD camera. It does not involve electronic-numerical-mechanical feedback. Numerical computation of holographic images is faster than the conventional AO feedback loop. Dynamic range of deformation measurement is essentially unlimited.

Below, we describe the principle of the proposed DHAO system. Numerical simulation examples are used to illustrate the DHAO process for the particular configuration appropriate for ocular imaging. Proof-of-principle experiments clearly demonstrate the feasibility to compensate the ocular aberrations and significantly improve resolution in a robust and efficient manner. The proposed DHAO represents an imaging capability novel and distinct from currently available

techniques. In this original DHAO system, the sensor is put at the image plane of the pupil. We term it as image plane DHAO (IPDHAO) to be distinct from the DHAO system in the next chapter.

2.2 Principles and Simulations

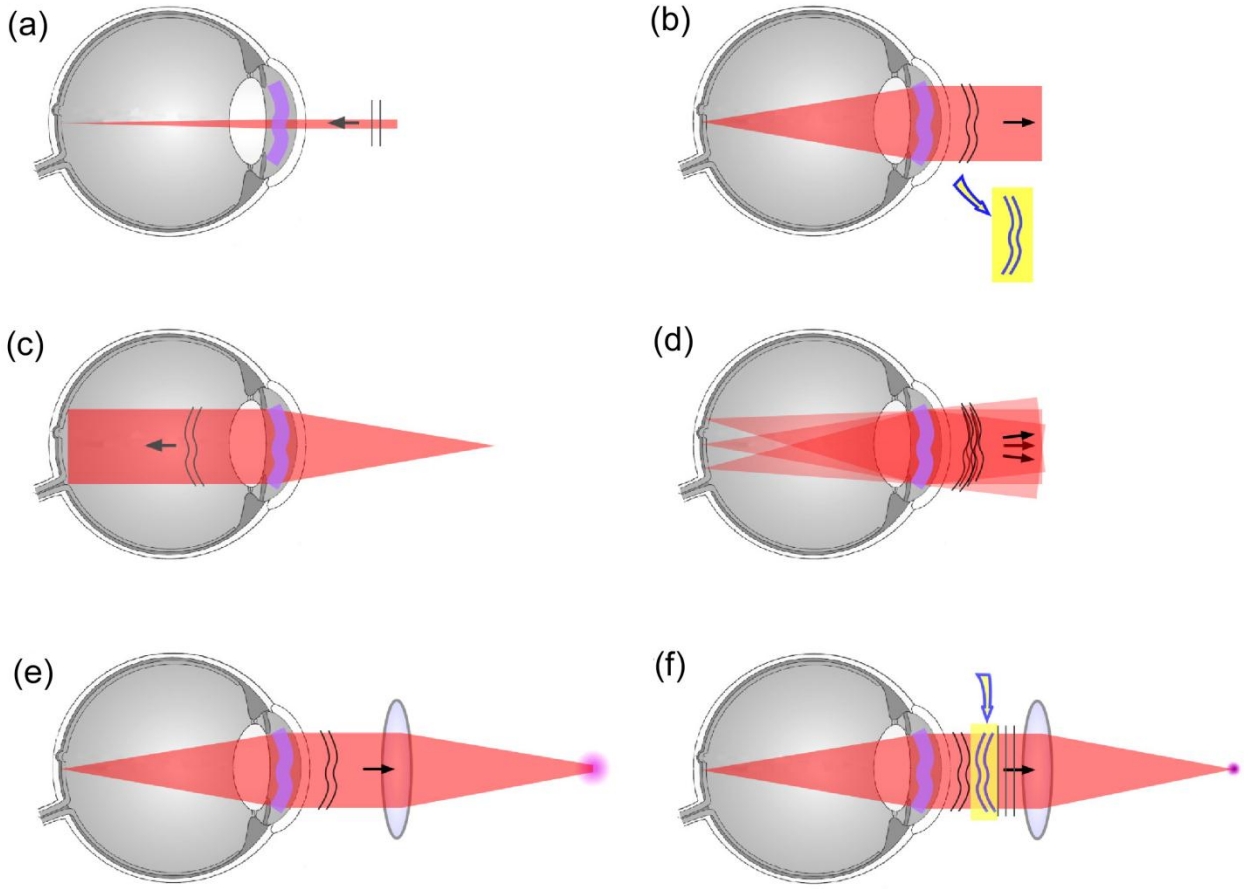

Figure 2.1. IPDHAO principle.

The basic principle of IPDHAO is described using Fig. 2.1. It is a two-exposure process. First, in Fig. 2.1(a), a narrow collimated laser beam enters the eye through the cornea and the lens of the eye, which forms a focused spot on the retina – the so-called "guide star." As noted earlier, diffraction-limited spot size is typically a few micrometers. The light scatters and reflects from the guide star spot and exits the eye with a broad coverage of the cornea and the lens, Fig.

2.1(b). Ideally, the emergent beam would be collimated and its wavefront planar, whereas any aberration of the eye's optics causes distortion of the wavefront. The phase profile of the wavefront is captured by digital holography and numerically stored, as described below in the experimental section. In the second step, for full-field imaging of the retina, a focused source at the front focus of the eyes lens results in a collimated illumination of the retina, Fig. 2.1(c). The illumination does contain phase distortion due to the eye's aberration, but this does not affect the final intensity image of the eye. The complex, i.e. amplitude and phase, optical field exiting the eye is again captured by digital holography at a plane in front of the cornea. The captured complex optical field contains all the information necessary to reconstruct the image of the retina by using a numerical lens and numerically propagating an appropriate distance, Fig. 2.1(e). But the phase distortion degrades the point spread function of the resultant image, which can be compensated for by numerically subtracting the stored phase profile from the first step, Fig. 2.1(f). This description of IPDHAO assumes: i) that the guide star input beam is narrow enough that the aberration across it is negligible; and ii) that most of the aberration is in the anterior region of the eye, i.e. the lens and the cornea, that the aberration experienced by the light from various parts of the retina is approximately equal, see Fig. 2.1(d). Similar assumptions are necessary in the conventional AO, and they are not any more severe in IPDHAO.

The process of IPDHAO is illustrated using the simulation images in Fig. 2.2, where the retinal surface is represented with a resolution target pattern, Fig. 2.2(a). The field is assumed to be $2500 \times 2500 \mu\text{m}^2$ with 512×512 pixels. The retinal surface irregularity is represented with a random phase distribution of the retinal surface, Fig. 2.2(b). The eye is modeled to consist of a lens of focal length 25 mm and the retinal surface located at the focal plane of the lens. The lens is also assumed to contain aberration in the form of phase distortion corresponding to one of the

Zernike polynomials $aZ_5^3(\rho,\varphi) = a\left(5\rho^5 - 4\rho^3\right)\cos 3\varphi$, defined on a circle of radius 2500μm and an amplitude $a = 4\pi$, as depicted in Fig. 2.2(c). In sensing, the amplitude and phase profiles of optical field emerging from a small area of the retina, the guide star, are shown in Fig. 2.2(d) and 2.2(e). It is an approximately plane wave, with phase distortion due to the assumed aberration of the lens and the phase noise of the retina. For imaging, the light enters the eye lens, with aberration, and illuminates the retina, from which it reflects and exits the lens, again with the aberration. The emerging optical field is diffuse with random phase distribution, which can be captured in experiment as a hologram.

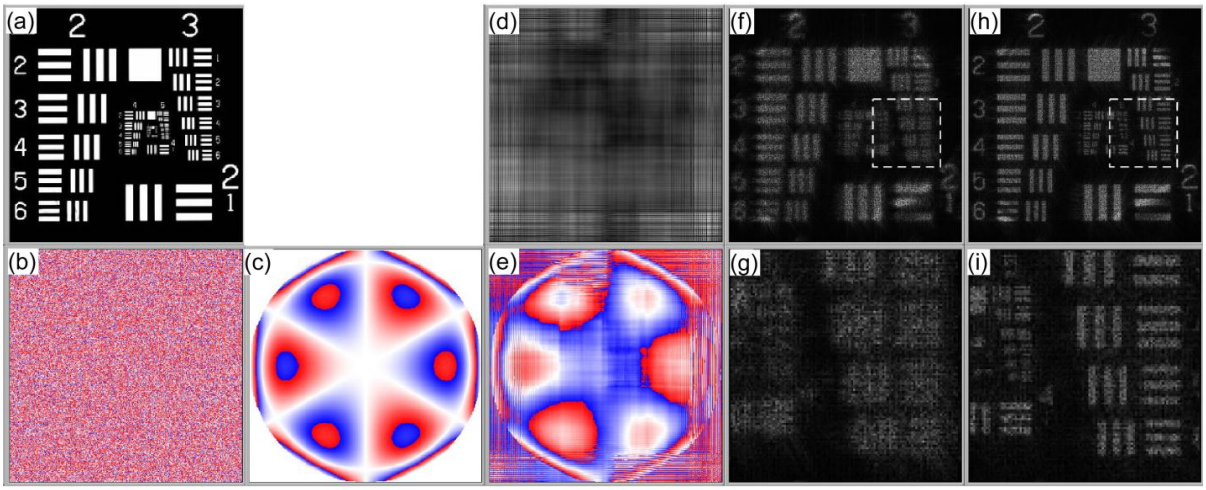

Figure 2.2. Simulation of DHAO process. Amplitude image are shown in gray scale and phase images (b, c, and e) in blue-white-red color scale, representing the range of phase from –π to +π. (a) Assumed amplitude pattern on retina. (b) Phase noise of retinal surface. (c) Assumed aberration of the eye. (d) Amplitude of exit field. (e) Phase of exit field, representing recovered aberration of the eye. (f) Uncorrected image of retina, and (g) its detail. (h) Corrected image of retina, and (i) its detail.

To reconstruct the image of the retina, one can simulate the propagation of light through a numerical lens (e.g., f = 25 mm) and an appropriate distance (z = 25 mm) to the image plane. The resultant image is shown in Fig. 2.2(f), and a magnified view of the dotted square area is shown in Fig. 2.2(g). Now, in order to compensate for the aberration, the aberration field represented in Figs. 2.2(d) and 2.2(e) is conjugated and multiplied to the hologram, before propagating through the imaging lens and to the image plane. The result is shown in Fig. 2.2(h), and a magnified view

of the dotted square area is shown in Fig. 2.2(i). Comparison of Figs. 2.2(f) and 2.2(h), or 2.2(g) and 2.2(i), clearly displays the feasibility of improved resolution.

2.3 Optical System

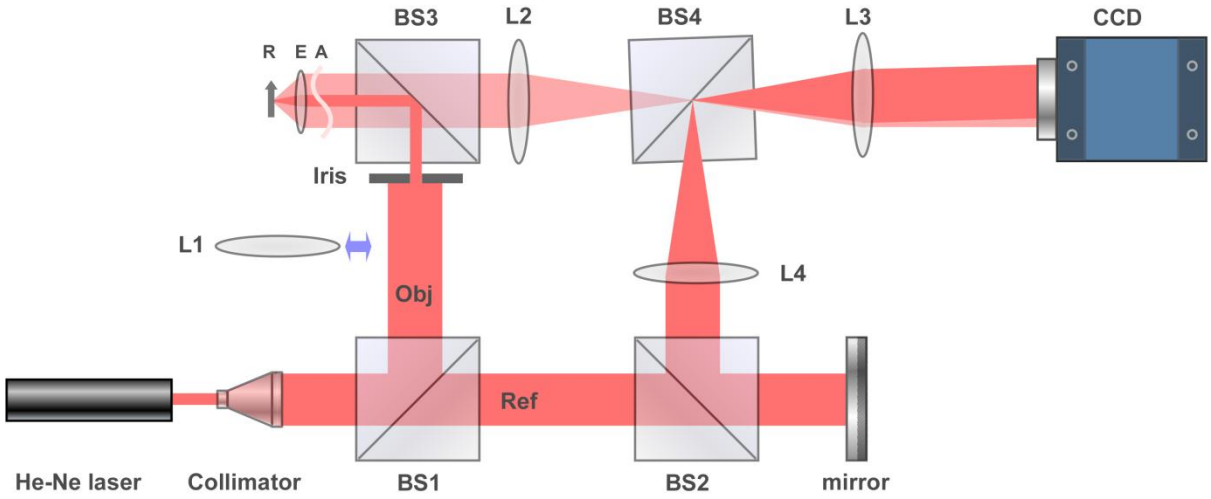

Figure 2.3. Optical system of IPDHAO. BS1-BS4: unpolarized beamsplitter. L1-L4: lens. E:eye lens. A: artificial aberrator. R: sample at retinal plane.

The optical system of IPDHAO is shown in Fig. 2.3. First, a narrow collimated He-Ne laser beam enters the eye lens E and is focused on the retinal surface R. For this proof-of-principle experiment, the eye is modeled by a combination of a simple lens (f_E= 25 mm), and a scattering sample R, placed at the focal plane of the lens. The aberration of the eye is realized by placing a broken piece of glass from a beaker in front of the lens. The complex optical field of the emergent light at the pupil plane is captured by the CCD camera with 1024×768 square pixels of a side length 4.65μm, which is focused at the pupil plane through the relay lenses L2(f_2=100mm) and L3(f_3=100mm). In the reference path for the holographic imaging, a lens L4 with same focal lens as L2 is put the same distance away from L3 as L2 to neutralize the phase curvature in the imaging path due to the lens L2. For the full-field imaging of the retinal surface, another lens L1 is inserted so that its focus coincides that of the eye lens E. A second exposure of

hologram is acquired at the pupil plane of the eye lens E. The two holograms are numerically combined and processed as described above to finally obtain the aberration-compensated image of the retina. Thus, the same holographic interferometer serves to achieve the sensing of the aberration field and compensation of the aberration. In comparison with conventional adaptive optics, a lenslet array, a second CCD camera, and a deformable mirror are absent, significantly reducing the complexity and cost of the apparatus.

2.4 Theory of Full-Field Imaging

In the optical system, we add a lens L4 with the same focal length as L2 and same distance away from L3 as L2. Why do we need this matching lens? As we described in the section 2.2, after we get the full-field complex amplitude at the CCD plane, a numerical lens needs be inserted and then we propagate the field after the numerical lens by a distance to the image plane. What optical parameters affect this propagation distance? To answer these questions, this section is devoted to the theoretical description of full-field imaging by use of paraxial approximation. The coordinate system adopted here is shown in Fig.2.4.

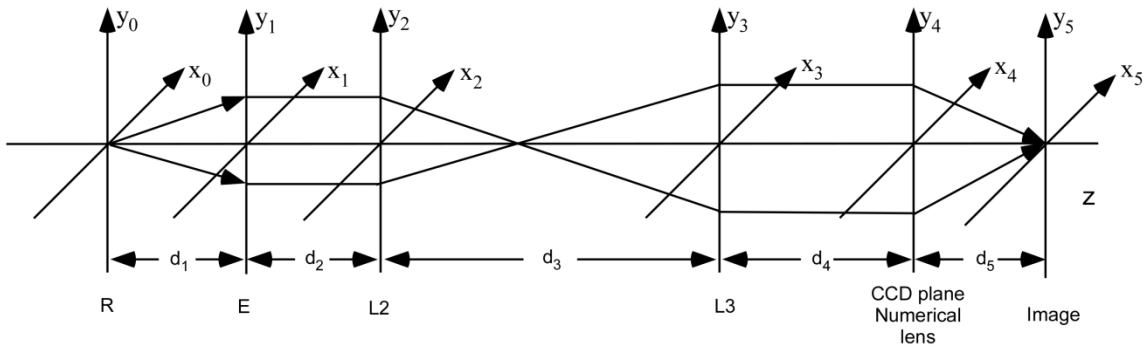

Figure 2.4. Coordinate system for imaging path of the optical apparatus.

The object at the retinal plane R is assumed to take the form as

$$O_0(x_0, y_0) = A(x_0, y_0)\exp[j\varphi(x_0, y_0)] \tag{2.1}$$

The distance d_1 between the retinal plane and the eye lens is set to be f_E, the focal length of the eye lens. The optical field after propagating a distance f_E can be given by [13].

$$O_{10}(x_1, y_1) = \exp[\frac{j\pi}{\lambda f_E}(x_1^2 + y_1^2)] \times \iint O_0(x_0, y_0) \exp[\frac{j\pi}{\lambda f_E}(x_0^2 + y_0^2)] \exp[-\frac{j2\pi}{\lambda f_E}(x_1 x_0 + y_1 y_0)] dx_0 dy_0 \tag{2.2}$$

The field going through the eye lens becomes

$$\begin{aligned} O_1(x_1, y_1) &= \exp[-\frac{j\pi}{\lambda f_E}(x_1^2 + y_1^2)] O_{10}(x_1, y_1) \\ &= \iint O_0(x_0, y_0) \exp[\frac{j\pi}{\lambda f_E}(x_0^2 + y_0^2)] \exp[-\frac{j2\pi}{\lambda f_E}(x_1 x_0 + y_1 y_0)] dx_0 dy_0 \end{aligned} \tag{2.3}$$

In IPDHAO, O_1 is imaged on the CCD plane, therefore it can be considered as the object of following optical systems up to the CCD plane. O_1 propagates in the free space by a distance d_2 which is set to be the focal length f_2 of L2 and goes through the lens L2. The resultant optical field after L2 can be expressed as

$$O_2(x_2, y_2) = \iint O_1(x_1, y_1) \exp[\frac{j\pi}{\lambda f_2}(x_1^2 + y_1^2)] \exp[-\frac{j2\pi}{\lambda f_2}(x_2 x_1 + y_2 y_1)] dx_1 dy_1 \tag{2.4}$$

The O_2 propagates in the free space by a distance d_3 and goes through the lens L3, obtaining a field after L3 as

$$O_3(x_3, y_3) = \exp[-\frac{j\pi}{\lambda f_3}(x_3^2 + y_3^2)] \exp[\frac{j\pi}{\lambda d_3}(x_3^2 + y_3^2)] \iint O_2(x_2, y_2) \exp[\frac{j\pi}{\lambda d_3}(x_2^2 + y_2^2)] \exp[-\frac{j2\pi}{\lambda d_3}(x_3 x_2 + y_3 y_2)] dx_2 dy_2 \tag{2.5}$$

Substituting Eq. (2.4) into Eq. (2.5),obtaining

$$
\begin{aligned}
O_3(x_3,y_3) &= \exp[-\frac{j\pi}{\lambda f_3}(x_3^{\,2}+y_3^{\,2})]\exp[\frac{j\pi}{\lambda d_3}(x_3^{\,2}+y_3^{\,2})] \\
&\iint\iint dx_1dy_1O_1(x_1,y_1)\exp[\frac{j\pi}{\lambda f_2}(x_1^{\,2}+y_1^{\,2})] \\
&\exp[-\frac{j2\pi}{\lambda f_2}(x_2x_1+y_2y_1)]\exp[\frac{j\pi}{\lambda d_3}(x_2^{\,2}+y_2^{\,2})]\exp[-\frac{j2\pi}{\lambda d_3}(x_3x_2+y_3y_2)]dx_2dy_2 \\
&= \exp[\frac{j\pi}{\lambda}(\frac{1}{d_3}-\frac{1}{f_3})(x_3^{\,2}+y_3^{\,2})] \\
&\iint\iint dx_1dy_1O_1(x_1,y_1)\exp[\frac{j\pi}{\lambda f_2}(x_1^{\,2}+y_1^{\,2})] \\
&\exp[\frac{j\pi}{\lambda d_3}(x_2^{\,2}+y_2^{\,2})]\exp\{-\frac{j2\pi}{\lambda}[(\frac{x_1}{f_2}+\frac{x_3}{d_3})x_2+(\frac{y_1}{f_2}+\frac{y_3}{d_3})y_2]\}dx_2dy_2
\end{aligned}
\tag{2.6}
$$

To simplify Eq. (2.6), we need use the following Fourier transformation relation

$$
FT\{\exp(\frac{j\pi}{\lambda d}x^2)\} = \sqrt{\frac{\lambda d}{-j}}\exp(-\pi j\lambda d f^2) \tag{2.7}
$$

where FT means Fourier transformation. Plugging Eq. (2.7) into Eq. (2.6), we can obtain

$$
\begin{aligned}
O_3(x_3,y_3) &= \exp[\frac{j\pi}{\lambda}(\frac{1}{d_3}-\frac{1}{f_3})(x_3^{\,2}+y_3^{\,2})] \\
&\iint dx_1dy_1O_1(x_1,y_1)\exp[\frac{j\pi}{\lambda f_2}(x_1^{\,2}+y_1^{\,2})] \\
&\exp\{-j\pi\lambda d_3\frac{1}{\lambda^2}[(\frac{x_1}{f_2}+\frac{x_3}{d_3})^2+(\frac{y_1}{f_2}+\frac{y_3}{d_3})^2]\} \\
&= \exp[-\frac{j\pi}{\lambda f_3}(x_3^{\,2}+y_3^{\,2})]\iint dx_1dy_1O_1(x_1,y_1)\exp[\frac{j\pi}{\lambda}(\frac{1}{f_2}-\frac{d_3}{f_2^{\,2}})(x_1^{\,2}+y_1^{\,2})] \\
&\exp[-j2\pi\frac{1}{\lambda f_2}(x_3x_1+y_3y_1)]
\end{aligned}
\tag{2.8}
$$

where a global constant is ignored. To image O_1 onto the CCD plane, d_3 is set to be f_3, the focal length of L3. The optical field at CCD plane can be given by

$$
\begin{aligned}
O_4(x_4,y_4) &= \exp[\frac{j\pi}{\lambda f_3}(x_4{}^2+y_4{}^2)] \\
&\iint O_3(x_3,y_3)\exp[\frac{j\pi}{\lambda f_3}(x_3{}^2+y_3{}^2)]\exp[-\frac{j2\pi}{\lambda f_3}(x_4x_3+y_4y_3)]dx_3dy_3 \\
&= \exp[\frac{j\pi}{\lambda f_3}(x_4{}^2+y_4{}^2)]\iint\iint dx_1dy_1O_1(x_1,y_1)\exp[\frac{j\pi}{\lambda}(\frac{1}{f_2}-\frac{d_3}{f_2{}^2})(x_1{}^2+y_1{}^2)] \\
&\exp\{-\frac{j2\pi}{\lambda}[(\frac{x_1}{f_2}+\frac{x_4}{f_3})x_3+(\frac{y_1}{f_2}+\frac{y_4}{f_3})y_3]\}dx_3dy_3 \\
&= \exp[\frac{j\pi}{\lambda f_3}(x_4{}^2+y_4{}^2)]\iint dx_1dy_1O_1(x_1,y_1)\exp[\frac{j\pi}{\lambda}(\frac{1}{f_2}-\frac{d_3}{f_2{}^2})(x_1{}^2+y_1{}^2)] \\
&\delta[\frac{1}{\lambda}(\frac{x_1}{f_2}+\frac{x_4}{f_3}),\frac{1}{\lambda}(\frac{y_1}{f_2}+\frac{y_4}{f_3})] \\
&= O_1(-\frac{f_2x_4}{f_3},-\frac{f_2y_4}{f_3})\exp[\frac{j\pi}{\lambda f_3}(x_4{}^2+y_4{}^2)]\exp[\frac{j\pi}{\lambda}(\frac{1}{f_2}-\frac{d_3}{f_2{}^2})(\frac{f_2}{f_3})^2(x_4{}^2+y_4{}^2)]
\end{aligned}
\tag{2.9}
$$

Equation (2.9) shows that there is a quadratic phase curvature modulating the geometrical image $O_1(-\frac{f_2x_4}{f_3},-\frac{f_2y_4}{f_3})$. If O_1 is the artificial aberration, then the measured aberration will be overshadowed by this quadratic phase term. Since we know the mathematical form of this phase term, we can remove it numerically to obtain the phase aberration. In IPDHAO, we adopt an experimental method to remove this quadratic phase term by introducing a reference beam that experiences same phase curvature as the full-field object field. This idea is realized by putting the L4 with same focal length as L2 and same distance away from L3 as L2. If the reference field at the pupil plane is a planar wave,

$$
R_1(x_1,y_1)=1 \tag{2.10}
$$

Replacing O_1 by R_1 in Eq. (2.9), the reference field at the CCD plane has the form as

$$
\begin{aligned}
R_4(x_4,y_4) = \exp[\frac{j\pi}{\lambda f_3}(x_4{}^2+y_4{}^2)]\exp[\frac{j\pi}{\lambda}(\frac{1}{f_2}-\frac{d_3}{f_2{}^2})(\frac{f_2}{f_3})^2(x_4{}^2+y_4{}^2)] \\
\exp[\frac{j2\pi}{\lambda}(x_4\cos\alpha+y_4\cos\beta)]
\end{aligned}
\tag{2.11}
$$

where α and β represent the angles of the wave vector of the reference field with respect to the x and y axis respectively. The digital hologram can be given by

$$I_4(x_4, y_4) = |R_4|^2 + |O_4|^2 + O_4^* R_4 + R_4^* O_4 \tag{2.12}$$

Filtering out the image order and moving it in the center of the Fourier domain, the resultant field from the digital hologram becomes

$$\begin{aligned} O_{41}(x_4, y_4) &= O_1(-\frac{f_2 x_4}{f_3}, -\frac{f_2 y_4}{f_3}) \\ &= \iint O_0(x_0, y_0) \exp[\frac{j\pi}{\lambda f_E}(x_0^2 + y_0^2)] \exp[\frac{j2\pi f_2}{\lambda f_E f_3}(x_4 x_0 + y_4 y_0)] dx_0 dy_0 \end{aligned} \tag{2.13}$$

To find the image, we first insert a numerical lens with a focal length f_N at the CCD plane, the field after this numerical lens becomes

$$O_{42}(x_4, y_4) = \exp[-\frac{j\pi}{\lambda f_N}(x_4^2 + y_4^2)] O_1(-\frac{f_2 x_4}{f_3}, -\frac{f_2 y_4}{f_3}) \tag{2.14}$$

Then, we propagate O_{42} by a distance d_5, obtaining

$$\begin{aligned} O_5(x_5, y_5) &= \exp[\frac{j\pi}{\lambda d}(x_5^2 + y_5^2)] \\ &\times \iint O_{42}(x_4, y_4) \exp[\frac{j\pi}{\lambda d_5}(x_4^2 + y_4^2)] \exp[-\frac{j2\pi}{\lambda d_5}(x_5 x_4 + y_5 y_4)] dx_4 dy_4 \\ &= \exp[\frac{j\pi}{\lambda d_5}(x_5^2 + y_5^2)] \iint \iint dx_0 dy_0 O_0(x_0, y_0) \exp[\frac{j\pi}{\lambda f_E}(x_0^2 + y_0^2)] \\ &\times \exp[\frac{j\pi}{\lambda}(\frac{1}{d_5} - \frac{1}{f_N})(x_4^2 + y_4^2)] \exp\{\frac{j2\pi}{\lambda}[(\frac{f_2 x_0}{f_E f_3} - \frac{x_5}{d_5})x_4 + (\frac{f_2 y_0}{f_E f_3} - \frac{y_5}{d_5})y_4)]\} dx_4 dy_4 \end{aligned} \tag{2.15}$$

From Eq. (2.15), the imaging condition is given by

$$d_5 = f_N \tag{2.16}$$

With this relation, we can get the final image field as

$$O_5(x_5, y_5) = \exp[\frac{j\pi}{\lambda f_N}(x_5^2 + y_5^2)]$$
$$\times \iint dx_0 dy_0 O_0(x_0, y_0) \exp[\frac{j\pi}{\lambda f_E}(x_0^2 + y_0^2)] \delta[\frac{1}{\lambda}(\frac{f_2 x_0}{f_E f_3} - \frac{x_5}{f_N}), \frac{1}{\lambda}(\frac{f_2 x_0}{f_E f_3} - \frac{x_5}{f_N})] \quad (2.17)$$
$$= O_0(\frac{f_E f_3 x_5}{f_2 f_N}, \frac{f_E f_3 y_5}{f_2 f_N}) \exp[\frac{j\pi}{\lambda f_N}(x_5^2 + y_5^2)] \exp[\frac{j\pi f_E}{\lambda}(\frac{f_3}{f_2 f_N})^2 (x_5^2 + y_5^2)]$$

The magnification M is then given by

$$M = \frac{f_N f_2}{f_E f_3} \quad (2.18)$$

In this section, we have modeled wave propagation through the imaging path and found that without a matching lens, the aberration measurement will be modulated by quadratic phase curvature. That is why a matching lens L4 is added to demodulate this quadratic phase term. To get the final image, a numerical lens is needed. Image will be found at a distance f_N from the numerical lens.

2.5 Experimental Results and Discussions

In this section, we first report the experimental results on a paper target and study the effects of angular spectrum filter size and guide star input beam size on the quality of the corrected images. Then we present our experimental results on biological samples such as onion skin tissue and butterfly wing.

2.5.1 Paper Target

A set of image data on the paper target is shown in Fig. 2.5. Field of view on the retinal plane is $1792 \times 1344 \mu m^2$ with 1024×768 pixels. The hologram with full-field illumination is shown in Fig. 2.5(a). The angular spectrum, i.e. the Fourier transform, of the hologram is shown in Fig.

2.5(b), with the highlighted elliptical area on the lower right representing the first-order term for extracting the complex optical field [14]. The complex optical field of the full-field hologram is obtained by inverse Fourier transform of the filtered angular spectrum of Fig. 2.5(b), and is shown in Fig. 2.5(c) the amplitude, and Fig. 5(d) the phase. The sensing, or the guide star, hologram is shown in Fig. 2.5(e), and the angular spectrum in Fig. 2.5(f). In Fig. 2.5(f), we use a small radius 4.8 mm^{-1} for the numerical filter, which is 1/40 of the radius used in Fig. 2.5(b), as explained below, and therefore the highlighted area is difficult to discern. The complex optical field of the guide star hologram is shown in Fig. 2.5(g) the amplitude, and Fig. 2.5(h) the phase.

The two holograms thus obtained are then used to reconstruct the retinal image. First, in Fig. 2.6(a), the image reconstructed from another hologram without the phase aberrator – the broken piece of glass – in place is shown, as a base line. For reconstruction, we use a numerical lens of focal length 80 mm and the best image is obtained at a distance of 78 mm. Then, Fig. 2.6(b) is the image reconstructed from the complex hologram of Figs. 2.5(c) and (d), without the aberration compensation, showing significant degradation of the resolution. Finally the complex conjugate of the guide star hologram of Figs. 2.5(g) and (h) is multiplied to the uncorrected hologram of Figs. 2.5(c) and 2.5(d), the resultant corrected image is shown in Fig. 2.6(c). In both Figs. 2.6(b) and (c), the best focus images are obtained at a distance of 76 mm, the difference with the case of Fig. 2.6(a) being due to the presence of the piece of glass with approximately 1.2mm in thickness. Compensation of the effect of the aberration and improvement of the resolution is quite evident, thus demonstrating the validity of the IPDHAO principle.

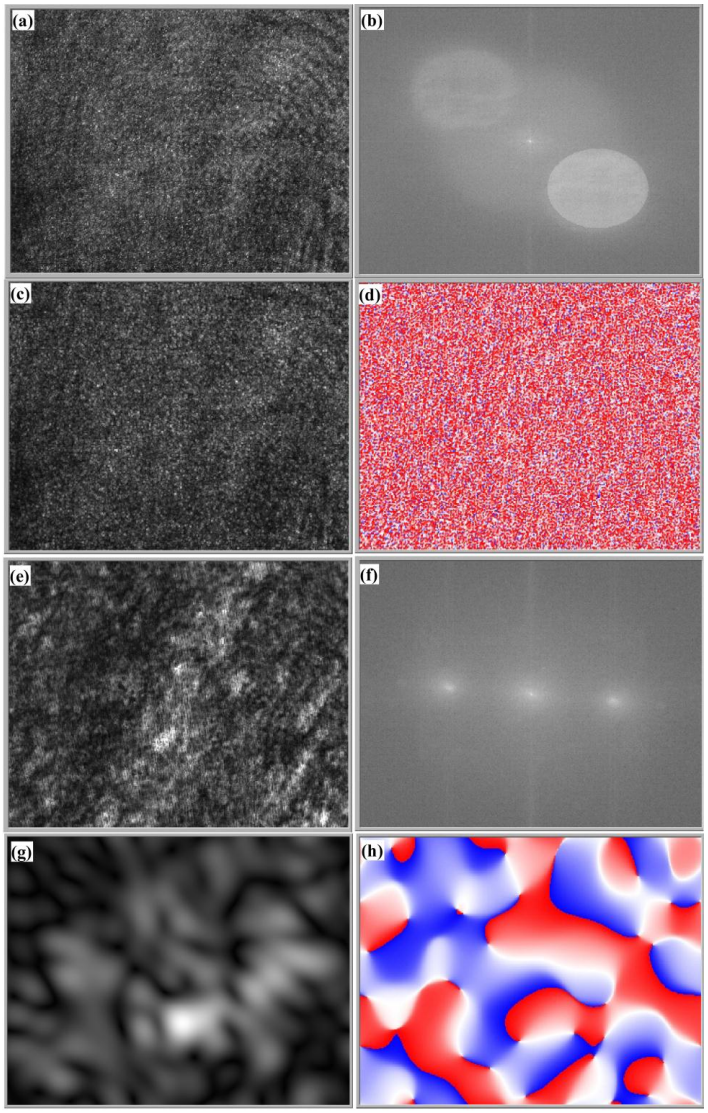

Figure 2.5. IPDHAO on paper target. (a) Distorted full-field hologram. (b) Angular spectrum of (a). (c) Full-field amplitude. (d) Full-field phase. (e) Guide star hologram. (f) Angular spectrum of (e). (g) Reconstructed amplitude from (e). (h) Measured aberration from (e).

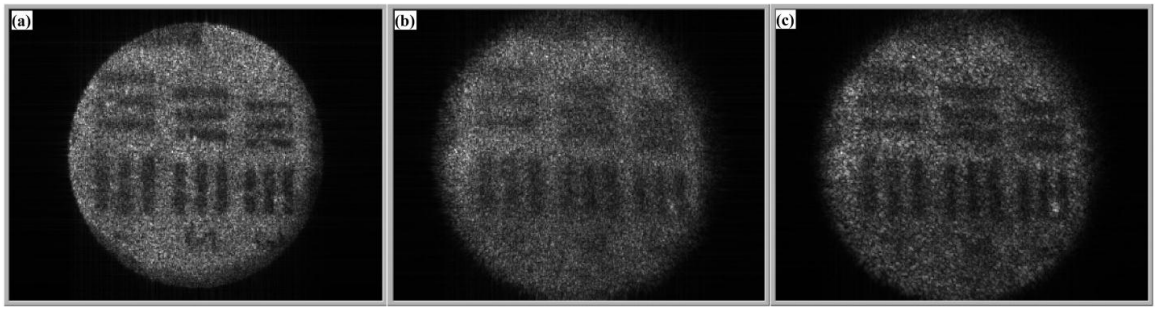

Figure 2.6. Image correction by IPDHAO. (a) Image without aberrator in place. (b) Image distorted by the aberrator. (c) Corrected image.

2.5.2 Image Quality versus Filter Size

The quality of the corrected image is significantly affected by the size of the numerical filter that determines the accuracy of the phase aberration measurement. The filter size should be large enough to recover most information of the phase aberration and small enough to avoid the strong speckle noise due to the scattering nature of the sample. Fig. 2.7(a)-(c) are angular spectra of the hologram, Fig. 2.5(a), with filter diameters 1.6 mm^{-1}, 4.8 mm^{-1}, and 48 mm^{-1} respectively, as shown in the highlighted areas. The filters in Figs. 2.7(a) and (b) are too small to see. Figures 2.7(d)-(f) are phase profiles of the filtered angular spectra of Figs. 2.7(a)-(c). They are measured phase aberrations under varying filters. Figures 2.7(g)-(i) show the corrected images by the measured phase aberrations shown in Figs. 2.7(d)-(f). Compared to the aberration affected image Fig. 2.6(b), the corrected image, Fig. 2.7(g), shows moderate improvement. The horizontal bars are barely resolved, but the vertical bars are still oblique. That is because the very low frequency components of the phase aberration are recovered, as shown in Fig. 2.7(d), while a number of higher frequency constituents are lost. When the filter diameter increases to 4.8 mm^{-1}, most information of the aberration can be obtained, resulting phase profile, Fig. 2.7(e), shows more irregularity and the corrected image, Fig. 2.7(h) shows significant improvement. The horizontal bars are readily resolved and the obliquity of the vertical bars is corrected. In fact, when filter size ranges from 4.5 mm^{-1} to 5.5 mm^{-1}, the corrected images are comparable in quality. When a much larger filter is used, more frequency constituents can be obtained, but severe noise mainly from the speckle will also be included. As a result, the phase profile, Fig. 2.7(f) shows severe noise, and the corrected image, Fig. 2.7(i), is greatly degraded compared to the best case, Fig. 2.7(h).

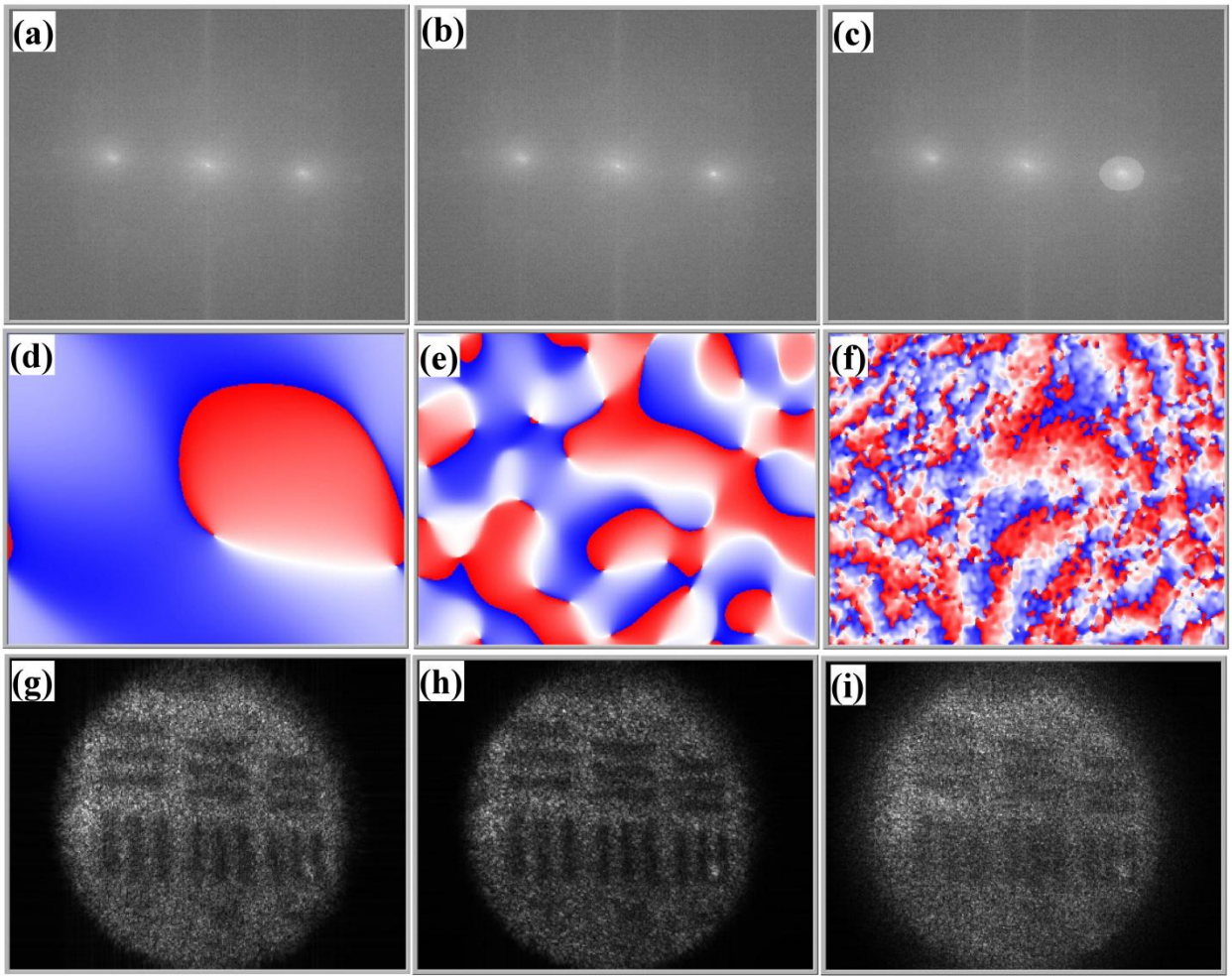

Figure 2.7. Quality of the corrected images versus the numerical filter size. (a)-(c) are angular spectra of the hologram shown in Fig. 5(e), with filter diameters 1.6mm^{-1}, 4.8mm^{-1}, and 48mm^{-1} respectively. (d)-(f) Phase profiles of filtered angular spectra of (a)-(c). They are measured phase aberrations. (g)-(i) Images corrected by (a)-(c) respectively.

2.5.3 Image Quality versus Input Beam Size

The input beam size in the guide star sensing process is another contributing parameter to the quality of corrected image. It determines the quality of the guide star spot that in principle should be close to an ideal point source and emits a spherical wave. If there is no aberration, the guide star spot size is inversely proportional to the input beam size, according to the diffraction theory [13]. This relationship does not hold if the aberration exists. It is worth exploring this relationship when a typical aberration exists to estimate optimal size of the input beam. We first

run simulations using a typical aberration. Then experimental results are presented to validate the observations in the simulations.

The optical aberration can be represented by a series of Zernike polynomials [1,4,5]. The aberration can be given by

$$\varphi(x, y) = \sum_{j=0}^{20} C_j Z_j(x, y) \tag{2.19}$$

where (x, y) is the coordinate of the pupil plane, Z_j represents the jth Zernike term and C_j the corresponding coefficient. We generate a typical aberration by a series of Zernike terms up to the fifth order. Because the constant term Z_0 and linear terms Z_1 & Z_2 have no influence on the spectral width of the aberration, they are ignored in the simulation. The coefficients of the defocus and astigmatism terms C_3- C_5 are set to be π that are the same level compared to the normal eye [15]. If the real eye has much higher defocus and astigmatism, they can be greatly reduced by adjusting the optics and trial lens in the experiment [5]. The coefficients of other terms, or higher order aberrations, are set to one, which is higher than the normal eye [15]. The phase profile is composed of 1024×1024 pixels with pixel size 4.65μm×4.65μm^2. The complex amplitude transmission of this pupil can be written as $A\exp(j\varphi)$, where A is the amplitude and set to be one in the simulation. For an aberration free pupil, the guide star spot decreases as the input beam increases [13]. Due to the aberration, the guide star spot shrinks as the input beam increases only when using narrow input beam. When a wide beam is used, the aberration will spread the focus energy distribution and increases the guide star spot size. We assume the pupil is illuminated by a Gaussian beam of an optical field represented by $\exp(-\frac{4(x^2+y^2)}{d_g^{\,2}})$, where d_g is the diameter of the beam. This collimated beam goes through the aberration and the eye lens, and is finally brought to focus at the retinal plane. The formed guide star spot will change as the

diameter d_g changes. Assume the complex amplitude of the guide star spot is represented by $g(x_0,y_0)$, where (x_0,y_0) is the coordinate at the retinal plane. The distributions of the modulus of $g(x_0,y_0)$ are shown in Figs. 2.8(a)-(c), which correspond to the input beam diameters 0.4 mm, 1.8mm, and 3.6 mm respectively. It is quite evident that the guide star spot shrinks when using a small beam, while spreads using a large beam, as expected. To quantitatively assess the guide star spot, we introduce the guide star spot diameter d_s such that most of the energy is concentrated in the circle with diameter d_s. There is no well-defined quantity on how much out of the total energy should be chosen to determine this diameter d_s. Fortunately, the goal of this simulation is to see if there is a range of input beam size where the guide star spot stay unchanged or their exact distribution will not change the quality of the corrected images. We could find such a plateau when we vary this ratio from 0.95 to 0.99. Fig. 2.8 (d) shows the relationship between the guide star spot diameter d_s and the input beam diameter d_g , where we set this ratio as 0.99. d_s decreases until d_g reaches 1.1 mm and experiences a flat region when d_g ranges from 1.1 mm to 2.3 mm, and then increases again. The mid-point is 1.7 mm. The mid-point of the flat region will increase as we reduce the higher order aberrations. From the simulations, we find that there is always a plateau in the curve while varying the aberration strength, although the midpoint and width of this flat region will changes as the strength.

To verify this observation, experiments with varying input beam size are carried out. The phase profiles with varying input beam size are shown in Fig. 2.9. The input beam diameters corresponding to (a)-(h) are from 0.5 mm to 4.0 mm at a 0.5 mm step. The images compensated for by the phase aberrations Figs. 2.9(a)-(h) are shown in Figs. 2.10(a)-(h). The images, Figs. 2.10(a)-(c), experience an obvious increase in quality, which corresponds to a decrease in guide star spot diameter when the input beam diameter increases from 0.5mm to 1.5mm. Figures

2.10(c) and2.10 (d) are comparable and the best in quality, which indicates an unchanged guide star diameter when input beam ranges from 1.5 mm to 2.0 mm in diameter. The images, shown in Figs. 2.10(d)-(h), show a decrease in image quality, which signifies an evident increase in guide star spot diameter when the input beam diameter increases from 2.0 mm to 4.0 mm. Using a narrow input beam, the diffraction effect dominates and broadens the guide star spot, while using a wide input beam, the aberration takes over and broadens the guide star spot. Only at a moderate input beam size, do these two effects balance each other, resulting in an optimal guide star spot and in turn an optimal image.

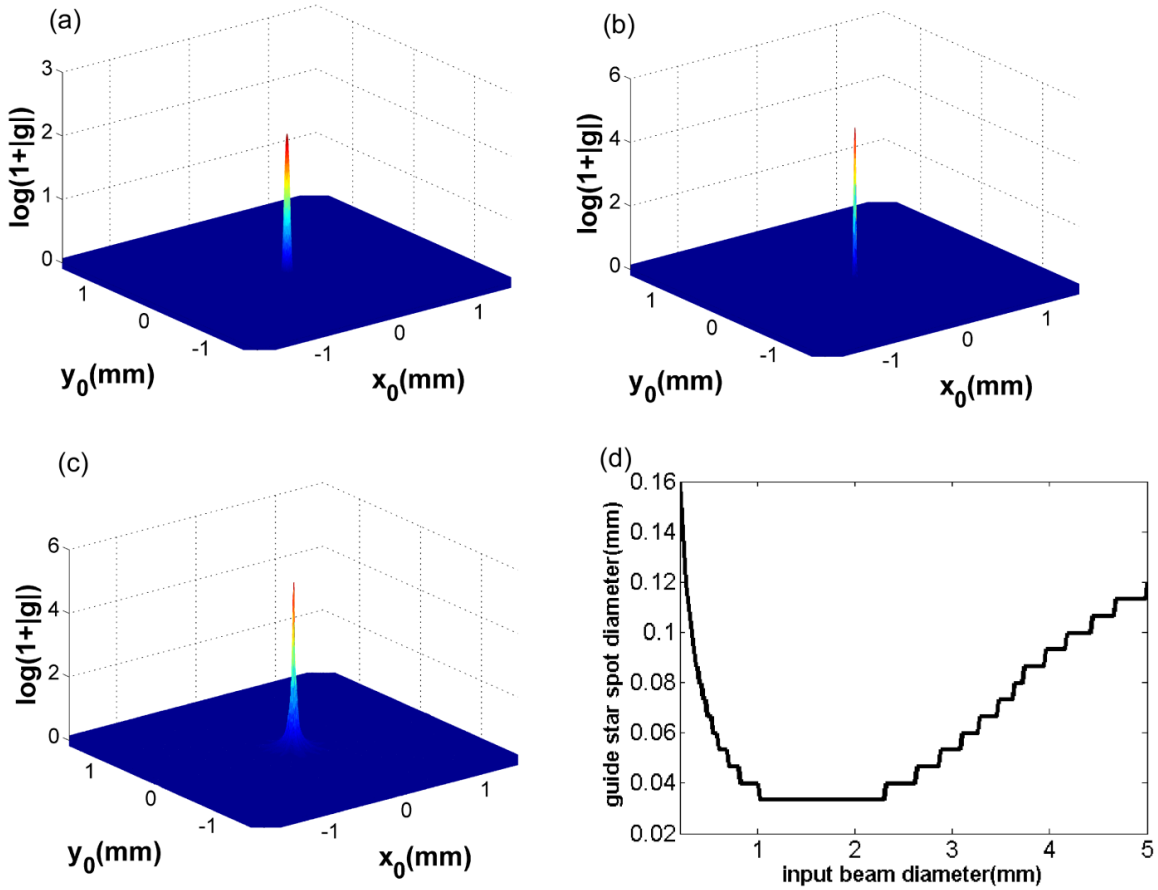

Figure 2.8. The effect of the input beam size on the guide star spot. (a)-(c) are modulus of the complex amplitude, $g(x_0,y_0)$, of the guide star spot when input beam diameters are 0.4 mm, 1.8 mm, 3.6 mm respectively. They are displayed in logarithmic scale. (d) shows the dependency of the guide star spot diameter on the input beam diameter.

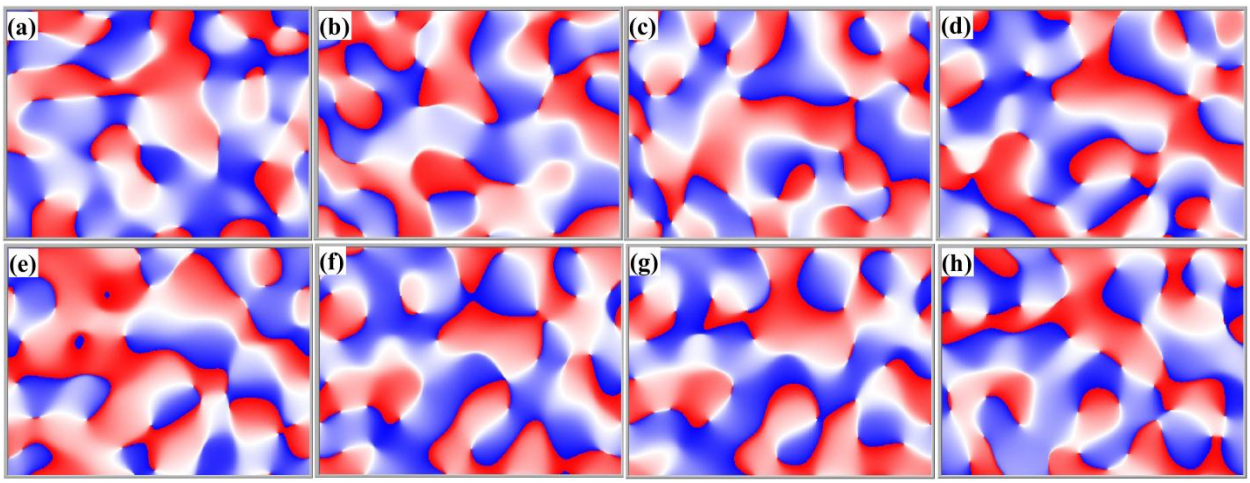

Figure 2.9. Phase aberrations at varying input beam size. The input beam diameters of (a)-(h) increase from 0.5 mm to 4.0mm at a step 0.5mm.

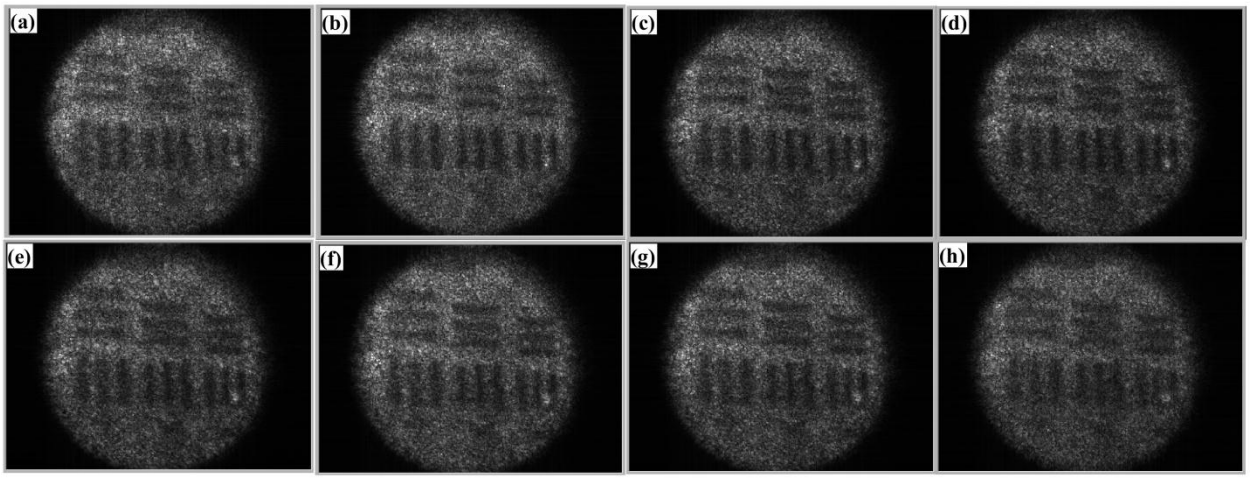

Figure 2.10. Quality of the corrected image versus input beam size. (a)-(h) are corrected images by (a)-(h) of Fig.2.9.

2.5.4 Biological Samples

In this section, two biological samples are used to further verify the feasibility of IPDHAO. The first biological sample is onion skin tissue. Experimental results on this sample are shown in Fig. 2.11. Figure 2.11(a) shows the image without aberrator added in the pupil plane. The phase aberration sensed by DH is shown in Fig. 2.11(b). Figure 2.11(c) shows the image distorted by the aberrator and the corrected image is shown in Fig. 2.11(d) which is

comparable to the undistorted image in Fig. 2.11(a) in terms of quality.

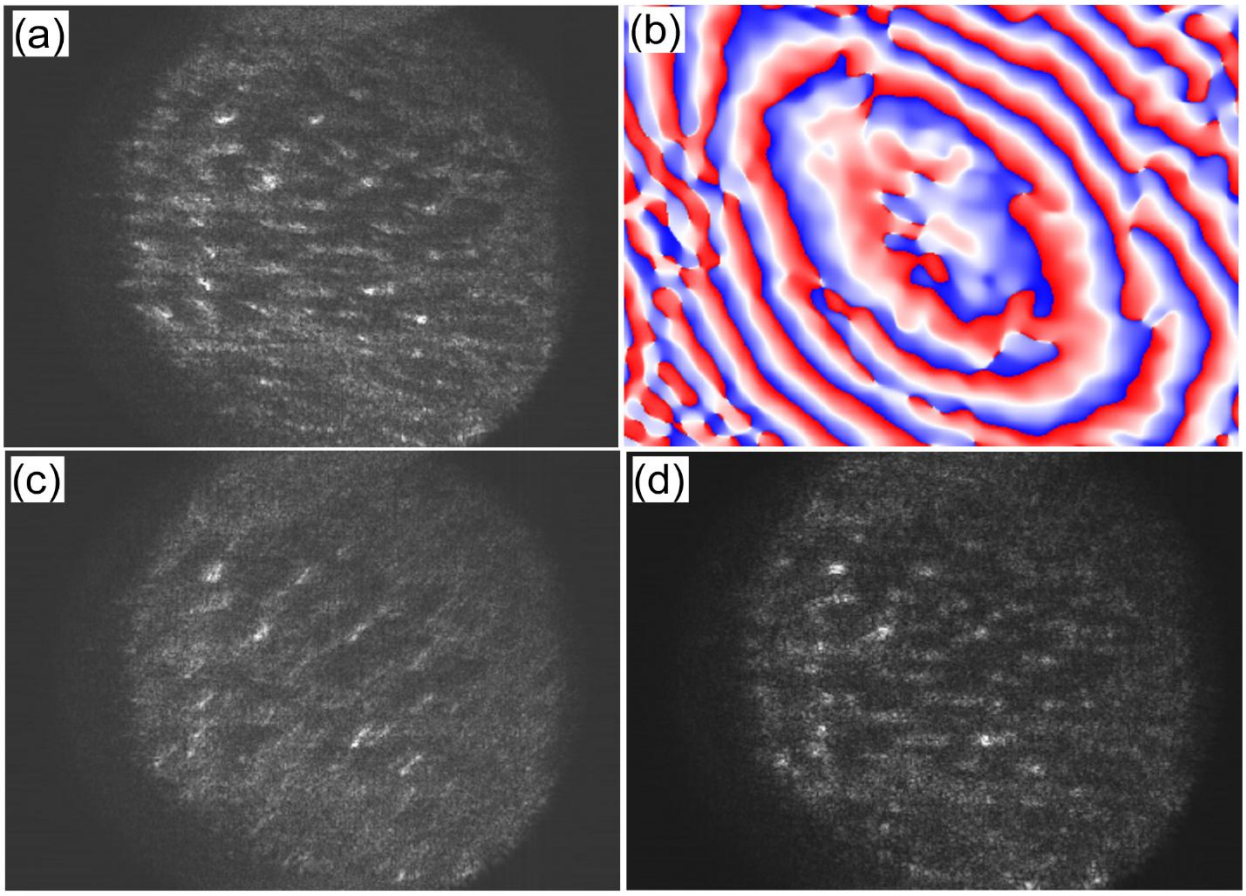

Figure 2.11. IPDHAO on the onion skin tissue. FOV is $1792\times1344\mu m^2$

A second example is butterfly wing which is a strongly scattering sample as the paper target. In this case, the focal lengths of both L2 and L3 are changed to 200mm to increase to the magnification. The calibrated field of view (FOV) on retinal plane is 990μm×720μm. A set of images from this sample are shown in Fig. 2.12. Figure 2.12(a) represents the base line image. Figure 2.12(b) shows the measured aberration. The distorted image is shown in Fig.2.12(c) and the corrected image is shown in Fig. 2.12(d) which is also comparable to the undistorted image in Fig. 2.12(a) in terms of quality.

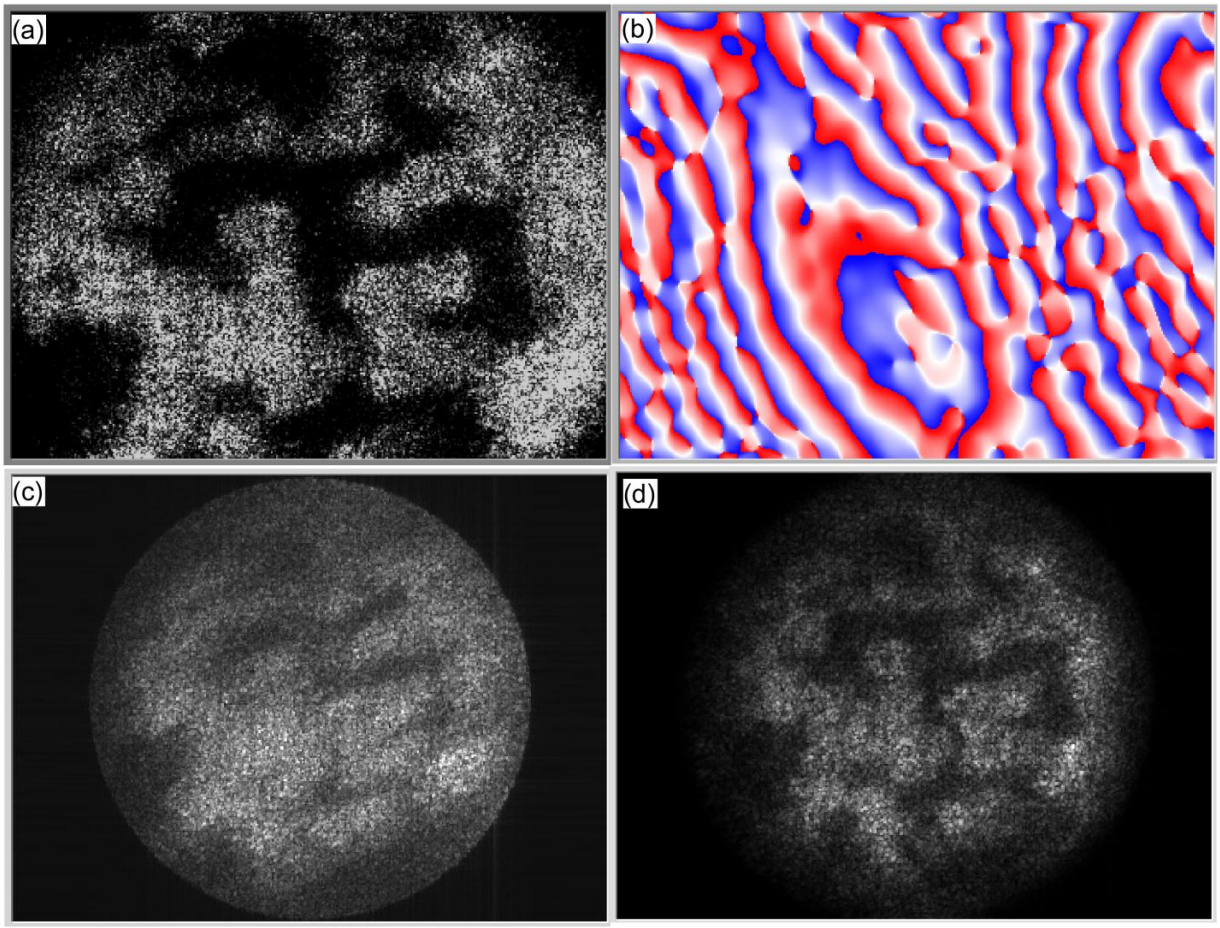

Figure 2.12. IPDHAO on butterfly wing. (a) The image without aberration, FOV: 990μm×720μm. (b) Phase aberration. (c) Distorted image. (d) The corrected image.

2.6 Conclusions

We present a new type of adaptive optics, IPDHAO, based on the principles of digital holography. IPDHAO realize the aberration sensing by a guide star hologram and image correction by use of numerical processing, thus removing the need of hardware-based wavefront sensor, wavefront corrector and complicated control procedures. The basic idea of IPDHAO are described and verified by computer simulations. Then proof of concept experiments are carried out by use of an eye model. The basic process is first demonstrated by use of a paper target. The effects of the angular spectrum filter size and guide star input beam size are studied through

simulations and experiments. Due to the scattering nature of the sample, the filter of angular spectrum should be set to be small enough to reduce the speckle noise and large enough to encircle most information of the aberration. In the aberration sensing, input beam has to be set to be in a range where the assumption that the guide star acts like a point source holds well. For the aberrator we use in the experiments, the optimal beam size is in the range between 1.5mm to 2.0mm in diameter. The feasibility of IPDHAO is further validated by use of biological samples such as onion skin tissues and butterfly wing. The former represents a weakly scattering sample, and the latter a strongly scattering sample.

The idea of IPDHAO is trying to replace the hardware pieces and control procedures of the conventional AO for retinal imaging. So in IPDHAO, we put the CCD plane at the conjugate of the eye pupil as the conventional AO does. In fact, DHAO is a coherent imaging modality which has the access to the complex amplitude of the optical field. This capability enables us to design more flexible optical configuration to realize goals set by IPDHAO. In the next chapter, we will describe an alternative DHAO system where the CCD is not put at the image plane of the eye pupil. This alternative DHAO system will be detailed in the following chapter.

2.7 References

1. J. Porter, H. Queener, J. Lin, K. Thorn, and A. Awwal, eds., *Adaptive optics for vision science*, John Wiley & Sons, Hoboken, New Jersey, (2006).

2. R. D. Ferguson, D. Hammer, A. Elsner, R. H. Webb, S. A. Burns, and J. J. Weiter, "Wide-field retinal hemodynamic imaging with the tracking scanning laser ophthalmoscope," Opt. Express **12**, 5198-5208(2004).

3. M. Wojtkowski, T. Bajraszewski, P. Targowski, and A. Kowalczyk, "Real-time in vivo imaging by high-speed spectral optical coherence tomography," Opt. Lett. **28**, 1745-1747(2003).

4. K. M. Hampson, "Adaptive optics and vision," J. Mod. Opt. **55**, 3425-3467(2008).

5. J. Z. Liang, B. Grimm, S. Goelz, and J. F. Bille, "Objective measurement of wave aberrations of the human eye with the use of a hartmann-shack wave-front sensor," J. Opt. Soc. Am. A **11**, 1949-1957(1994).

6. N. Doble, G. Yoon, L. Chen, P. Bierden, B. Singer, S. Olivier, and D. R. Williams, "Use of a microelectromechanical mirror for adaptive optics in the human eye," Opt. Lett. **27**, 1537-1539(2002).

7. Q. A. Yang, D. W. Arathorn, P. Tiruveedhula, C. R. Vogel, and A. Roorda, "Design of an integrated hardware interface for AOSLO image capture and cone-targeted stimulus delivery," Opt. Express **18**, 17841-17858(2010).

8. A. Roorda, F. Romero-Borja, W. J. Donnelly III, H. Queener, T. J. Herbert, and M. C. W. Campbell, "Adaptive optics scanning laser ophthalmoscopy," Opt. Express **10**, 405-412 (2002).

9. J. Rha, A. M. Dubis, M. Wagner-Schuman, D. M. Tait, P. Godara, B. Schroeder, K. Stepien, and J. Carroll, "Spectral domain optical coherence tomography and adaptive optics: imaging photoreceptor layer morphology to interpret preclinical phenotypes," Retinal Degenerative Diseases: Laboratory and Therapeutic Investigations **664**, 309-316(2010).

10. R. J. Zawadzki, S. S. Choi, A. R. Fuller, J. W. Evans, B. Hamann, and J. S. Werner, "Cellular resolution volumetric in vivo retinal imaging with adaptive optics-optical coherence tomography," Opt. Express **17**, 4084-4094 (2009).

11. R. J. Zawadzki, S. S. Choi, S. M. Jones, S. S. Oliver, and J. S. Werner, "Adaptive optics-optical coherence tomography: optimizing visualization of microscopic retinal structures in three dimensions," J. Opt. Soc. Am. A **24**, 1373-1383 (2007).

12. T. Kohnen, J. Buhren, C. Kuhne, and A. Mirshahi, "Wavefronto-guided LASIK with the Zyoptix 3.1 system for the correction of myopia and compound myopic astigmatism with 1-year follow-up Clinical outcome and change in higher order aberrations," Ophthalmology **111**, 2175-2185 (2004).

13. J. W. Goodman, *Introduction to Fourier Optics*, 3rd ed. Roberts & Company Publishers, Englewood, Colorado, (2005).

14. M.K. Kim, "Principles and techniques of digital holographic microscopy," SPIE Reviews **1**, 1-50(2010).

15. J. Porter, A. Guirao, Ian G. Cox, and David R. Williams, "Monochromatic aberrations of the human eye in a large population," J. Opt. Soc. Am. A **18**, 1793-1803(2001).

Chapter Three:

Fourier Transformation Digital Holographic Adaptive Optics

3.1 Introduction

In the original digital holographic adaptive optics (DHAO) setup [1], the imaging sensor is put at the conjugate plane of the eye pupil. From a guide star hologram, we can obtain the phase aberration at pupil plane. The imaging lens other than the eye lens will introduce spherical curvature that has to be removed by additional matching lens in the reference beam. And, the correct guide star hologram is difficult to obtain. Many trials have to be performed to get a correct measurement of the phase aberration. To get a focus image, a numerical lens is added and numerical propagation is performed. If the effective CCD aperture is smaller than the pupil, the resolution will be limited. Also, it becomes hard to employ a low coherence or incoherent light source [2-6], which may be methods of reducing the speckle noise if it becomes a real issue in the real retinal imaging. To address these limitations, Fourier Transform DHAO (FTDHAO) system is presented. The CCD is put at the exact FT plane of the eye pupil. There is no spherical curvature induced by the imaging lens, resulting in a more precise measurement of the phase aberration and more compact system. The CCD can directly record the amplitude point spread function (PSF) of the system, making it easier to determine the correct guide star hologram. The CCD is also at the image plane of the target. The signal will be stronger than the original DHAO system, especially for the phase aberration sensing. Numerical propagation is not necessary. If the pixel is smaller than half of the diffraction limited resolution, other parameters of the CCD

have nothing to do with the resolution. So, the CCD's aperture will not affect the resolution anymore. With some modifications, low coherence or even incoherent light source can be incorporated [2-6]. So, the system will be more flexible and applicable.

The principle of the proposed FTDHAO imaging system is different from that of the existing DHAO imaging system [1]. In the FTDHAO imaging system, the phase aberration at the eye pupil can be retrieved by the inverse FT of the guide star hologram and the complex amplitude of full field optical field at the eye pupil can be obtained by the inverse FT of the full field hologram. The correction takes place at the eye pupil, instead of the CCD plane. Taking FT of the corrected field at the eye pupil, the corrected image can be obtained. Numerical propagation is not necessary. Simulations and experimental studies show the efficiency and robustness of this new DHAO system.

This chapter is organized as follows: the FTDHAO apparatus is presented and the principle of this new system is described in section 3.2. In section 3.3, simulations are given. The experimental results are given and discussed in section 3.4. Finally, the conclusions are drawn.

3.2 Optical Apparatus

The schematic of FTDHAO setup is illustrated in Fig.3.1. He-Ne laser is the light source with a wavelength 632.8nm. The eye lens is simulated by the lens E of which the focal length f_1 25mm. R represents retinal plane that is at the back focal plane of eye lens E. A represents the phase aberrator that is at the pupil of the eye lens. The distance between lens E and L2 and that between L2 and the CCD are equal to the focal length f_2 of L2 that is 200mm. According to the ref.[7], the optical field at the CCD plane is the Fourier transformation of the optical field at the eye pupil except a global prefactor. That is why this DHAO system is termed as FTDHAO.

Similar to the original DHAO, a narrow beam is sent into the eye lens to generate a guide star on the sample and wave sensing is performed by processing the guide star hologram. Then, L1 is inserted and distorted full-field image is obtained by a second hologram. Lastly, image is improved by removing the aberration sensed in the first step from the second hologram. The theory of this process will be presented in section 3.3.

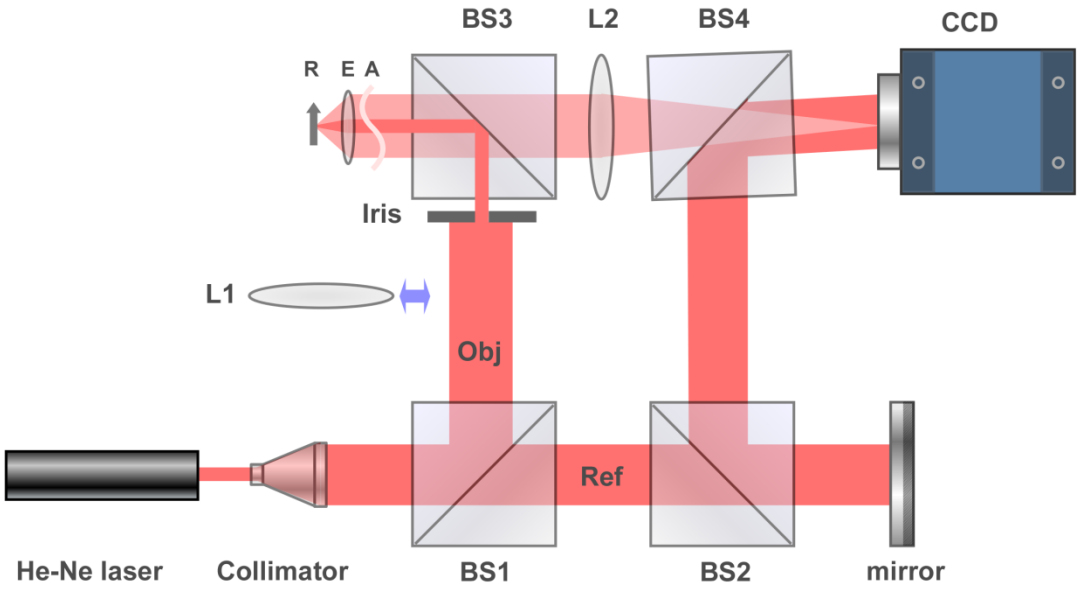

Figure 3.1. Schematic of the Fourier Transform digital holographic adaptive optics imaging system. R: Retina. E: Eye lens of focal length 25mm. A: aberrator. L1:75mm in focal length. L2:200mm. BS1-4: Beamsplitters.

3.3 Theory

The mathematical description of FTDHAO is presented in this section. The coordinate systems adopted for the derivation are illustrated by Fig. 3.2. The relationship between the optical field $P(x_1,y_1)$ at the eye pupil and the field $O(x_2,y_2)$ at the CCD is given by [7]

$$O(x_2, y_2) = \frac{1}{j\lambda f_2} \iint P(x_1, y_1) \exp[-j2\pi \frac{1}{\lambda f_2}(x_2 x_1 + y_2 y_1)] dx_1 dy_1 \qquad (3.1)$$

where λ is the wavelength of the light source. Ignoring the prefactor, Eq. (3.1) can be rewritten as

$$O(f_x, f_y) = FT\{P(x_1, y_1)\}(f_x, f_y) \tag{3.2}$$

where

$$f_x = \frac{x_2}{\lambda f_2} \qquad f_y = \frac{y_2}{\lambda f_2} \tag{3.3}$$

By holographic process, the optical field $O(f_x, f_y)$ at the CCD plane can be retrieved [8-13]. The optical field $P(x_1, y_1)$ at the eye pupil can be obtained by taking inverse FT of it, as follows

$$P(x_1, y_1) = IFT\{O(f_x, f_y)\}(x_1, y_1) \tag{3.4}$$

The holographic process is realized by a modified Mach-Zehnder interferometer as shown by Fig.3.1. A plane wave reference interferes with the object field at a small angle to generate an off-axis hologram from which the object field can be reconstructed [8-13]. The small angle is realized by tilting the beamsplitter BS4 as shown in Fig.3.1. For the phase aberration measurement, a narrow collimated laser beam of diameter about 2mm enters the eye through the aberrator and the eye lens, which forms a focused spot on the retina – the so-called guide star. The light scatters and reflects from the guide star spot and exits the eye with a broad coverage of the aberrator and the eye lens. A guide star hologram is captured by the CCD. The phase aberration, $\phi(x_1, y_1)$, introduced by the aberrator and the system error can be reconstructed from the guide star hologram. For full field imaging, the lens L1 is inserted in the setup. The laser beam is focused at the front focus of the eyes lens, resulting in a collimated illumination of the retina. The exiting distorted field $P(x_1, y_2)$ at the eye pupil can be recovered by the full field hologram. The corrected image can be described by

$$O_c(x_2, y_2) = FT\{P(x_1, y_1)\exp(-j\phi(x_1, y_1))\}(f_x, f_y) \tag{3.5}$$

The corrected image is already focused because the CCD is also at the conjugate plane of the retina. Therefore, further numerical propagation is not necessary. To recover the optical field at

the eye pupil from the digital off axis hologram, the inverse FT is utilized. If the CCD has $M \times N$ square pixels with side length $\Delta x_2 \times \Delta y_2$, then the sampling spacings of the spatial frequency are given by

$$\Delta f_x = \frac{\Delta x_2}{\lambda f_2} \qquad \Delta f_y = \frac{\Delta y_2}{\lambda f_2} \tag{3.6}$$

Then, sampling spacings at pupil plane can be given by [18-20]

$$\Delta x_1 = \frac{\lambda f_2}{M \Delta x_2} \qquad \Delta y_1 = \frac{\lambda f_2}{N \Delta x_2} \tag{3.7}$$

Assume the diameter of the round eye pupil is D, and the dimension of zero order of the hologram is twice the dimension of the image or twin order. To recover the optical field at pupil plane, the pupil size D has to satisfy [14]

$$D \le \frac{\sqrt{2}\lambda f_2}{4\Delta x_2} \tag{3.8}$$

For instance, if λ=0.633μm, f_2=200mm and Δx_2=4.65μm as we adopt in the experiment, then the maximum D can be 9.63mm. In most cases in ocular imaging and microscopy, the size of the pupil will not exceed 8mm. Hence, off-axis holography is sufficient to recover the optical field in these applications.

3.4 Simulations

In the simulation, we use the group 4 elements 2~5 of USAF1951 resolution target to simulate the amplitude of the retina, as shown by Fig. 3.3(a). The field of view is 780μm×780μm. A random phase noise ranging from $-\pi$ to π simulates the phase distribution of the retina, as illustrated by Fig. 3.3(b). All the phase profiles throughout this paper are displayed in blue-white-red colormap that corresponds to $[-\pi\ \pi]$. The wavelength of the laser beam is set to be

0.633μm. As a baseline, the focused image, without the aberrator in place, is given in Fig. 3.3(c). The CCD has 1536×1536 square pixels with pixel size 3.9μm. From Eq.(3.6), the sampling spacing of the spatial frequency along either dimension can be calculated as 0.031 linepairs/mm. The phase aberration is simulated by the Zernike term $4\pi Z_6^2 = 4\pi(15r^6 - 20r^4 + 6r^2)\cos(2\theta)$, as shown in Fig. 3.3(d). The pupil size is set to be 5mm in diameter. Figure 3.3(e) shows the image distorted by the phase aberration. Taking inverse FT of the distorted image field, the optical field at pupil plane can be obtained. The phase map of this field at pupil is represented by Fig. 3.3(f) that is distorted by the phase aberration. The sampling spacing at the eye pupil is 21.1μm, according to Eq. (7). In the guide star process, we set the input beam to be 2mm in diameter. The measured phase map is shown in Fig. 3.3(g). The measurement error is 0.09 wavelengths. Subtracting the measured phase aberration by Fig. 3.3(g) from the distorted optical field represented by Fig. 3.3(f), the corrected optical field at pupil can be obtained, as shown by Fig. 3.3(h). Taking FT of this corrected optical field, the corrected image is achieved, as shown in Fig. 3.3(i). The corrected image shows remarkable improvement in resolution. Other simulation samples for various types and strengths of phase aberrations show the FTDHAO is quite robust, especially for fairly severe aberrations.

3.5 Experimental Results and Discussion

He-Ne laser is used as light source in our experiments. The wavelength is 0.633μm. The first sample under test is a positive USAF 1951 resolution target with a piece of Teflon tape tightly attached behind. The specular reflection is blocked by the pupil whose size is set to be 5mm in diameter. A piece of broken glass serves as the phase aberrator. A set of image data is shown in Fig. 3.4.The field of view on the retinal plane is 573μm×430μm with 1024×768 pixels. The

hologram with full field illumination, without the aberrator in place, is shown in Fig.3.4 (a). The angular spectrum, i.e. the inverse FT of the hologram, is shown in (b), with the highlighted elliptical area on the upper right representing the image-order term for extracting the complex optical field at pupil plane [8-13]. The filtered angular spectrum of (b) is the complex optical field at pupil plane. The phase map of this field is shown in (c). The sampling spacings along horizontal and vertical directions are 26.6μm and 35.4μm respectively. The number of pixels occupied by the elliptical area is 190×140 that corresponds to a circle of diameter 5mm, the same as the actual pupil size. Figure 3.4(e) shows the full field hologram with aberrator in place. The angular spectrum is shown in (f). The phase map of the distorted optical field at pupil is shown in (g). (h) is the distorted image where the resolution is totally lost due to the phase aberration. The guide star hologram is shown in (i). The dashed circle represents a spatial spectral filter with 3.7 linepairs/mm in diameter. The angular spectrum of filtered hologram is shown in (j). The measured phase aberration is given by (k). The RMS of phase distortion is 0.49μm, a rather severe value compared to those expected in the normal population [15].

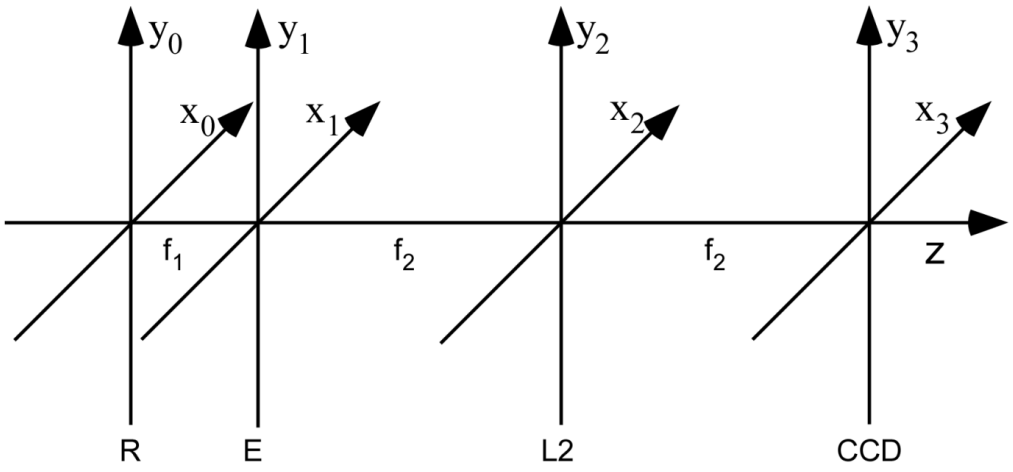

Figure 3.2. Coordinates of the optical system.

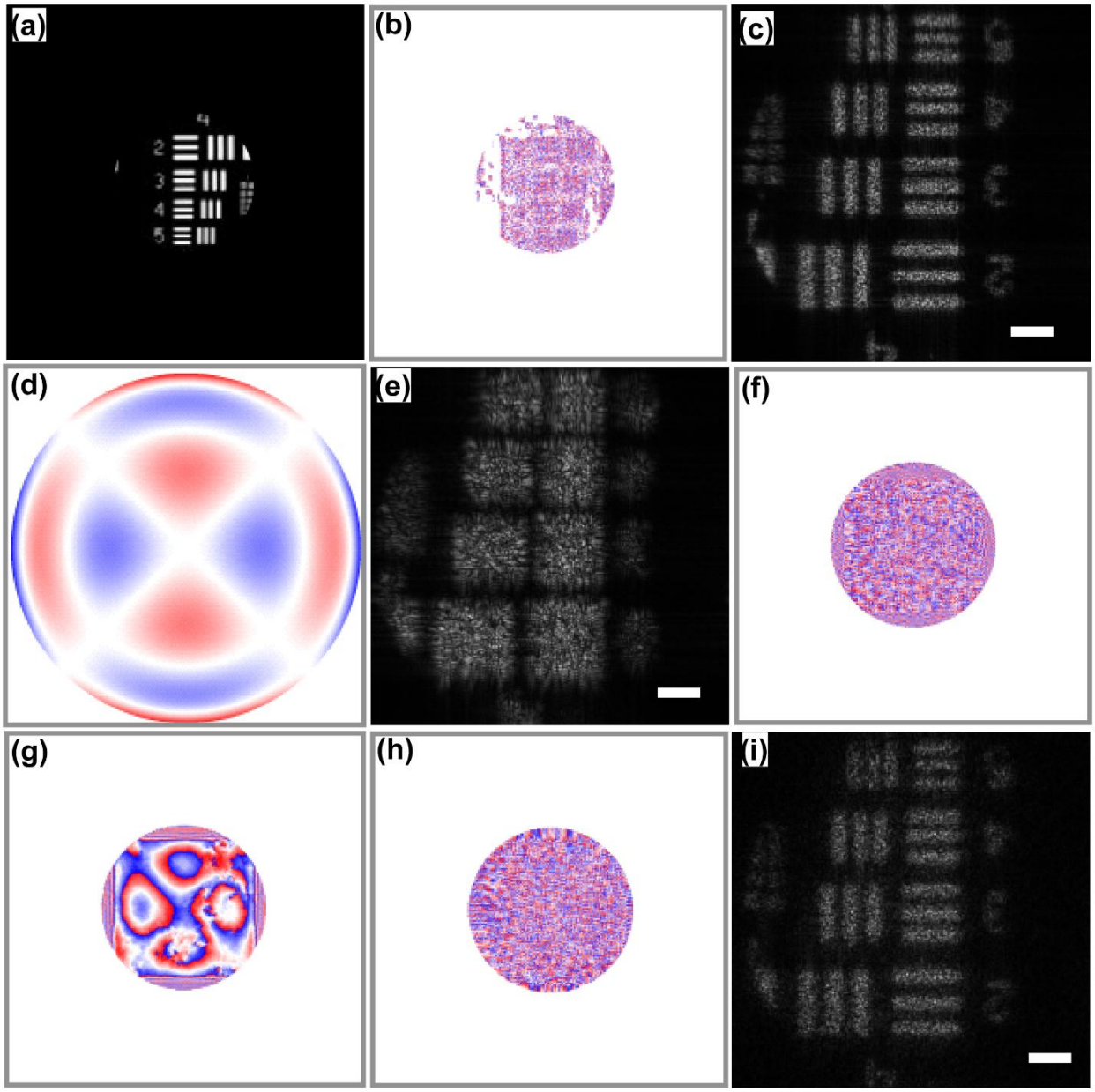

Figure 3.3. Simulations. (a) and (b): Simulated amplitude and phase. The phase map is represented by blue-white-red colormap that corresponds to [-π, π]. (c): Image without aberrator in place. (d): Simulated phase aberration. (e): Distorted image. (f): Phase map of distorted field at the eye pupil. (g): Measured phase aberration at the eye pupil. (h): Phase map of the corrected field at pupil. (i): Corrected image. Scale bar: 100μm.

Subtracting (k) from (g) and taking FT, the corrected image is obtained, as illustrated by (l) that shows significant improvement in resolution and image quality compared with the distorted image given by (h). The resolution is completely recovered by the FTDHAO correction. A proper spatial spectral filter plays important role in phase aberration measurement.

Because the phase aberration has a certain bandwidth, most information lies in a limited spatial frequency range. Outside this range, the information bears negligible effect on compensating for the distorted image. Therefore, a proper filter can recover most phase aberration while effectively reduce the noise for scattering samples. To illustrate this argument, a comparison of corrected images is given in Figs. 3.5(a)-(c) are the phase aberration measurements when filter sizes are 28.4 linepairs/mm, 7.4 linepairs/mm and 0.74 linepairs/mm. The corresponding images are shown in the lower panel from (d)-(f). When the filter is too large, although almost all the phase aberration can be recovered, the noise is too strong and the corrected image is messed up by the noise, as shown by (d). When filter size decreases to 7.4 linepairs/mm, the resolution is recovered while noise still degrades the corrected image quality, as shown in (e). When the filter size is too small, the phase aberration is lost. Therefore, there is no improvement in the corrected image as shown by (f). The optimal filter size depends on the aberration and degree of surface roughness of the target. The filter size will tend to decreases as the degree of surface roughness increases. For this specific sample, the optimal filter size is about 3.7 linepairs/mm.

A second example to be tested is the onion tissue. The experimental results are shown in Fig.3.6. The focused image without aberrator serves as a baseline, as shown in (a). The distorted image is shown in (b). A spatial spectral filter of a diameter 7.4 linepairs/mm is applied to the guide star hologram. The measured phase aberration from this filtered hologram is given by (c). The corrected image is shown in (d) that shows significant improvement in resolution and quality compared to the distorted image by (b).

3.6 Conclusions

A novel DHAO imaging system is proposed. The CCD is located at FT plane of the pupil

of the eye lens. The PSF can be directly visualized, making it practically easy to determine the correct guide star hologram. In FTDHAO, numerical propagation is avoided. The limit of the CCD aperture on the resolution is eliminated and the low coherence or even incoherent illumination becomes possible [2-6]. Although FTDHAO is designed for ophthalmic use, it also shows potential applications in in-depth biomedical microscopy [16, 17]. The basic principles and feasibility of FTDHAO imaging system are demonstrated by simulations and experimental results. FTDHAO is proved to be more compact, flexible and efficient compared to the original DHAO system [1].

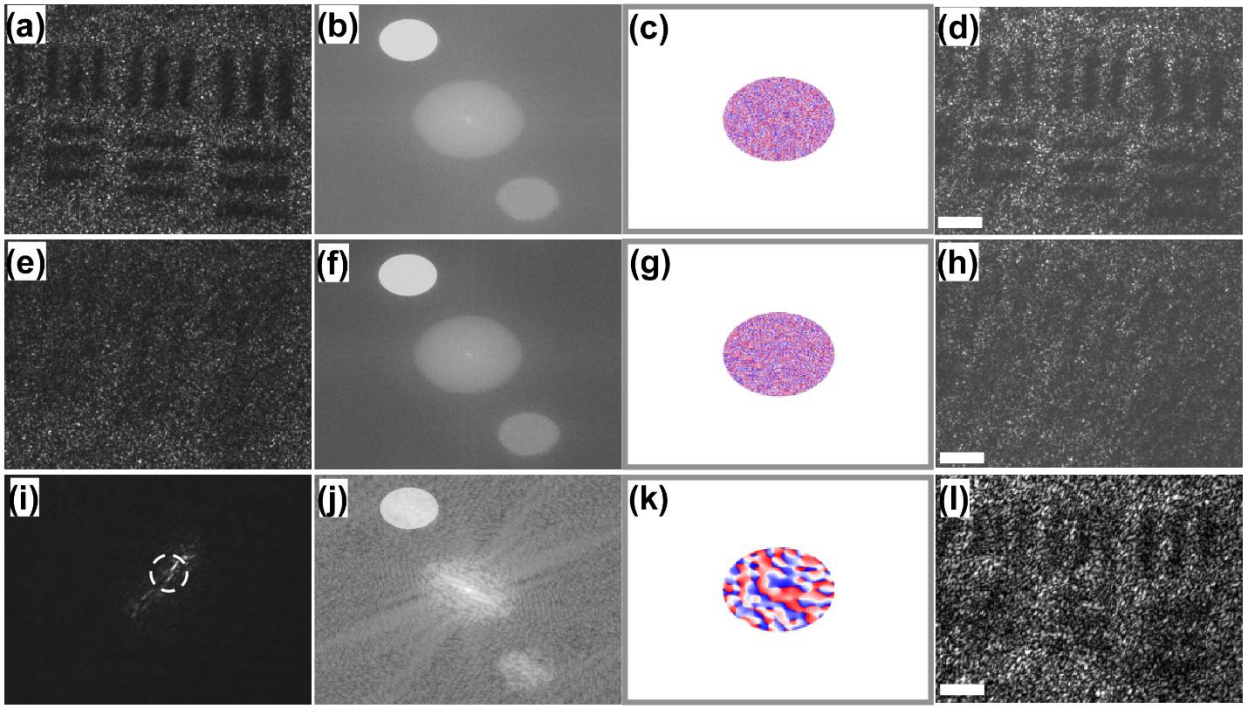

Figure 3.4. Experimental results on USAF 1951 resolution target. (a): Undistorted full-field hologram. (b): Angular spectrum of (a), displayed in logarithmic scale. (c): Phase map of part of (a) filtered by the highlighted elliptical area. (d) Reconstructed baseline image. (e): Distorted full-field hologram. (f): Angular spectrum of (e). (g): Distorted phase map. (f): Distorted image. (i): Guide star hologram. (j): Angular spectrum of part of (i) represented by the dashed circle. (k): Measured phase aberrations. (l): Corrected image. Scale bar: 100μm.

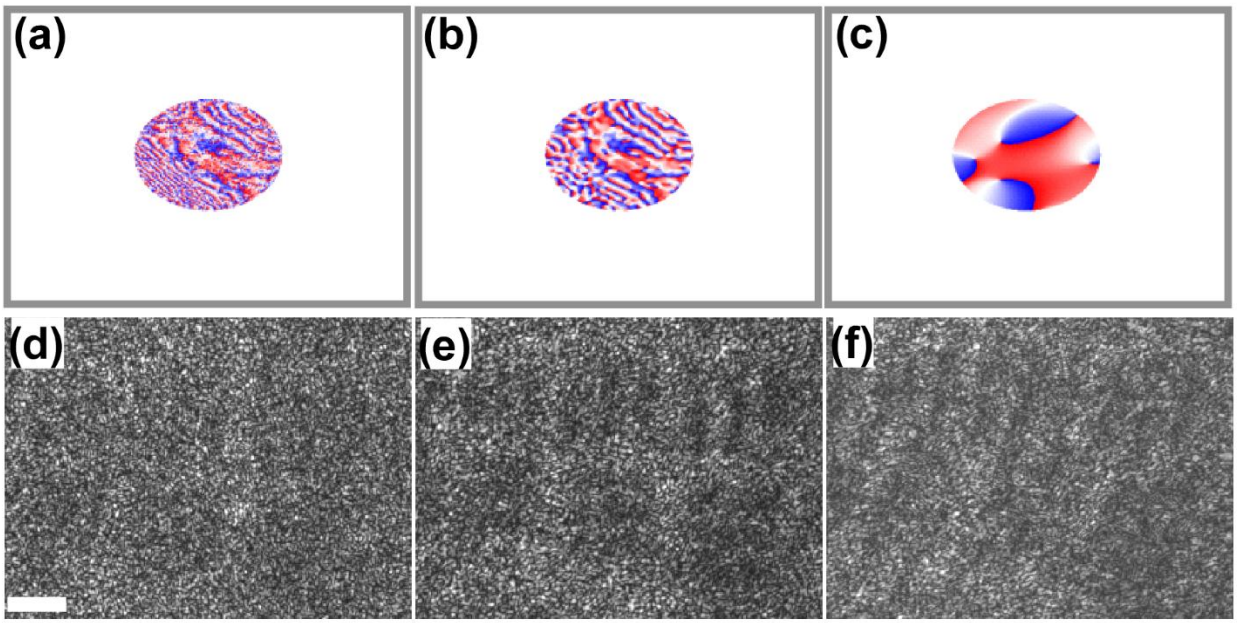

Figure 3.5. Corrected images with varying spatial spectral filters. (a)-(c): Measured phase aberrations with filter diameters 28.4 linepairs/mm, 7.4 linepairs/mm, and 0.74 linepairs/mm respectively. (d)-(e): Corrected images by the phase measurements in upper panel. Scale bar:100μm.

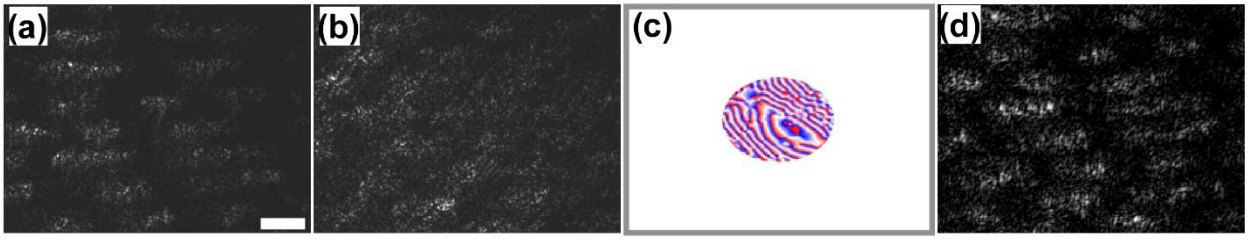

Figure 3.6. FTDHAO on onion tissue. (a): Baseline image. (b): Distorted image. (c): Measured aberration. (d): Corrected image. Scale bar: 100μm.

3.7 References

1. C. Liu, and M. K. Kim, "Digital holographic adaptive optics for ocular Imaging: proof of principle," Opt. Lett. **36**, 2710-2712(2011).

2. F. Dubois, L. Joannes, and J. C. Legros, "Improved three-Ddimensional imaging with digital holography microscope with a source of partial spatial coherence," Appl. Opt. **38** , 7085-7094(1999).

3. G. Pedrini, and H. J. Tiziani, "Short-coherence digital microscopy by use of lensless holographic iImaging system," Appl. Opt. **41**, 4489-4496(2002).

4. M. K. Kim, "Adaptive optics by incoherent digital holography," Opt. Lett. **37**, 2694-2696(2012).

5. F. Dubois, and C. Yourassowsky, "Full off-axis red-green-blue digital holographic microscope with LED illumination," Opt. Lett. **37**, 2190-2192(2012).

6. R. Kelner, and J. Rosen, "Spatially incoherent single channel digital Fourier holography," Opt. Lett. **37**, 3723-3725(2012).

7. J. Goodman, *Introduction to Fourier optics*, 3rd ed. Roberts&Company Publishers, 105-107(2005).

8. U. Schnars and W. Jüptner, "Direct recording of holograms by a CCD target and numerical reconstruction," Appl. Opt. **33**, 179-181(1994).

9. E. Cuche, P. Marquet, and C. Depeursinge, "Digital holography for quantitative phase-contrast imaging," Opt. Lett. **24**, 291-293 (1999).

10. C. Mann, L. Yu, C. Lo, and M. K. Kim, "High-resolution quantitative phase-contrast microscopy by digital holography," Opt. Express. **13**, 8693-8698 (2005).

11. C. Liu, D. Wang, and Y. Zhang, "Comparison and verification of numerical reconstruction methods in digital holography," Opt. Eng. **48**, 1058021-1058027(2009).

12. M. K. Kim, "Principles and techniques of digital holographic microscopy," SPIE Reviews **1**, 1-50 (2010).

13. M. K. Kim, *Digital Holographic Microscopy: Principles, Techniques, and Applications*, Springer Series in Optical Sciences, 55-93 (2011).

14. N. Pavillon, C. S. Seelamantula, J. Kühn, M. Unser, and C. Depeursinge, "Suppression of the zero-order term in off-axis digital holography through nonlinear filtering," Appl. Opt. **48**, H186-H195(2009).

15. K. M. Hampson, "Adaptive optics and vision," J. Mod. Opt. **55**, 3425-3467 (2008).

16. M. J. Booth, "Adaptive optics in microscopy," Phil. Trans. R. Soc. **A 365**, 2829-2843(2007).

17. M. J. Booth, D. Debarre, and A. Jesacher, "Adaptive optics for biomedical microscopy," Opt. Photonics News **January**, 22-29(2012).

Chapter Four:

Digital Holographic Adaptive Optics for General Imaging System

4.1 Introduction

In the original digital holographic adaptive optics system (DHAO), the CCD was put in the image plane of the pupil [1]. Although we can obtain a direct measurement of the wavefront at the pupil, the imaging lens other than the eye lens will introduce spherical curvature that has to be removed by additional matching lens in the reference beam. Also, the correct guide star hologram is difficult to obtain. To get a focused image, numerical propagation is necessary. To address these issues, Fourier transform digital holographic adaptive optics system (FTDHAO) was proposed [2].The CCD is put at the Fourier transform (FT) plane of the pupil, instead of the image plane. No spherical curvature will be induced by the imaging lens. The CCD can directly record the amplitude point spread function (PSF) of the system, facilitating the determination of the correct guide star hologram. In addition, with some modifications, low coherence or even incoherent light source may be incorporated [3-8]. Notwithstanding these advantages over the original DHAO, the correction method in FTDHAO has significant constraint in the optical configuration. In this paper, we present a more general and flexible correction method. FTDHAO becomes a special case of this generalized method. It is realized through the correlation between the complex full field hologram and the guide star hologram after removal of a global quadratic phase term. This correlation operation can eliminate both the aberration at the entrance pupil and the defocus term, obtaining a corrected and focused image, no matter where the CCD is placed.

Except for the assumption that the optical aberrations mainly lie at or close to the pupil plane, the correlation method does not set any other requirement on the optical system. Therefore, it will greatly improve the flexibility of the optical design for AO in vision science and microscopy. The correlation method can not only maintain the merits possessed by FTDHAO, but also be applied for any DHAO systems. It is worth noting that similar method was used in incoherent DHAO [5-6]. However, in principle, it is different from the method presented in this paper. Correlation operation used in incoherent DHAO results in corrected intensity instead of corrected complex amplitude. The observations on the global phase term and the defocus term presented in this paper was not shown in the method for incoherent DHAO [5-6].

Section 4.2 presents a detailed mathematical description of this correction method. In this section, the sampling requirements are also discussed. In section 4.3, three simulation examples are given. Corresponding to the simulations, the experiments are described and discussed in section 4.4. The major conclusions are summarized in section 4.5.

4.2 Theory

A typical DHAO process includes phase aberration measurement, full-field imaging and image correction. The phase aberration is retrieved from a guide star hologram while the full-field image is obtained from a full-field hologram that is distorted by the aberration. The image is recovered by removing the measured phase aberration from the distorted full-field image [1-2]. In this chapter, we treat the correction from a different point of view by taking correlation of the complex full-field hologram with the complex guide star hologram. Although the derivation is based on a two-lens system, the generalization of the conclusion to arbitrary optical systems is straightforward. The coordinates adopted for this two-lens system are illustrated in Fig. 4.1. For

the purpose of brevity, one dimension is adopted in the derivation. Assume the pupil function of the lens L1 is the entrance pupil of the system. The aberration-free pupil function is represented by $P(x_1)$, and the phase aberration at the pupil is denoted by $\Phi(x_1)$.The focal lengths of the lens L1 and L2 are f_1 and f_2 respectively. Distances d_1, d_2 and d_3 are as defined in Fig. 4.1. The amplitude PSF of this system is given by

$$\begin{aligned}
G(x_3,x_0) &= \int_{-\infty}^{+\infty} dx_2 \exp[\frac{j\pi}{\lambda d_3}(x_3-x_2)^2]\exp(-\frac{j\pi}{\lambda f_2}x_2^{\,2}) \\
&\times\{\exp(\frac{j\pi}{\lambda d_2}x_2^{\,2})\int_{-\infty}^{+\infty} dx_1 A(x_0)\exp[\frac{j\pi}{\lambda d_1}(x_1-x_0)^2]P(x_1)\Phi(x_1)\exp(-\frac{j\pi}{\lambda f_1}x_1^{\,2})\exp(\frac{j\pi}{\lambda d_2}x_1^{\,2})\exp(\frac{-j2\pi}{\lambda d_2}x_1x_2)\} \\
&= \exp(\frac{j\pi}{\lambda d_3}x_3^{\,2})\exp(\frac{j\pi}{\lambda d_1}x_0^{\,2})A(x_0)\int_{-\infty}^{+\infty} dx_1 P(x_1)\Phi(x_1)\exp[\frac{j\pi}{\lambda}(\frac{1}{d_1}+\frac{1}{d_2}-\frac{1}{f_1})x_1^{\,2}]\exp(\frac{-j2\pi}{\lambda d_1}x_0x_1) \\
&\times[\int_{-\infty}^{+\infty} dx_2 \exp(\frac{j\pi}{\lambda d_2}x_2^{\,2})\exp(\frac{j\pi}{\lambda d_3}x_2^{\,2})\exp(-\frac{j\pi}{\lambda f_2}x_2^{\,2})\exp(\frac{-j2\pi_1}{\lambda d_2}x_2x_1)\exp(\frac{-j2\pi}{\lambda d_3}x_2x_3)] \\
&= \exp(\frac{j\pi}{\lambda d_3}x_3^{\,2})\exp(\frac{j\pi}{\lambda d_1}x_0^{\,2})A(x_0)\int_{-\infty}^{+\infty} dx_1 P(x_1)\Phi(x_1)\exp[\frac{j\pi}{\lambda}(\frac{1}{d_1}+\frac{1}{d_2}-\frac{1}{f_1})x_1^{\,2}]\exp(\frac{-j2\pi}{\lambda d_1}x_0x_1) \\
&\times\{\int_{-\infty}^{+\infty} dx_2 \exp[\frac{j\pi}{\lambda}(\frac{1}{d_2}+\frac{1}{d_3}-\frac{1}{f_2})x_2^{\,2}]\exp[\frac{-j2\pi}{\lambda}(\frac{x_1}{d_2}+\frac{x_3}{d_3})x_2]\}
\end{aligned} \tag{4.1}$$

where a prefactor is dropped. $A(x_0)$ is the strength of the point source at x_0 of the sample plane, and λ is the wavelength of the illumination. To simplify Eq. (4.1), we define β and γ as

$$\beta = \frac{1}{\frac{1}{d_1}+\frac{1}{d_2}-\frac{1}{f_1}} \text{ and } \gamma = \frac{1}{\frac{1}{d_2}+\frac{1}{d_3}-\frac{1}{f_2}} \tag{4.2}$$

Then, Eq. (4.1) can be rewritten as

$$\begin{aligned}
G(x_3,x_0) &= \exp(\frac{j\pi}{\lambda d_3}x_3^{\,2})\exp(\frac{j\pi}{\lambda d_1}x_0^{\,2})A(x_0)\int_{-\infty}^{+\infty} dx_1 P(x_1)\Phi(x_1)\exp(\frac{j\pi}{\lambda\beta}x_1^{\,2})\exp(\frac{-j2\pi}{\lambda d_1}x_0x_1) \\
&\times\{\int_{-\infty}^{+\infty} dx_2 \exp(\frac{j\pi}{\lambda\gamma}x_2^{\,2})\exp[\frac{-j2\pi}{\lambda}(\frac{x_1}{d_2}+\frac{x_3}{d_3})x_2]\} \\
&= \exp[\frac{j\pi}{\lambda}(\frac{1}{d_3}-\frac{\gamma}{d_3^{\,2}})x_3^{\,2}]\exp(\frac{j\pi}{\lambda d_1}x_0^{\,2})A(x_0) \\
&\times\int_{-\infty}^{+\infty} dx_1 P(x_1)\Phi(x_1)\exp[\frac{j\pi}{\lambda}(\frac{1}{\beta}-\frac{\gamma}{d_2^{\,2}})x_1^{\,2}]\exp[-j2\pi(\frac{\gamma x_3}{\lambda d_2 d_3}+\frac{x_0}{\lambda d_1})x_1]
\end{aligned} \tag{4.3}$$

To further simplify Eq. (4.3), we define the general pupil function as

$$P_1(x_1) = P(x_1)\Phi(x_1)\Phi_d(x_1) \tag{4.4}$$

where

$$\Phi_d(x_1) = \exp[\frac{j\pi}{\lambda}(\frac{1}{\beta} - \frac{\gamma}{d_2^{\,2}})x_1^{\,2}] \tag{4.5}$$

which is the defocus term of the system. The defocus term becomes unity if the CCD is at image plane of the sample. Now, Eq. (4.1) can be simplified as

$$G(x_3, x_0) = \exp[\frac{j\pi}{\lambda}(\frac{1}{d_3} - \frac{\gamma}{d_3^{\,2}})x_3^{\,2}]\exp(\frac{j\pi}{\lambda d_1}x_0^{\,2})A(x_0)T(\frac{\gamma d_1}{d_2 d_3}x_3 + x_0) \tag{4.6}$$

where

$$T(\frac{\gamma d_1}{d_2 d_3}x_3 + x_0) = FT\{P_1(x_1)\}|_{f_x = \frac{1}{\lambda d_1}(\frac{\gamma d_1}{d_2 d_3}x_3 + x_0)} \tag{4.7}$$

where the FT denotes Fourier transform. The complex amplitude of the optical field of an extended object at the CCD plane is obtained by superposition of the amplitude PSF of all the source points, which is given by

$$O(x_3) = \Phi_q(x_3)\int_{-\infty}^{+\infty} dx_0 \exp[\frac{j\pi}{\lambda d_1}(x_0^{\,2})]A(x_0)T(\frac{\gamma d_1}{d_2 d_3}x_3 + x_0) \tag{4.8}$$

where $\Phi_q(x_3)$ is given by

$$\Phi_q(x_3) = \exp[\frac{j\pi}{\lambda}(\frac{1}{d_3} - \frac{\gamma}{d_3^{\,2}})x_3^{\,2}] \tag{4.9}$$

This quadratic phase term appears outside the integrals in Eq. (4.6) and Eq. (4.8). It plays a crucial role in the image correction, as will be validated in the following two sections. From the guide star hologram, we can obtain the amplitude PSF given by Eq. (4.6) . Removing $\Phi_q(x_3)$ from the amplitude PSF and setting the source point at origin, we can obtain a modified amplitude PSF, as follows

$$G_1(x_3) = A_0 T(\frac{\gamma d_1}{d_2 d_3}x_3) \tag{4.10}$$

Similarly, a modified field of the extended object can be obtained from the full-field hologram

and numerical removal of the quadratic phase term $\Phi_q(x_3)$, as follows

$$O_1(x_3) = \int_{-\infty}^{+\infty} dx_0 \exp[\frac{j\pi}{\lambda d_1}(x_0^2)]A(x_0)T(\frac{\gamma d_1}{d_2 d_3}x_3 + x_0) \tag{4.11}$$

Correlating this modified field with the modified amplitude PSF given by Eq. (4.10), we have

$$\begin{aligned} O_1 \odot G_1(x_3) &= A_0 \int_{-\infty}^{+\infty}\int_{-\infty}^{+\infty} d\alpha dx_0 \exp[\frac{j\pi}{\lambda d_1}(x_0^2)]A(x_0)T(\frac{\gamma d_1}{d_2 d_3}x_3 + x_0 + \frac{\gamma d_1}{d_2 d_3}\alpha)T^*(\frac{\gamma d_1}{d_2 d_3}\alpha) \\ &= \frac{d_2 d_3 A_0}{\gamma d_1}\int_{-\infty}^{+\infty}\int_{-\infty}^{+\infty} d\alpha dx_0 \exp[\frac{j\pi}{\lambda d_1}(x_0^2)]A(x_0)T(\frac{\gamma d_1}{d_2 d_3}x_3 + x_0 + \alpha)T^*(\alpha) \end{aligned} \tag{4.12}$$

where $\odot$ denotes correlation. According to the definition in Eq. (4.7), we have

$$T(x_0 + \frac{\gamma d_1}{d_2 d_3}x_3 + \alpha) = \int_{-\infty}^{+\infty} d\eta P_1(\eta)\exp[\frac{-j2\pi}{\lambda d_1}\eta(x_0 + \frac{\gamma d_1}{d_2 d_3}x_3 + \alpha)] \tag{4.13}$$

and

$$T^*(\alpha) = \int_{-\infty}^{+\infty} dx P_1^*(x)\exp(\frac{j2\pi}{\lambda d_1}\alpha x) \tag{4.14}$$

Plugging Eqs. (4.13) and (4.14) into Eq. (4.12), the correlation operation results in

$$\begin{aligned} O_1 \odot G_1(x_3) &= \frac{d_2 d_3 A_0}{\gamma d_1}\int_{-\infty}^{+\infty}\int_{-\infty}^{+\infty} d\alpha dx_0 \exp[\frac{j\pi}{\lambda d_1}(x_0^2)]A(x_0) \\ &\quad \times\{\int_{-\infty}^{+\infty} d\eta P_1(\eta)\exp[\frac{-j2\pi}{\lambda d_1}\eta(x_0 + \frac{\gamma d_1}{d_2 d_3}x_3 + \alpha)]\int_{-\infty}^{+\infty} dx P_1^*(x)\exp(\frac{j2\pi}{\lambda d_1}\alpha x)\} \\ &= \frac{d_2 d_3 A_0}{\gamma d_1}\int_{-\infty}^{+\infty} dx_0 \exp[\frac{j\pi}{\lambda d_1}(x_0^2)]A(x_0) \\ &\quad \times\int_{-\infty}^{+\infty}\int_{-\infty}^{+\infty} dx d\eta P_1^*(x)P_1(\eta)\exp[\frac{-j2\pi}{\lambda d_1}\eta(x_0 + \frac{\gamma d_1}{d_2 d_3}x_3)]\{\int_{-\infty}^{+\infty} d\alpha \exp[\frac{j2\pi}{\lambda d_1}(x-\eta)\alpha]\} \\ &= \frac{\lambda d_2 d_3 A_0}{\gamma}\int_{-\infty}^{+\infty} dx_0 \exp(\frac{j\pi}{\lambda d_1}x_0^2)A(x_0)\int_{-\infty}^{+\infty} dx P(x)\exp[\frac{-j2\pi}{\lambda d_1}x(x_0 + \frac{\gamma d_1}{d_2 d_3}x_3)] \end{aligned} \tag{4.15}$$

From Eq. (4.15), the correlation operation removes both the aberration term $\Phi(x_1)$ and the defocus term $\Phi_d(x_1)$, obtaining a corrected and focused image no matter where the CCD is put. The magnification of this corrected image is given by $-\frac{d_2 d_3}{\gamma d_1}$. Although our derivation is based on a two-lens system, the conclusion thus rendered can be generalized to any optical system. The

difference lies in the specific expressions for the defocus term $\Phi_d(x_1)$ and the global quadratic phase term $\Phi_q(x_3)$. According to the convolution theorem, Eq. (4.15) can be implemented by

$$O_1 \otimes G_1(x_3) = IFT\{FT\{O_1(x_3)\}FT^*\{G_1(x_3)\}\} \tag{4.16}$$

where IFT denotes the inverse Fourier transform and $\otimes$ represents convolution operation. $O(x_3)$ and $G(x_3)$ can be obtained through off-axis holography [9-13]. Eliminating the quadratic phase term $\Phi_q(x_3)$ from $O(x_3)$ and $G(x_3)$, we can get $O_1(x_3)$ and $G_1(x_3)$. To achieve the fields $O_1(x_3)$ and $G_1(x_3)$ correctly, the sampling requirements have to be taken into account. Taking FT of the amplitude PSF of the source point at origin, we have

$$\begin{aligned} FT\{G(x_3,0)\} &= A_0 FT\{\exp[\frac{j\pi}{\lambda}(\frac{1}{d_3}-\frac{\gamma}{d_3^{\,2}})x_3^{\,2}]T(\frac{\gamma d_1}{d_2 d_3}x_3)\} \\ &= A_0 FT\{\exp[\frac{j\pi}{\lambda}(\frac{1}{d_3}-\frac{\gamma}{d_3^{\,2}})(\frac{\lambda d_2 d_3}{\gamma})^2 f_x^{\,2}]\} \otimes FT\{FT\{P_1(x_1)\}(f_x)\} \\ &= \frac{A_0\gamma}{d_2\sqrt{-j\lambda(d_3-\gamma)}}\exp[\frac{-j\pi\gamma^2}{\lambda(d_3-\gamma)d_2^{\,2}}x_1^{\,2}] \otimes P_1(-x_1) \end{aligned} \tag{4.17}$$

where f_x is the spatial frequency in the horizontal direction,

$$f_x = \frac{\gamma}{\lambda d_2 d_3}x_3 \tag{4.18}$$

Expanding the Eq. (4.17), it becomes the spectrum of a finite chirp function. The width of this spectrum can estimated as that of the general pupil function [14-15]. Because the sampling requirement for the one dimensional case is different from that for the two dimensional case, let us now consider the two dimensional case. If the CCD has $M \times N$ square pixels with side length Δx_3, then the sampling spacings of the spatial frequency along the horizontal and vertical dimensions are given by

$$\Delta f_x = \Delta f_y = \frac{\gamma}{\lambda d_2 d_3}\Delta x_3 \tag{4.19}$$

Then the sampling spacings on two dimensions at the pupil plane are given by [11]

$$\Delta x_1 = \frac{\lambda d_2 d_3}{N \gamma \Delta x_3} \text{ and } \Delta y_1 = \frac{\lambda d_2 d_3}{M \gamma \Delta x_3} \tag{4.20}$$

Assume the diameter of a round pupil is *D* that is estimated as the width of the image order of the hologram, and the width of zero order of the hologram is twice that of the image order. To recover the optical field at the pupil plane, the pupil size *D* has to satisfy [16]

$$D \le \frac{\sqrt{2}\lambda d_2 d_3}{4\gamma \Delta x_3} \tag{4.21}$$

Finally, it is worth mentioning that a special case of the correlation method is FTDHAO, where d_2 and d_3 are equal to f_2 [7]. Then Eq. (4.21) evolves into the expression for the sampling requirement in FTDHAO.

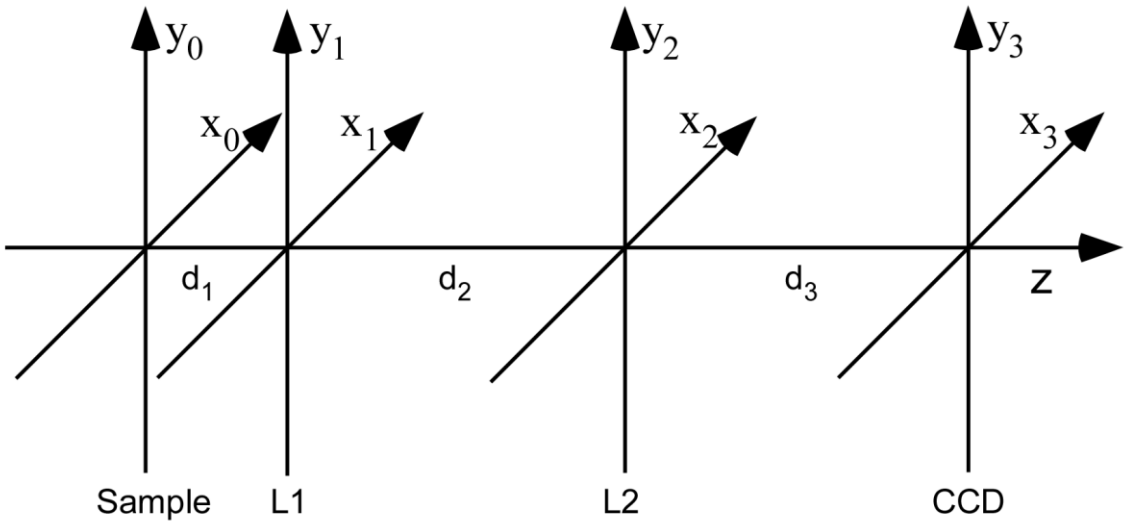

Figure 4.1. Coordinates for a two-lens optical system.

4.3 Simulations

In the simulations, the focal lengths, f_1 and f_2, of the lens L1 and L2 are set to be 25mm and 200mm respectively. We set d_1, the distance between the sample and the lens L1, to be

25mm. The group 4 elements 2~5 of USAF1951 resolution target are used to simulate the amplitude of the sample, as shown by Fig. 4.2(a). The field of view is 780μm×780μm. The pixel pitch is 3.9μm. A random phase noise ranging from $-\pi$ to π simulates the phase distribution of the sample, as illustrated by Fig. 4.2(b). All the phase profiles throughout this paper are displayed in blue-white-red colormap that corresponds to $[-\pi\ \pi]$. The wavelength of the laser beam is set to be 0.633μm. We present three simulation samples, corresponding to three different combinations of d_2 and d_3. In the first case, d_2 is set to be 200mm and d_3 to be 150mm. Then γ is calculated as 150mm, according to Eq. (4.2), and Φ_q becomes unity. The CCD is put at a defocus plane of the sample. The defocus term Φ_d is given by Eq. (4.5). The simulation results are presented in Fig. 4.2. Figure 4.2(c) is the undistorted but defocused field at the CCD plane when no aberration is added at the pupil plane. The sampling spacing of the spatial frequency in either direction is 0.031linepairs/mm. For the purpose of comparison, we propagate it to the image plane. The undistorted focused image is shown in Fig. 4.2(d). Figure 4.2(e) shows the simulated phase aberration Φ added at the pupil plane, which is given by two sixth-order Zernike polynomials $4\pi(Z_6^2 + Z_6^4) = 4\pi(15r^6 - 20r^4 + 6r^2)[\cos(2\theta) + \sin(2\theta)]$. From the full-field hologram, we can retrieve the field at the CCD plane that is distorted by this added phase aberration Φ, as shown in Fig. 4.2(f). Propagating this distorted field to the focal plane, we can obtain the focused but degraded image, as shown by Fig. 4.2(g). Taking FT of the distorted field shown by Fig. 4.2(f) results in the distorted field at the pupil, which contains both the added aberration Φ and the defocus term Φ_d, as shown in Fig. 4.2(h). The spatial sampling spacing of this distorted field is 21μm. From the guide star hologram, the amplitude PSF of the system is obtained, which is shown in Fig. 4.2(i). The general pupil function that is the FT of the amplitude PSF is shown in Fig. 4.2(j). The Root-Mean-Square (RMS) measurement error of the phase of the general pupil

function is 0.97 radian that corresponding to about 0.15 wavelengths. Subtracting Fig. 4.2(j) from Fig. 4.2(h), we can get the corrected field at the pupil, which is given by Fig. 4.2(k). As described by Eq. (4.16), the corrected image can be obtained by taking IFT of Fig. 4.2(k), which is shown in Fig. 4.2(l). Compared to the defocused and distorted field in Fig. 4.2(f), the correlation operation eliminates the aberration and meanwhile automatically focuses the corrected field.

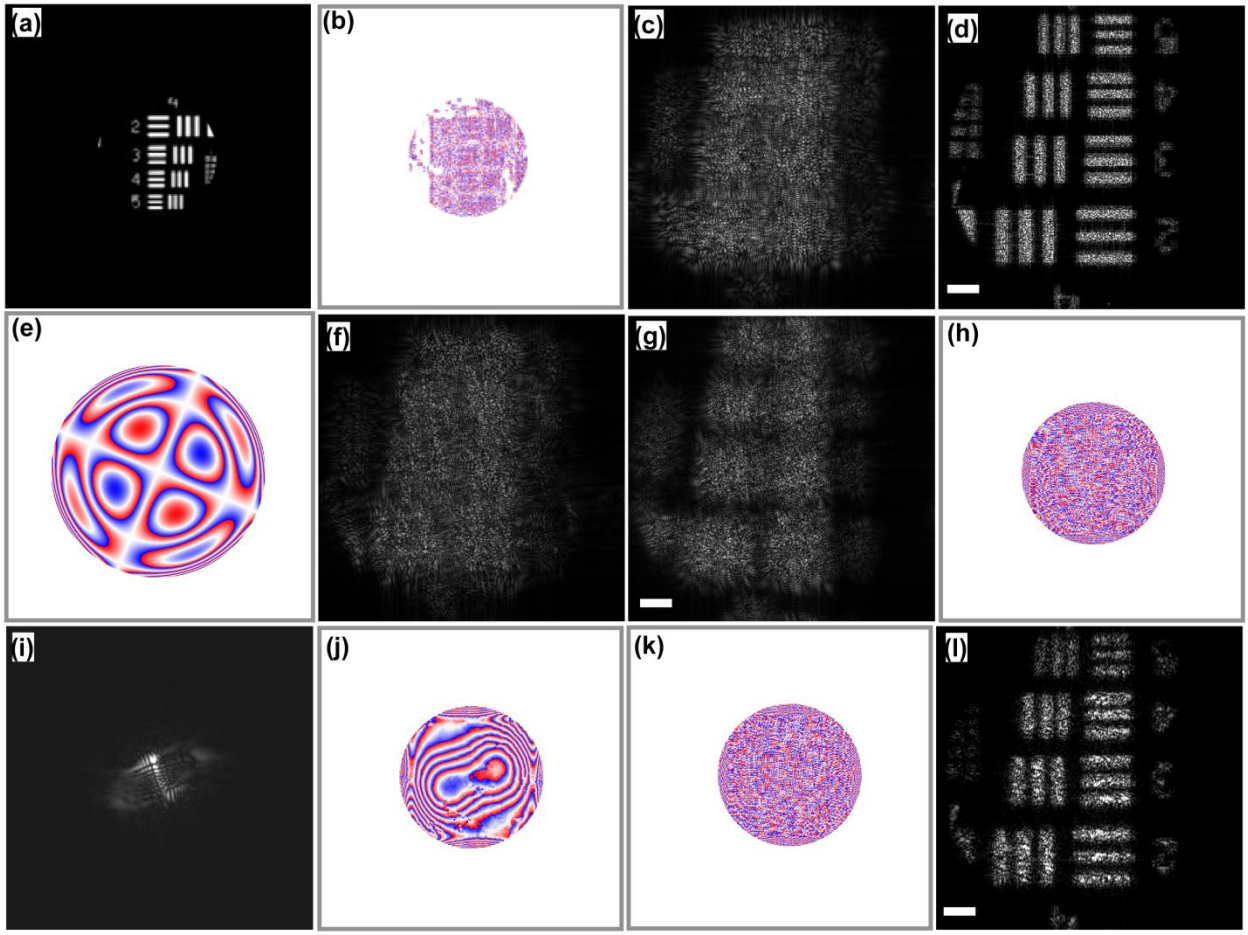

Figure 4.2. Simulation example where the defocus term Φ_d exists and the global quadratic phase term Φ_q is unity. (a) and (b): Simulated amplitude and phase. The phase maps are represented by blue-white-red colormap that corresponds to $[-\pi, \pi]$. (c): Optical field at the CCD plane without aberrator in place. (d): Focused image of (c). (e): Simulated phase aberration Φ. (f): Full-field aberrated hologram at the CCD plane. (g): Focused image of (f). (h): Full-field phase profile at the pupil with aberration. (i): Guide star hologram, i.e. the amplitude PSF of the system. (j): General pupil function that is the FT of (i). (k): Corrected field at the pupil. (l): Corrected image from (k).

In the second case, d_2 is set to be 300mm and d_3 to be 200mm. The defocus term Φ_d

becomes unity, which signifies the CCD is at the image plane of the sample. However, in this scheme, the global quadratic phase term Φ_q is not unity, which is given by Eq. (4.9). The simulation results are shown in Fig. 4.3. The baseline image, without aberration in place, is shown in Fig. 4.3(a). Figure 4.3(b) shows the image distorted by the aberration Φ illustrated in Fig. 4.2(e). Figure 4.3(c) shows the affected field at the pupil. The amplitude PSF of this system is shown in Fig. 4.3(d). The measured aberration at the pupil is given by Fig. 4.3(e). The RMS measurement error of the phase of the general pupil function is 0.91 radian that corresponding to about 0.14 wavelengths. Figure 4.3(f) illustrates the corrected image that shows remarkable improvement in resolution and quality, compared to the distorted image in Fig. 4.3(b). In this case, removal of the quadratic phase term Φ_q before the correlation operation is found to be of significance in the correction. The effect of this term on the corrected image is shown in Fig. 4.4. Figure 4.4(a) shows the measured aberration at the pupil when Φ_q is not eliminated before the correlation operation, and Fig. 4.4(c) illustrates the corresponding corrected image which is much degraded compared to Fig. 4.3(f) that is obtained with Φ_q removed. If Φ_q is partially removed, the recovered image becomes better, compared to that with Φ_q untreated. Figure 4.4(b) shows the measured aberration at the pupil when Φ_q is partially eliminated, and Fig. 4.4(d) shows the corresponding corrected image.

The third simulation sample demonstrates a general case where both Φ_q and Φ_d exist. In this case, we set d_2 to be 300mm and d_3 to be 150mm. The simulation results are shown in Fig. 4.5. Figure. 4.5(a) shows the distorted full field at the CCD plane that is defocused and distorted. Note that the quadratic phase term Φ_q has been eliminated. The focused but distorted image is shown in Fig. 4.5(b). The distorted field at the pupil is given by Fig. 4.5(c), which includes the added aberration Φ and defocus term Φ_d. The amplitude PSF of this system is shown in Fig.

4.5(d). Again, the quadratic phase term Φ_q has been eliminated. The FT of this amplitude PSF is given by Fig. 4.5(e) that includes Φ and Φ_d. The RMS measurement error of the phase map represented by Fig. 4.5(e) is 0.88 radian that corresponding to about 0.14 wavelengths. Removing Fig. 4.5(d) from Fig. 4.5(c) and taking IFT, we can get the corrected image shown in Fig. 4.5(f). The resolution is completely recovered and the defocus is eliminated.

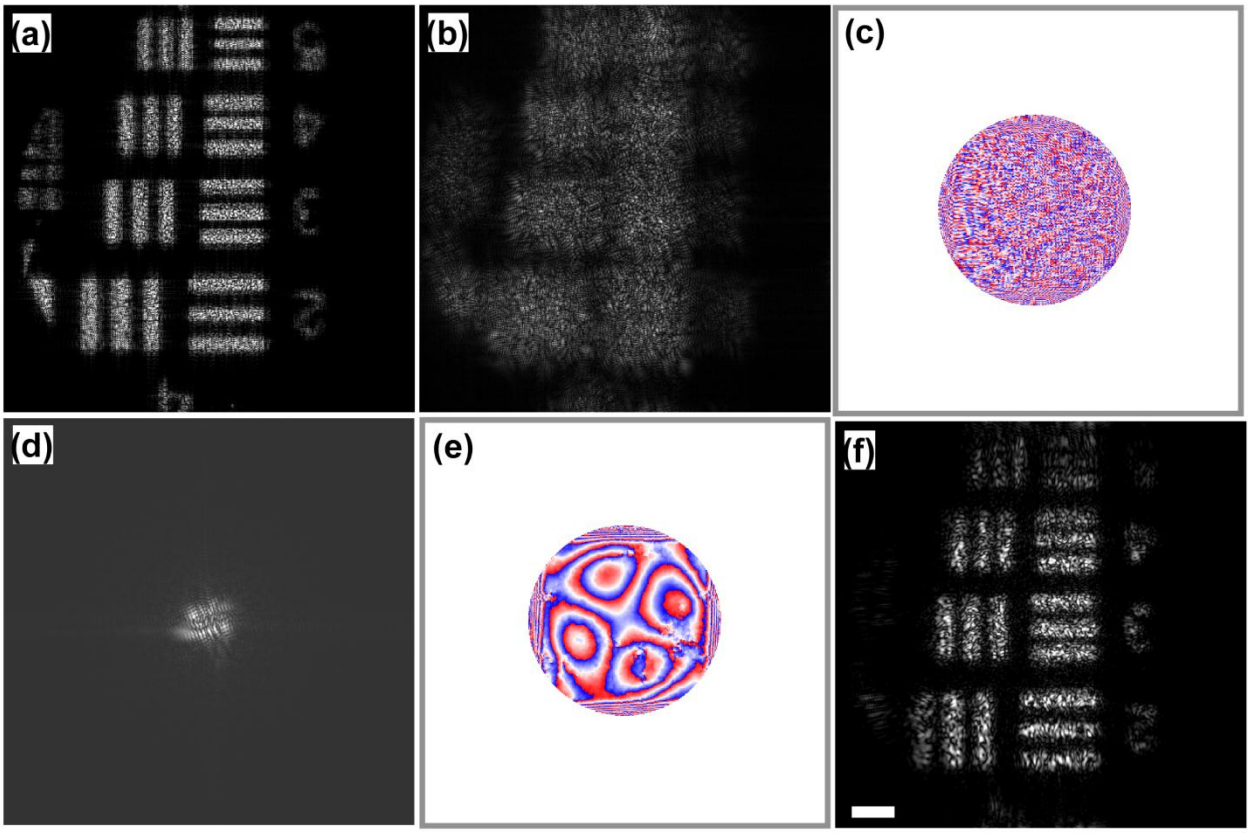

Figure 4.3. Simulation example where Φ_q exists while Φ_d is unity. (a): Undistorted optical field at CCD plane. (b): Distorted field at the CCD plane. (c): Distorted field at the pupil. (d): Amplitude PSF of the system. (e): General pupil function. (f): Corrected image.

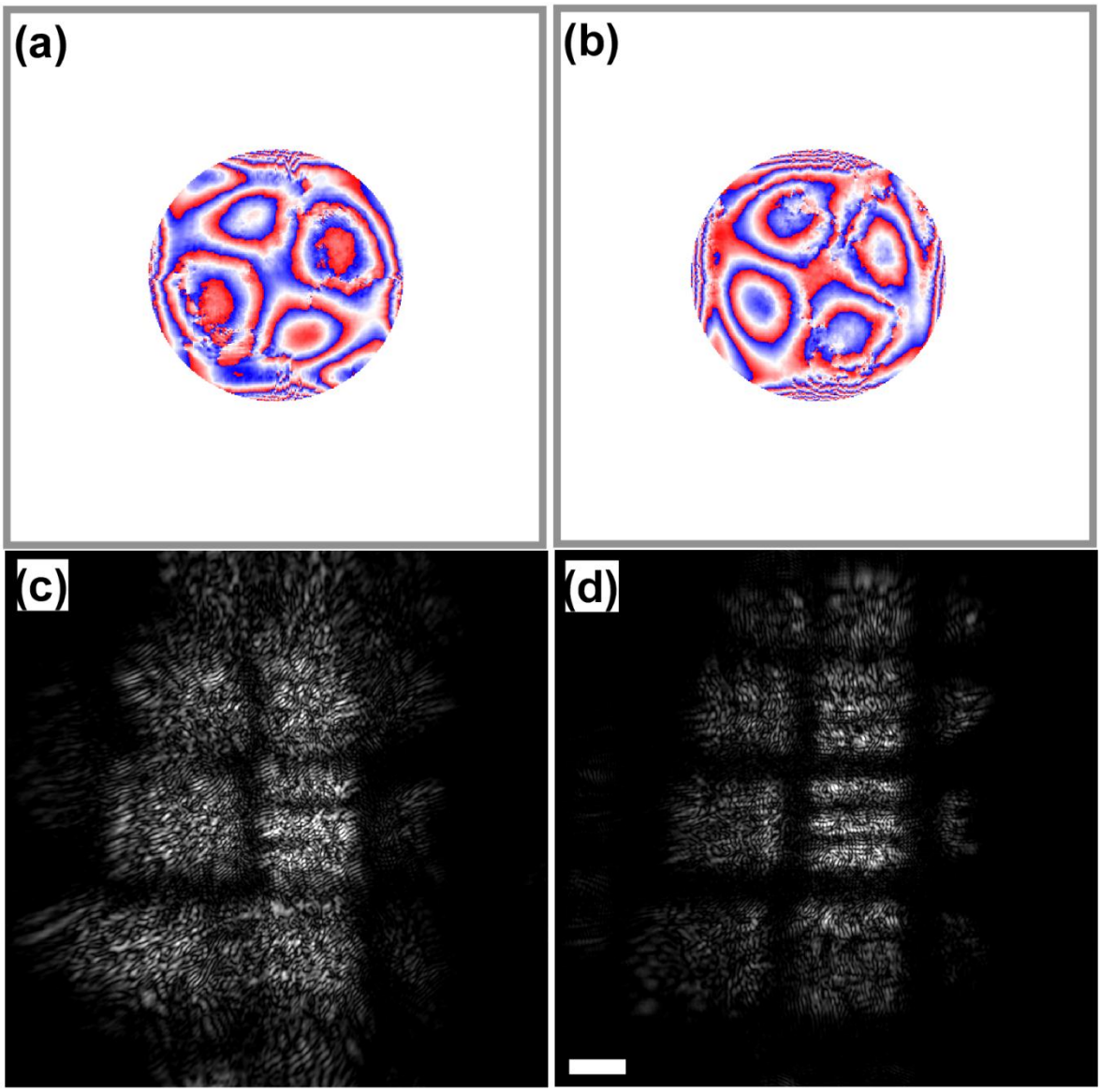

Figure 4.4. Demonstration of the effect of Φ_q on the corrected image. (a): Measured aberration at the pupil when Φ_q is not eliminated. (b): Measured aberration at the pupil when Φ_q is partially eliminated. (c): Image corrected by (a). (d): Image corrected by (b).

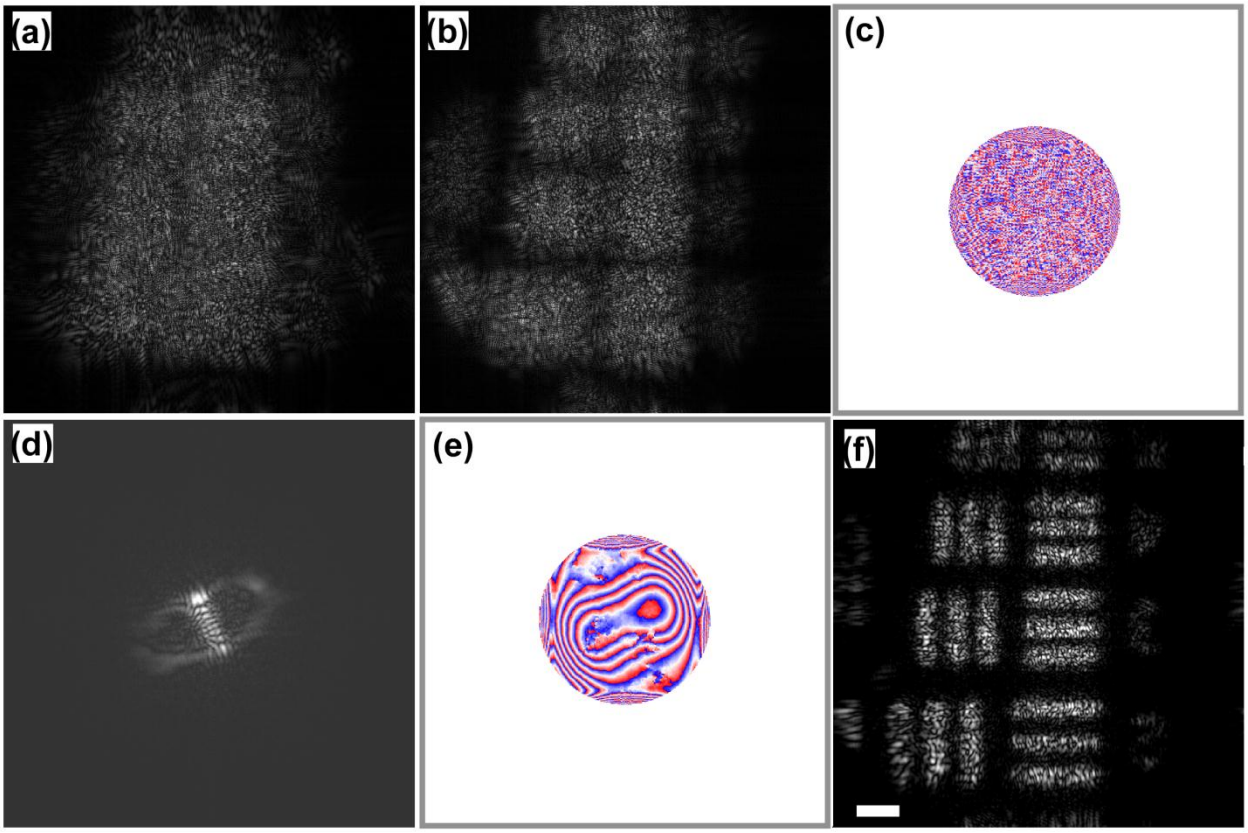

Figure.4.5. Simulation example where both Φ_q and Φ_d exist. (a): Distorted optical field at the CCD plane. (b): Distorted image. (c): Distorted field at the pupil. (d): Amplitude PSF of the system. (e): General pupil function. (f): Corrected image.

4.4 Experimental Results

The schematic diagram of the experimental setup is illustrated in Fig. 4.6. The focal length f_1 of the lens L1 is 25mm. S represents the sample plane that is at the back focal plane of eye lens E. Hence, d_1 equals 25mm. The phase aberrator A is close to the pupil of the lens L1. The focal length f_2 of L2 is 200mm. The CCD has 1024×768 pixels with the pixel pitch 6.45μm. In our experiments, He-Ne laser is used as light source. The sample under test is a positive USAF 1951 resolution target with a piece of Teflon tape tightly attached behind. The specular reflection is blocked by the pupil whose size is set to be 5mm in diameter, and the CCD receives

the diffuse scattered light from the Teflon tape. A piece of clear broken glass serves as the phase aberrator. The lens L3 is inserted for full-field illumination.

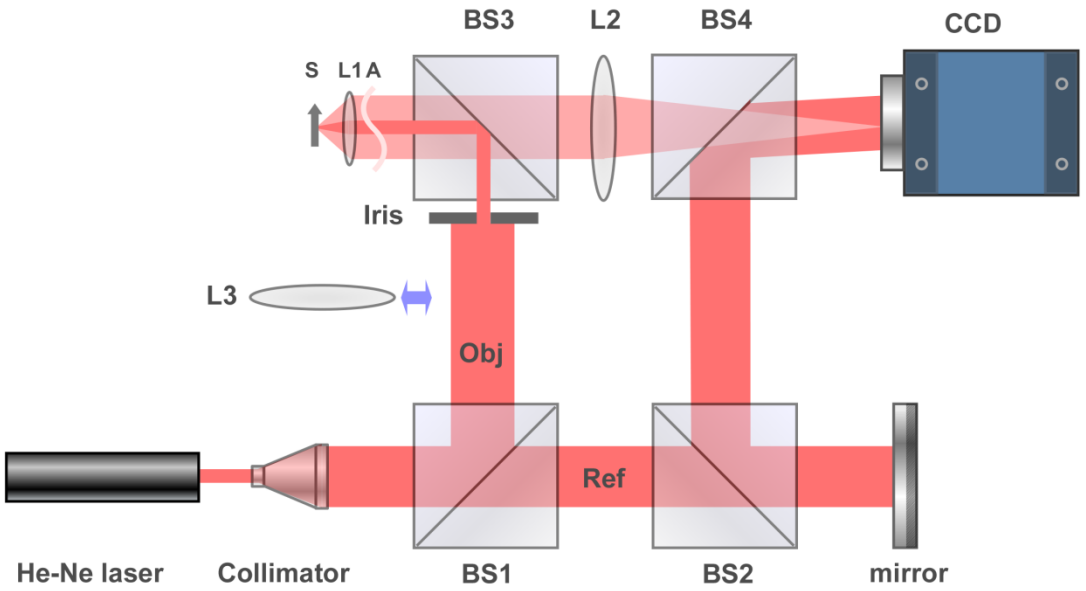

Figure 4.6. The schematic diagram of the experimental apparatus. S: Sample. L1-L3: lens. A: aberrator. BS1- BS 4: beamsplitters.

Corresponding to the three simulation cases, we present three experimental examples by choosing different values of d_2 and d_3. In the first example, we set d_2 to be 200mm and d_3 to be 150mm, which indicates the CCD is at a defocus plane of the sample. The defocus term Φ_d is calculated by Eq. (4.5). According to Eq. (4.9), the quadratic phase term Φ_q becomes unity. A set of image data is shown in Fig. 4.7. The field of view on the sample plane is 594μm×445μm. The full-field hologram, without the aberrator in place, is shown in Fig. 4.7(a). By the holographic process, the complex optical field at the CCD plane can be achieved, which is shown in Fig. 4.7(b) [2-6]. The sampling spacing of the spatial frequency at the CCD plane is 0.037 linepairs/mm in either direction, according to Eq. (4.19). Taking FT of this field, the full optical field at the pupil is obtained, as shown in Fig. 4.7(c). According to Eq. (4.20), the spatial sampling spacings along the horizontal and vertical directions are 27μm and 35μm respectively.

For the purpose of comparison, we propagate this defocused field at the CCD plane illustrated by Fig. 4.7(b) to the image plane, and obtain the undistorted focused image shown in Fig. 4.7(d), serving as a baseline. The distorted full-field hologram is shown in Fig. 4.7(e), from which we can get the distorted and defocused field at the CCD plane, as shown in Fig. 4.7(f).The distorted full field at the pupil is shown in Fig. 4.7(g), which contains the added aberration and the defocus term. Figure 4.7(h) is the distorted image. The guide star hologram is shown in Fig. 4.7(i), from which we obtain the amplitude PSF of the system that is illustrated by Fig. 4.7(j). Figure 4.7(k) shows the general pupil function. Subtracting Fig. 4.7(k) from Fig. 4.7(g), we get the corrected field at the pupil. As described by Eq. (4.16), the corrected image can be obtained by taking IFT of this corrected field, which is shown in Fig. 4.7(l). Compared to the defocused and distorted field in Fig. 4.7(f), the correlation operation eliminates both the aberration and the defocus term.

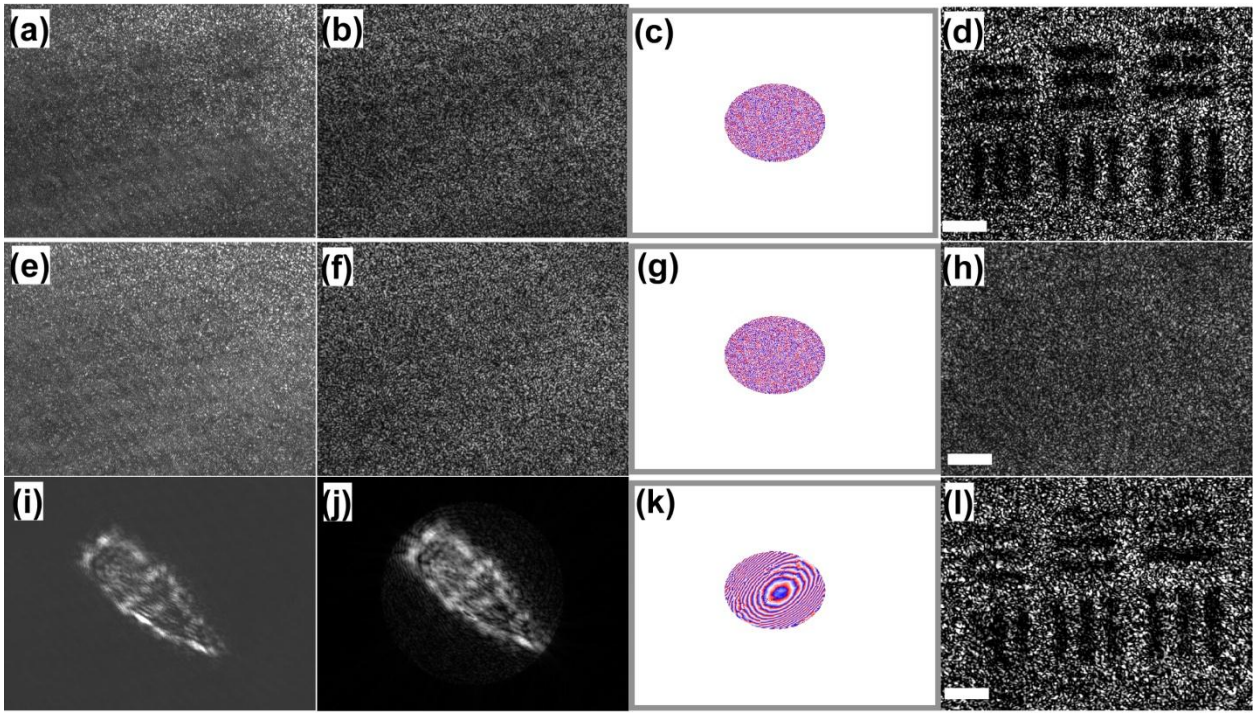

Figure 4.7. Experimental example where the defocus term Φ_d exists while the global quadratic phase term Φ_q is unity. (a): Hologram without aberration. (b): Amplitude at the CCD plane. (c): Undistorted field at the pupil. (d): Undistorted image. (e): Distorted hologram. (f): Distorted field at the CCD plane. (g): Distorted field at the pupil. (h): Distorted image. (i): Guide star hologram. (j): Amplitude PSF of the system. (k): General pupil function. (l): Corrected image.

In the second example, we set d_2 to be 150mm and d_3 to be 200mm, which indicates the CCD is at the image plane of the sample. The defocus term Φ_d disappears while the quadratic phase term Φ_q exists. Figure 4.8(a) shows the baseline image. The distorted image is illustrated by Fig. 4.8(b). Figure 8(c) shows the distorted full field at the pupil. The amplitude PSF of the system is illustrated by Fig. 4.8(d). Figure 4.8(e) is the measured aberration at the pupil. The recovered image is shown in Fig. 4.8(f). The resolution and contrast are almost completely recovered. Note that the quadratic phase term Φ_q has to be removed before the correlation operation. The effect of this term on the corrected image is also demonstrated in this example, shown in Fig. 4.9. Figure 4.9(a) shows the measured aberration at the pupil when Φ_q is not eliminated before the correlation operation, and Fig. 4.9(c) shows corresponding corrected image which is rather blurred compared to Fig. 4.8(f). When Φ_q is partially removed, the recovered image becomes better. Figure 4.9(b) shows the measured aberration at the pupil when Φ_q is partially eliminated and Fig. 4.9(d) shows the corresponding corrected image.

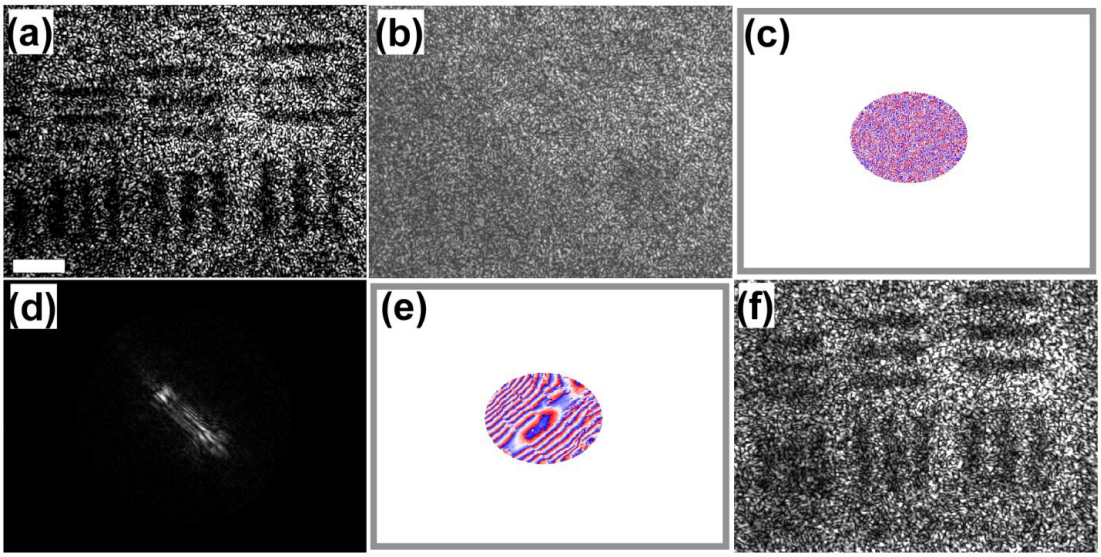

Figure 4.8. Experimental example where Φ_q exists while Φ_d takes unity. (a): Undistorted image. (b): Distorted image. (c): Distorted full field at the pupil. (d): Amplitude PSF of the system. (e): Measured aberration. (f): Corrected image.

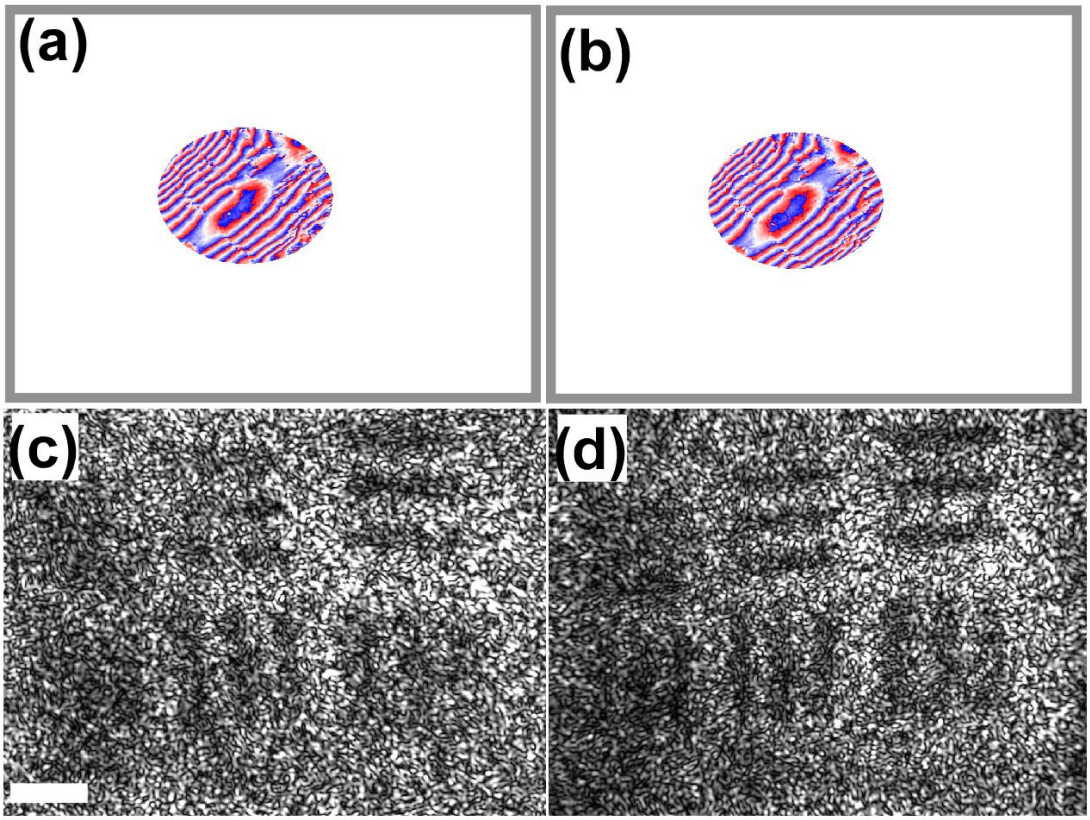

Figure 4.9. Experimental demonstration of the effect of Φ_q on the corrected image. (a): Measured aberration at the pupil when Φ_q is not eliminated. (b): Measured aberration at the pupil when Φ_q is partially eliminated. (c): Image corrected by a). (d): Image corrected by (b).

For the third experimental sample, d_2 is 150mm and d_3 250mm. This is a general case where both Φ_q and Φ_d exist. The results are shown in Fig. 4.10. Figure 4.10(a) shows the distorted field at the CCD plane that is defocused and distorted. Note that the quadratic phase term Φ_q has been eliminated. The focused but distorted image is shown in Fig. 4.10(b). The distorted full field at the pupil is given by Fig. 4.10(c). The amplitude PSF of this system is illustrated by Fig. 4.10(d). Its FT is shown in Fig. 4.10(e). Subtracting Fig. 4.10(e) from Fig. 4.10(c) and taking IFT, we can get the corrected image that is shown in Fig. 4.10(f). The resolution is completely recovered and the defocus is eliminated.

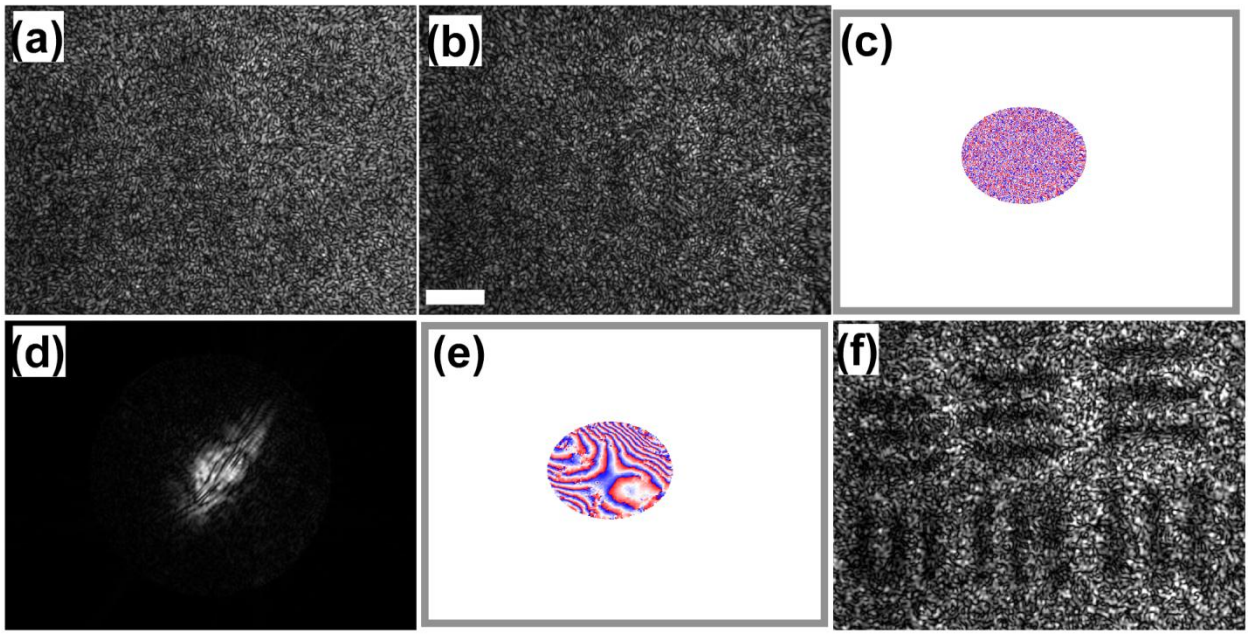

Figure 4.10. Experimental example where both Φ_q and Φ_d exist. (a): Distorted optical field at CCD plane. (b): Distorted image. (c): Distorted field at the pupil. (d): Amplitude PSF of the system. (e): Phase map of the FT of (d). (f): Corrected image.

4.5 Conclusions

In summary, a novel correction method is proposed for the DHAO system. It is realized through the correlation between the complex full-field hologram and complex guide star hologram. By this method, both the aberration at the pupil and the defocus of the system can be removed, which means it is not necessary to further propagate the corrected full field to the image plane, wherever the CCD is. It is worth noting that if the global phase term Φ_q does exist, it has to be removed before the correlation operation. Otherwise, the aberrations can not be correctly compensated for. Although our derivation is based on a two-lens system, the conclusion can be generalized to any optical system, if the optical aberrations of the system mainly lie at or close to the pupil plane. It generalizes the FTDHAO into arbitrary DHAO systems and provides us a guidance to design new experimental schemes for applications in adaptive optics in ophthalmology and microscopy. The measurement error of the phase

aberration is due mainly to the deviation of the guide star spot from the ideal point source. The size of the incident beam at the pupil in the first passage for the guide star hologram is usually set to be about 2 mm in diameter to minimize the effect of the aberration and generate a sharp guide star. From simulations and experiments, this error does exist but is not severe. Also, coherent noise seems inevitable if laser is used as the light source. This may be addressed by use of low coherent light source [3-8].

4.6 References

1. C. Liu, and M. K. Kim, "Digital holographic adaptive optics for ocular imaging: proof of principle," Opt. Lett. **36**, 2710-2712(2011).

2. C. Liu, X. Yu, and M. K. Kim, "Fourier transform digital holographic adaptive optics imaging system," Appl. Opt. **51**, 8449-8454(2012).

3. F. Dubois, L. Joannes, and J. C. Legros, "Improved three-dimensional imaging with digital holography microscope with a source of partial spatial coherence," Appl. Opt. **38**, 7085-7094(1999).

4. G. Pedrini, and H. J. Tiziani, "Short-coherence digital microscopy by use of lensless holographic imaging system," Appl. Opt. **41**, 4489-4496(2002).

5. M. K. Kim, "Adaptive Optics by Incoherent Digital Holography," Opt. Lett. **37**, 2694-2696(2012).

6. M. K. Kim, "Incoherent Digital Holographic Adaptive Optics," Appl. Opt. **52**, A117-A130(2013).

7. F. Dubois, and C. Yourassowsky, "Full off-axis red-green-blue digital holographic microscope with LED illumination," Opt. Lett. **37**, 2190-2192(2012).

8. R. Kelner, and J. Rosen, "Spatially incoherent single channel digital Fourier holography," Opt. Lett. **37**, 3723-3725(2012).

9. U. Schnars and W. Jüptner, "Direct recording of holograms by a CCD target and numerical Reconstruction," Appl. Opt. **33**, 179-181(1994).

10. E. Cuche, P. Marquet, and C. Depeursinge, "Digital holography for quantitative phase-contrast imaging," Opt. Lett. **24**, 291-293(1999).

11. C. Liu, D. Wang, and Y. Zhang, "Comparison and verification of numerical reconstruction methods in digital holography," Opt. Eng. **48**, 1058021-1058027(2009).

12. M. K. Kim, "Principles and techniques of digital holographic microscopy," SPIE Reviews **1**, 1-50(2010).

13. M. K. Kim, *Digital holographic microscopy: principles, techniques, and applications*, Springer Series in Optical Sciences, 55-93(2011).

14. J. Goodman, *Introduction to Fourier Optics*, 3rd ed. Roberts&Company Publishers, 105-107(2005).

15. L. Onural, "Some mathematical properties of the uniformly sampled quadratic phase function and associated issues in digital fresnel diffraction simulation," Opt. Eng. **43**, 2557-2563(2004).

16. N. Pavillon, C. S. Seelamantula, J. Kühn, M. Unser, and C. Depeursinge, "Suppression of the zero-order term in off-axis digital holography through nonlinear filtering," Appl. Opt. **48**, H186-H195(2009).

Chapter Five:

Digital Holographic Line-Scanning Confocal Imaging System

5.1 Introduction

Point-scanning confocal microscopy was originated by M. Minsky in 1961 to obtain high-resolution intensity images and optical sectioning of the samples [1]. It has proven to be successful for noninvasive imaging of thin sections within thick biological samples with high resolution and contrast [2-3]. It has also been widely applied in industrial inspection [4-5]. However, the speed of the image acquisition is limited by the point-scanning configuration. To speed up image acquisition and simplify the optical system, line-scanning confocal systems have been proposed and tested in industrial inspection, imaging of human tissues, and ophthalmology [6-9]. Equipped with adaptive optics, the line-scanning confocal ophthalmoscope is able to image the human retina at the cellular level [10]. Instead of scanning one point in the object at a time, one line is scanned at a time. This scanning scheme with a linear charge-coupled device (CCD) has gained more and more attention because it is fundamentally simpler and faster compared to the point-scanning confocal system. More importantly, the lateral and axial resolutions of the biological images are comparable with the point-scanning system [7-10]. Similar to the point-scanning confocal system, the line-scanning confocal system is unable to get the quantitative phase information of the optical field that is of great interest in industrial inspection and biomedical imaging.

On the other hand, DH is able to get access to the complex amplitude of the optical field

from which quantitative phase information can be retrieved [11-12]. This feature finds DH wide applications in many fields such as industrial inspection, biological imaging, adaptive optics and so forth [13-15]. In most cases, a coherent light source is necessary to perform the DH experiment. Inherent in this coherent imaging modality, speckle noise is still an issue that has severely limited the application of DH in imaging scattering samples such as human tissues. Another limitation of the DH is its lack of optical sectioning capability.

The first effort of combining the confocality with off-axis DH was made in 2012 [16], and confocal phase maps of biological cells were reported in a follow-up paper in 2013 by the same group [17]. In these original proposals, a point-scanning system was adopted. For each point of the sample, a hologram is recorded and numerically processed. The amount of data involved to reconstruct a full-field image is at the level of Terabytes. This huge data flow will make this original scheme hard to find practical applications in industrial testing and biomedical imaging in the near future. To simplify the optical system and speed up the data acquisition and processing, we explored the possibility of combining a line-canning confocal configuration with off-axis DH. The presented digital holographic line-scanning confocal imaging system (DHLCI) can take high-quality intensity images of optical sections and provide quantitative phase map at each optical section at a speed that is at least three orders of magnitude faster than the original digital point-scanning confocal system. The data involved can be easily handled by a regular desktop computer. In our experimental setup, the CCD is put at the image plane of the sample instead of Fourier plane as adopted by the original digital confocal microscope. The whole optical field of the sample is reconstructed without a need of performing numerical propagation. Also, a stronger signal is collected with the CCD at the image plane for imaging weakly scattering object. Since each line scan records all the information of one slice of the object

including the aberrations of the system, it opens the avenues for a variety of numerical aberration compensation methods and development of a full digital adaptive optics system for biomedical imaging especially ophthalmic imaging [14-15, 18-19].This idea will be explored in the next chapter.

This chapter is organized as follows: The optical system of DHLCI is described in section 5.2. In section 5.3, the experimental results are presented and discussed. Finally, the conclusions are drawn.

5.2 Optical Systems

The schematic diagram of DHLCI system is illustrated by Fig. 5.1. Figure 5.1(a) shows the top view of the optical setup. He-Ne laser is the light source with a wavelength of 632.8nm. The laser beam collimated by the beam expander BE1 is sent to a cylindrical lens CL with a focal length of 75mm and forms a diffraction-limited focal line at the back focal plane of the microscope objective MO (NA 0.65, 40×). This illumination configuration is unfolded in Figs. 5.1(b) and 5.1(c). The coordinates of the optical system are shown to the right of Fig. 5.1(b). Figure 5.1(b) shows the illumination in the xz plane where the light is focused at the back focal plane of the CL and front focal plane of the MO and a collimated line is generated on the sample S in the x direction (horizontally). The illumination in the yz plane is shown in Fig. 5.1(a), where the light is focused at the back focal plane of the MO. As a result, a focal line is formed in the x direction at the sample. The CCD with 1024×768 square pixels of a side length 4.65μm is put at the conjugate plane of the sample S. In the experiment, an area of interest with 512×512 pixels is used to speed up the data acquisition and processing. The calibrated magnification between the CCD and object planes is 43.5.

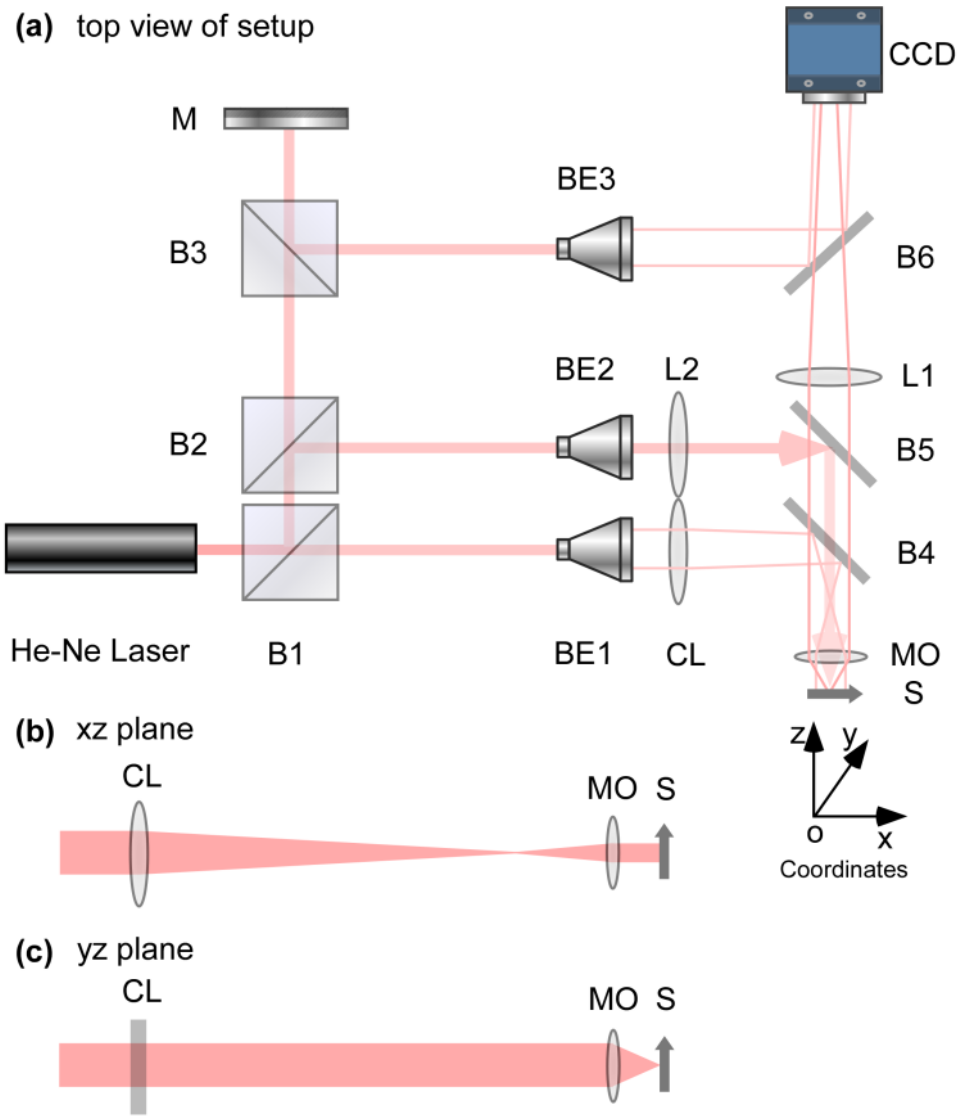

Figure 5.1. Schematic diagram of the optical system. (a) Top view of the setup. B1-B3: Cubic beam splitters, B4-B6: Pellicles. BE1-BE3: Beam expanders. L1-L2: Spherical lens. MO: Microscope objective. CL: Cylindrical lens. M: Mirror. (b) View of the xz plane of the illumination. (c) View of the yz plane of the illumination.

The sample S is mounted on a motorized translation stage. The CCD is triggered by a data acquisition device (Labjack, U3-LV) at the rate of 20 frames/s. The sample is continuously moved in the y direction (vertically) at the speed of 2.14μm/s during the image acquisition so that the pixel resolutions in both the scanning and non-scanning directions are consistent and also satisfy the Nyquist sampling requirement. To generate an off-axis hologram for each line scan, a laser beam collimated by the beam expander BE3 is introduced and reaches the CCD at a small

angle with respect to the light from the sample [11-13]. The exposure time for each hologram is set to be ~0.5ms to remove the motion blurring. To facilitate the adjustment of the sample position and compare the result of DHLCI with that of DH, we introduce a third laser beam indicated by the arrowed lines through the beam expander BE2 and the regular lens L2 in Fig. 5.1(a) to obtain wide-field microscopic images and holograms.

To build up a full-field image at one optical section, a video of 512 holograms is recorded and processed by Matlab 2008b on a Dell desktop computer [Intel(R) Core(TM Duo CPU, 4 Gigabytes memory)] to reconstruct the intensity and phase images. It takes ~26 seconds to complete the data acquisition and ~ 2 minutes to reconstruct the intensity and phase images of an optical section with 512×512 pixels. It is worth noting that no physical slit aperture is added in the optical system. A numerical slit is applied in the numerical reconstruction. The basic process of image reconstruction will be demonstrated in subsection 3.1.

5.3 Experimental Results

5.3.1 Basic Process

To demonstrate the basic process of the confocal image reconstructions, a negative 1951 United States Air Force (USAF) resolution target is used as the sample. The hologram of one scan is shown in Fig. 5.2(a). The detailed view of the region in the white square in Fig. 5.2(a) is shown in Fig. 5.2(b) where the interference fringes are displayed. The angular spectrum of the hologram in Fig. 5.2(a) is shown in Fig. 5.2(c) in logarithmic intensity scale. The region indicated by the white circle is extracted and used to reconstruct this slice of the sample [13]. The resultant intensity $I_n(x,y)$ and phase map $\Phi_n(x,y)$ are shown in Figs. 5.2(d) and 5.2(e)

respectively, where n indicates the nth scan and the phase map is displayed in blue-white-red color map (same for all the phase maps in the remainder of this article).

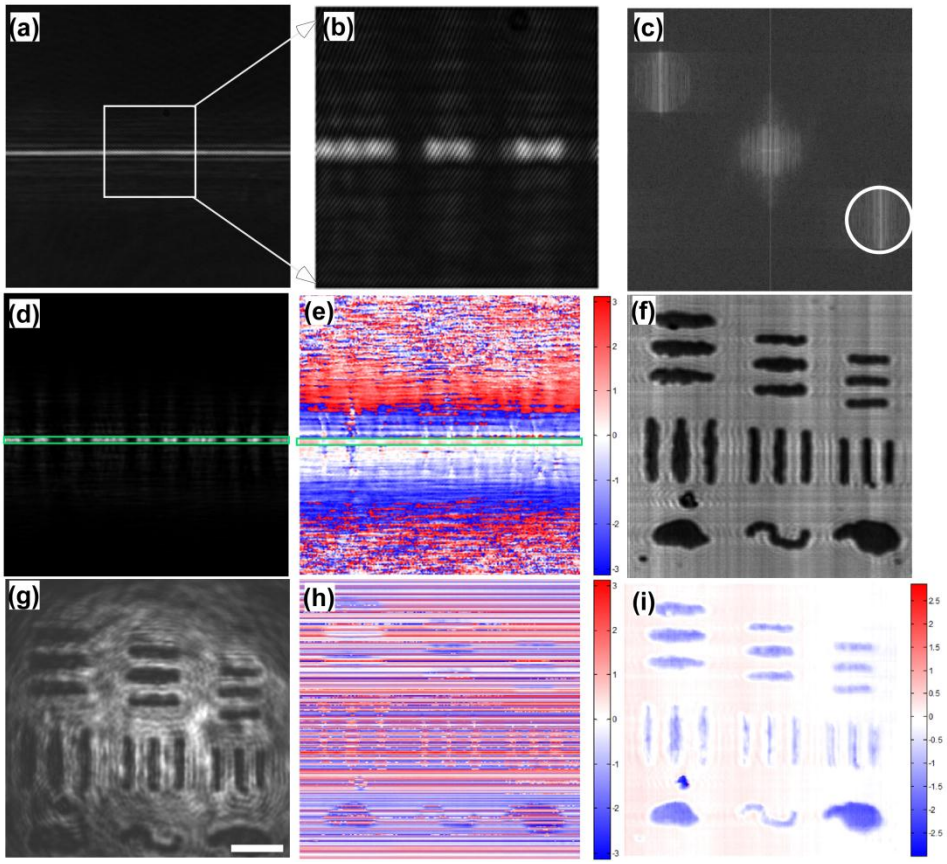

Figure 5.2. Reconstructions of confocal intensity image and confocal phase map. (a) Hologram of one line scan. (b) Detailed view of the region in the white square in (a). (c) Angular spectrum. (d) Reconstructed intensity of the line scan. The green rectangle represents the numerical slit. (e) Reconstructed phase of the line scan. (f) Confocal intensity image. (g) Wide-field image by He-Ne laser illumination. (h) Confocal phase map (in radian). (i) Corrected phase map. Scale bar in (g): 10μm. (f), (g) and (i) have the same field of view.

The confocal intensity I_{conf} (x,n) of this scan is obtained by summing intensity values of I_n(x,y) within a numerical slit along y direction, as follows

$$I_{conf}(x,n) = \sum_{y \in slit} I_n(x,y) \tag{5.1}$$

where the slit means the applied numerical slit indicated by the green rectangle in Fig. 5.2(d). The slit width S_w is determined by one diffraction-limited resolution element, which is given by

$$S_w = \frac{0.61\lambda M}{P \times NA} \tag{5.2}$$

where λ is the wavelength of the light source, M is the magnification of this imaging system, NA is the numerical aperture of the MO and P is the pixel size of the CCD. The result calculated by this equation is 5.55 pixels. We set S_w to be 5 pixels. In fact, the slight change in the slit width bears negligible effect on the reconstructions. The full-field confocal intensity image is obtained by stitching together 512 confocal intensity lines given by Eq. (5.1). The reconstructed full-field intensity image is shown in Fig. 5.2(f). Compared to the wide-field image illustrated in Fig. 5.2(g), the confocal intensity image clearly shows higher contrast and lower coherent artifact.

The confocal phase profile $\Phi_{conf}(x,n)$ of each scan is obtained by taking average of the phase values of $\Phi_n(x,y)$ within the numerical slit along y direction, as follows

$$\Phi_{conf}(x,n) = \frac{\sum_{y \in slit} \Phi_n(x,y)}{S_w} \tag{5.3}$$

The reconstructed full-field confocal phase map is shown in Fig. 5.2(h). Random phase shifts among different line holograms due to the mechanical vibrations prevent a two-dimensional phase map from being visualized. These phase shifts can be removed by the following numerical procedures: Step 1, Subtracting the phase values in the nth row from those in the (n-1)th row in a pixel-wise way; Step 2, Picking the value with maximum likelihood as the phase shift and correcting the nth row by subtracting this phase shift from it and wrapping the result into the range (-π π]; Step 3, Increasing n by one and repeating steps 1 and 2 until last row. Note that in the first step the (n-1)th row has already been corrected. The corrected phase map is shown in Fig. 5.2(i). This procedure is based on the observations that the neighboring line phase profiles have similar shapes and that phase shifts across them are the same.

5.3.2 System Resolution Measurements

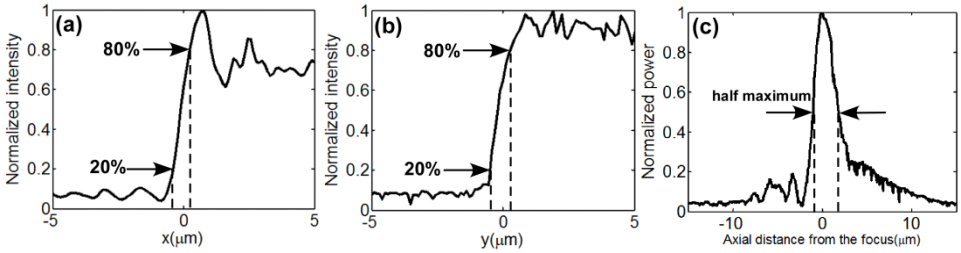

Figure 5.3. Measurements of lateral and axial resolutions. (a) Edge spread function in x direction. (b) Edge spread function in y direction. (c) Axial response with respect to the axial distance away from the focal plane.

The edge spread functions (ESF) can be used to test the lateral resolutions of intensity images [5]. The standard way is imaging a sharp edge object. In our experiment, an edge from a Ronchi ruling (20lp/mm) is imaged. Figure 5.3(a) shows the ESF in the non-scanning direction (x direction). The 20%-80% width as indicated by the distance of the two vertical dashed lines in Fig. 5.3(a) is used to estimate the lateral resolution in this direction that is ~0.64μm. The ESF in the scanning direction (y direction) is shown in Fig. 5.3(b). This curve shows a smoother boundary at the edge than the ESF in the non-scanning direction because of the confocality. The 20%-80% width as measured by the distance of the two vertical dashed lines in Fig. 5.3(b) is also ~0.64μm. These estimates of the lateral resolutions are close to the diffraction-limited resolution that is 0.59μm and can be verified by the confocal intensity image shown in Fig. 5.2(f) where the width of the smallest bar is 2.14μm. 0.64μm is a quite close estimate of the actual resolution. The lateral resolutions of the phase images are close to those of the intensity images as evidenced by the phase map in Fig. 5.2(i). The axial resolution of intensity images can be tested by measuring the power within the numerical slit of the images of a mirror while it is moved through the focal plane [20]. The axial response with respect to the axial distance away from the focal plane is given by Fig. 5.3(c). The axial resolution can be estimated by the full width at half maximum (FWHM) of this curve that is ~2.70μm, as indicated by the distance of the two vertical

dashed lines in Fig. 5.3(c). The accuracy of phase map at each optical section will be discussed in subsection 3.3.

5.3.3 Confocal Phase Map

A phase object is made by depositing a layer of chrome on top of a positive 1951 USAF resolution target to remove the amplitude contrast. The height of the bars on the target is around 100nm that is well within one axial resolution element [21]. Thus, both the top and bottom planes are in focus. The phase map obtained by DHLCI is shown in Fig. 5.4(a). The height profile at the cross section indicated by the solid line in Fig. 5.4(a) is shown in Fig. 5.4(b). The relationship between the height and the phase is given by

$$Height = \frac{Phase}{4\pi}\lambda \tag{5.4}$$

where λ is the wavelength of the laser. The denominator is 4π instead of 2π because the imaging system is in reflection mode. The height of this cross section is calculated as 100.8nm. The noise level can be visualized by the height profile of a cross section through an empty region, as shown in Fig. 5.4(c) that is the height profile of the cross section indicated by the dashed line in Fig. 5.4(a). The noise level is measured by evaluating the standard deviation of a flat region indicated by the dashed square in Fig. 5.4(a) that is calculated as 2.4nm. For comparison, DH is performed on the same area of the target. The phase map obtained by DH is shown in Fig. 5.4(d). The height profile at the cross section indicated by the solid line in Fig. 5.4(d) is shown in Fig. 5.4(e). The height of this cross section is calculated as 105.0 nm. Figure 5.4(f) shows the height profile of the cross section indicated by the dashed line in Fig. 5.4(d). Compared to Fig. 5.4(c), it shows stronger height variation, which means the noise level of DH is worse than the DHLCI. By evaluating the standard deviation of a flat region indicated by the dashed square in (d), the

noise level is calculated as 4.8nm. A more intuitive comparison of the noise levels of Figs. 5.4(a) and 5.4(d) can be given by Figs. 5.4(g) and 5.4(h). It is quite obvious that the phase image of Fig. 5.4(h) is smoother than that of Fig. 5.4(g), indicating the noise level of DHLCI is better than DH.

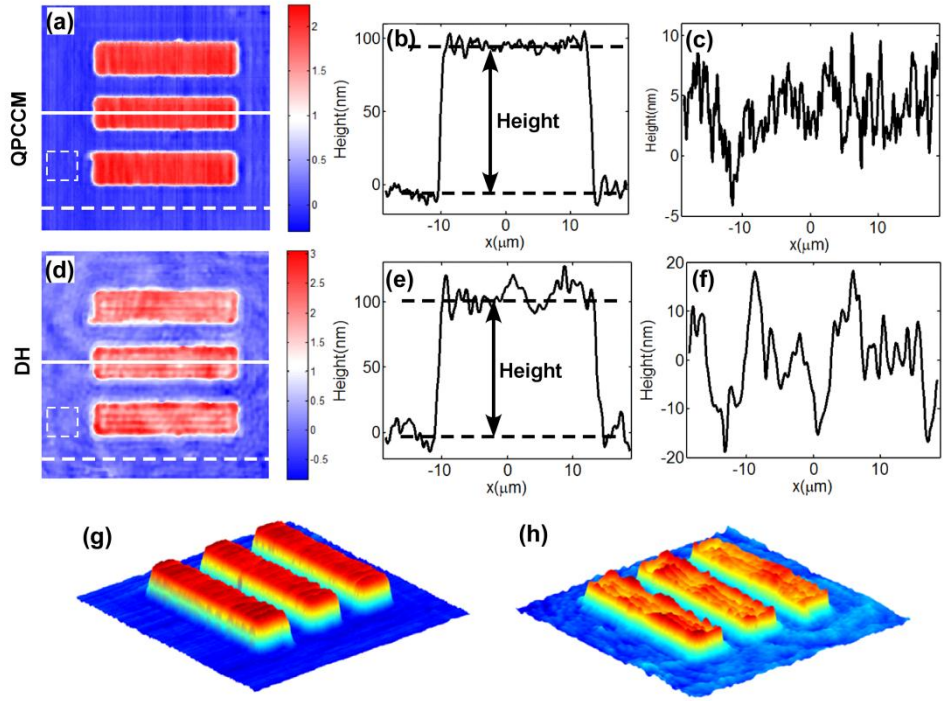

Figure 5.4. Phase images of a phase object by QPCCM and DH. (a) Phase map by QPCCM. (b) Height profile of a cross section by the solid line in (a). (c) Height profile of a cross section by the dashed line in (a). (d) Phase map by DH. (e) Height profile of a cross section indicated by the solid line in (d). (f) Height profile of a cross section indicated by the dashed line in (d). (g) Three-dimensional pseudo-color rendering of (a). (h) Three-dimensional pseudo-color rendering of (d). Fields of view of (a) and (d) are 37.4×37.4μm^2.

The effect of the slit width on the phase profile is investigated by observing how the phase profile of the cross section in Fig. 5.4(b) changes as the slit width. By convention, the unit of slit width adopted here is in Airy Unit (A.U.) that is given by [4]

$$A.U. = \frac{1.22\lambda}{NA} \tag{5.5}$$

One A.U. is the diameter of the first dark ring of the Airy pattern. As illustrated by Fig. 5(a), when the slit width is within several A.U., the phase profiles do not change much. After several A.U., the phase profiles start deviating away from the normal phase profiles and finally lose the

phase information as the slit width becomes too large. This process can be more clearly monitored by the change in the measured height as the slit width, as shown in Fig. 5.5(b). When slit width is within about 2 A.U., the measured height stays almost the same. As the numerical slit increases, the strong phase fluctuations outside the focal line will come into play and finally destroy the phase information when the slit is too large. It can be seen that, after about 2 A.U., the measured height begins decreasing and finally becomes meaningless when slit width becomes too large. This observation indicates that the phase map of DHLCI is not sensitive to the slit width when it is within about 2 A.U..

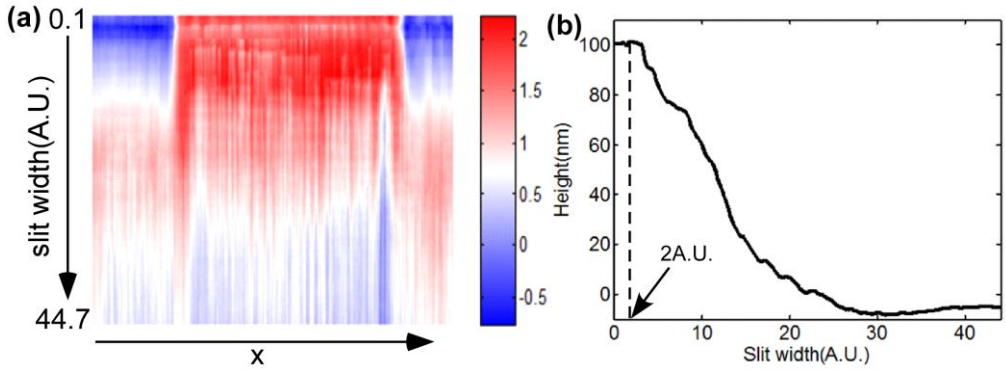

Figure 5.5. The effect of slit width on the phase profile. (a) The phase profile versus the slit width. (b) The measured height versus the slit width.

5.3.4 Optical Sectioning

In subsection 5.3.1, we have demonstrated that the intensity image of DHLCI is better than the wide-field coherent image in terms of the contrast and coherent noise. The experimental results in subsection 5.3.3 indicate that DHLCI can get an even better phase map than DH. Another important characteristic of DHLCI is its capability of optical sectioning. In fact, we have measured its axial resolution that is ~2.70μm in subsection 5.3.2. In this subsection, we will demonstrate this capability by imaging a silicon wafer at different depths. We will also demonstrate that the phase maps at different depths can be obtained. The silicon wafer is made

by photolithography and the average depth of the patterns is about 20.1μm, which is obtained by an optical profiler (Veeco Instruments Inc.) Figures 5.6(a)-5.6(c) show the wide-field laser images at three different axial distances z=0μm, 10μm, and 20μm respectively. It is apparent there is no optical sectioning for wide-field imaging. Figures 5.6(d)-5.6(f) show the confocal intensity images at these three depths by DHLCI. At z=0μm, the top layer of the silicon wafer is focused and other parts of the image become dark. At z=10μm, no apparent plane is focused. When z is set to be 20μm, the bottom layer of the etched lines are focused and other parts of the image become dark. To further demonstrate the optical sectioning, a confocal xz section at the position indicated by the dashed in Fig. 5.6(f) is illustrated by Fig. 5.6(g) where one can discern the bottom and top layers. The depth of the left hole can be measured as the difference in z values that correspond to the maximum intensities of the top and bottom surfaces of the left hole in Fig. 5.6(g), which is ~20.7μm. Similar to the conventional line-scanning confocal microscope, the numerical slit plays a role in enabling the optical sectioning. If the numerical slit is not applied, the capability of optical sectioning will disappear. It is worth noting that removal of the numerical slit means extending the numerical slit to the whole image height. Figures 5.6(h)-5.6(j) are the intensity images at the three depths when the numerical slit is removed. We can not see any characteristics of the optical sectioning. The loss of optical sectioning because of removal of the numerical slit is clearly illustrated by Fig. 5.6(k) that shows the non-confocal counterpart of Fig. 5.6(g). In this image, the layered structure is totally lost.

Different from the conventional line-scanning confocal microscope, DHLCI is able to get the quantitative phase maps of the confocal planes. This characteristic can be illustrated by the confocal phase maps shown in Figs. 5.6(l)-5.6(n). When the top layer of sample is focused, we can measure the height variation of this focused surface as shown in Fig. 5.6 (l). At z=10μm,

there is no apparent focal plane, therefore the corresponding phase map shown in Fig. 5.6(m) is of no practical interest. What is of interest is the phase map at the bottom layer as shown in Fig. 5.6(n), which may reflect irregularity of the etched surfaces. There are two strips in the phase maps that correspond to the bright regions in Fig. 5.6(f). These two pieces of phase maps can provide us with a quantitative way to assess the height variations of the bottom layer.

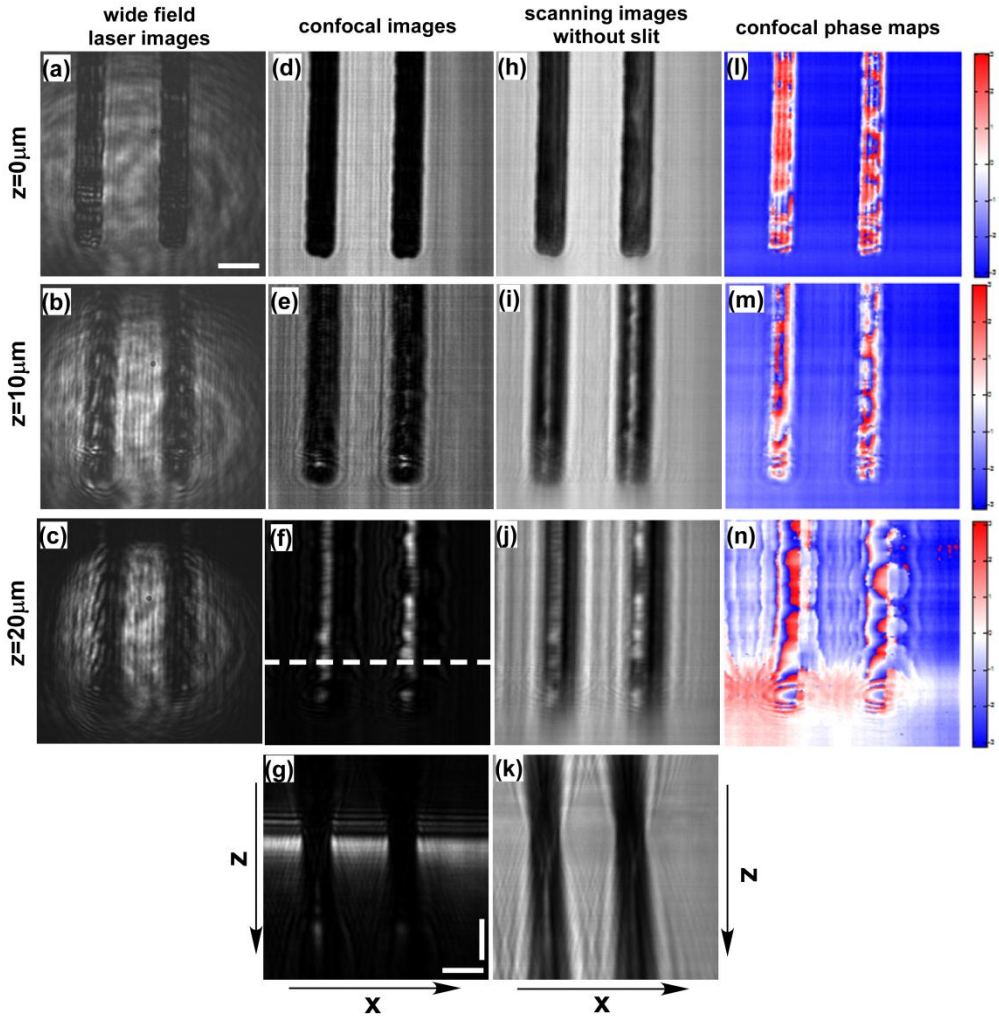

Figure 5.6. Confocal intensity images and phase maps of optical sections of a silicon wafer. (a)-(c) Wide-field images at z=0μm,10μm, and 20μm. (d)-(f) Confocal intensity images at z=0μm,10μm, and 20μm. (g) Confocal xz section at the position in xy plane indicated by the dashed line in (f). (h)-(j) Scanning images without numerical slit at z=0μm,10μm, and 20μm. (k) Non-confocal counterpart of (g). (l)-(n) Confocal phase maps at z=0μm,10μm, and 20μm. Scale bars in (a) and (g): 10μm.

5.4 Conclusions

We have experimentally demonstrated a quantitative phase-contrast confocal microscope that is fundamentally faster and simpler compared to the point-scanning digital confocal system [16-17]. DHLCI can obtain the quantitative phase profiles at an even better noise level than DH. Optical sectioning capability and high-contrast intensity imaging with low coherent noise promise its potential applications in industrial inspection and biomedical imaging. DHLCI also opens the avenues for a variety of numerical compensation methods and development of a full digital adaptive optics system for biomedical imaging especially ophthalmic imaging [14-15, 18-19].

5.5 References

1. M. Minsky, "Microscopy apparatus," U.S. patent 3,013,467(December 1961).
2. R. H. Webb, "Confocal optical microscopy," Rep. Prog.Phys.**59**, 427-471(1996).
3. J. B. Pawley, ed. *Handbook of biological confocal microscopy* (Springer,1995).
4. T. Wilson, ed. *Confocal microscopy* (Academic,1990).
5. T. R. Corle, and G. S. Kino, ed. *Confocal scanning optical microscopy and related imaging systems* (Academic, 1996).
6. K. Im, S. Han, Park,D. Kim, and B. Kim, "Simple high-speed confocal line-scanning microscope," Opt. Express.**13,** 5151-5156(2005).
7. P. J. Dwyer, C. A. DiMarzio, J. M. Zavislan, W. J. Fox, and M. Rajadhyaksha, "Confocal reflectance theta line-scanning microscope for imaging human skin *in vivo*," Opt. Lett. **31,** 942-944 (2006).
8. D. X. Hammer, R. D. Ferguson, T. E. Ustun, C. E. Bigelow, N. V. Iftimia, and R. H. Webb, "Line-scanning laser ophthalmoscope," J. Biomed. Opt. **11**, 041126(2006).
9. P. J. Dwyer, C. A. Dimarzlo, and M. Rajadhyaksha, "Confocal theta line-scanning microscope for imaging human tissues," Appl. Opt. **46**, 1843-1851(2007).

10. M. Mujat, R. D. Ferguson, N. Iftimia, and D. X. Hammer, "Compact adaptive optics ophthalmoscope," Opt. Express **17**, 10242-10258(2009).

11. E. Cuche, P. Marquet, and C. Depeursinge, "Digital holography for quantitative phase-contrast imaging," Opt. Lett. **24**, 291-293 (1999).

12. C. Mann, L. Yu, C. Lo, and M. K. Kim, "High-resolution quantitative phase-contrast microscopy by digital holography," Opt. Express. **13**, 8693-8698 (2005).

13. M. K. Kim, "Principles and techniques of digital holographic microscopy," SPIE Reviews **1**, 1-50(2010).

14. C. Liu, and M. K. Kim, "Digital holographic adaptive optics for ocular imaging: proof of principle," Opt. Lett., **36**, 2710-2712(2011).

15. C. Liu, X. Yu, and M.K. Kim, "Fourier transform digital holographic adaptive optics imaging system," Appl. Opt. **51**, 8449-8454(2012).

16. A. S. Goy, and D. Psaltis, "Digital confocal microscope," Opt. Express **20**, 22720-22727(2012).

17. A. S. Goy, M. Unser, and D. Psaltis, "Multiple contrast metrics from the measurements of a digital confocal microscope," Biomed. Opt. Express **4**,1091-1103(2013).

18. J. Fienup, and J. J. Miller, "Aberration correction by maximizing generalized sharpness metrics," J. Opt. Soc. Am. **A 20**,609-620(2003).

19. S. T. Thurman, and J. Fienup, "phase-error correction in digital holography," J. Opt. Soc. Am. **A 25**, 983-994(2008).

20. T. Wilson, and A. R. Carlini, "Size of the detector in confocal imaging systems," Opt. Lett. **12**, 227-229(1987).

21. A. Khmaladze, M. K. Kim, and C. M. Luo, "Phase imaging of cells by simultaneous dual-wavelength reflection digital holography," Opt. Express **16**, 10900-10911(2008).

Chapter Six:

Digital Adaptive Optics Line-Scanning Confocal Imaging System

6.1 Introduction

Point-scanning confocal microscopy, which was proposed by M. Minsky, has proven to be successful for noninvasive imaging of thin sections within thick biological samples and industrial samples with high resolution and contrast [1-5]. Recently, line-scanning confocal imaging systems has gained more and more attention because it is fundamentally simpler and faster compared to the point-scanning confocal system [6-10]. Instead of scanning one point in the object at a time, one line is scanned at a time. Similar to the point-scanning confocal system, the line-scanning confocal system is unable to get the quantitative phase information of the optical field that is of great interest in industrial inspection and biomedical imaging. These issues can be addressed by applying digital holography (DH) to the confocal imaging system, which is able to get the quantitative phase information of the optical field [11-15].

The first effort of applying DH to the confocal imaging system was made in 2012 [16], and confocal phase maps of biological cells were reported in a follow-up paper in 2013 by the same group [17]. In these original proposals, a point-scanning system was adopted. For each point of the sample, a hologram is recorded and numerically processed. The amount of data involved to reconstruct a full-field image is at the level of Terabytes. This huge data flow will make this original scheme hard to find practical applications in industrial testing and biomedical imaging in the near future. To simplify the optical system and speed up the data acquisition and

processing, we explored the possibility of combining a line-scanning confocal configuration with off-axis DH [18]. We have described this digital line-scanning confocal imaging system in Chapter 5. In this chapter, we will present a digital adaptive optics line-scanning confocal imaging system (DAOLCI). The idea of DAOLCI is to explore the possibility of correcting for aberration of the each slice of the sample that is distorted by the aberration at the pupil plane by use of digital holographic adaptive optics (DHAO). In the DAOLCI, digital line-scanning configuration is equipped with Fourier Transform DHAO as described in chapter 3. Specifically, the CCD is put at Fourier domain of the eye pupil and image plane of the sample. The configuration for digital line-scanning imaging is the same as presented in chapter 5 and the ref. [18]. What is different is that we will add an additional beam to sense the aberration at eye pupil as presented in Chapter 3 and ref. [15]. Because of the aberration, each line hologram will be distorted and final full-field confocal image will be degraded. To remove this distortion, we record the aberration through a guide star hologram. Each distorted line hologram is corrected by this guide star hologram, and then all the corrected line reconstructed intensity are combined to yield the final corrected image.

6.2 Principle and Optical System

Digital adaptive optics line-scanning confocal imaging system (DAOLCI) adopts the idea of Fourier Transformation DHAO system (FTDHAO). That means we can treat each line hologram as the full-field distorted hologram in FTDHAO system where the CCD is put at the Fourier domain of the eye pupil and image plane of the sample. The designed optical system is illustrated in Fig. 6.1.

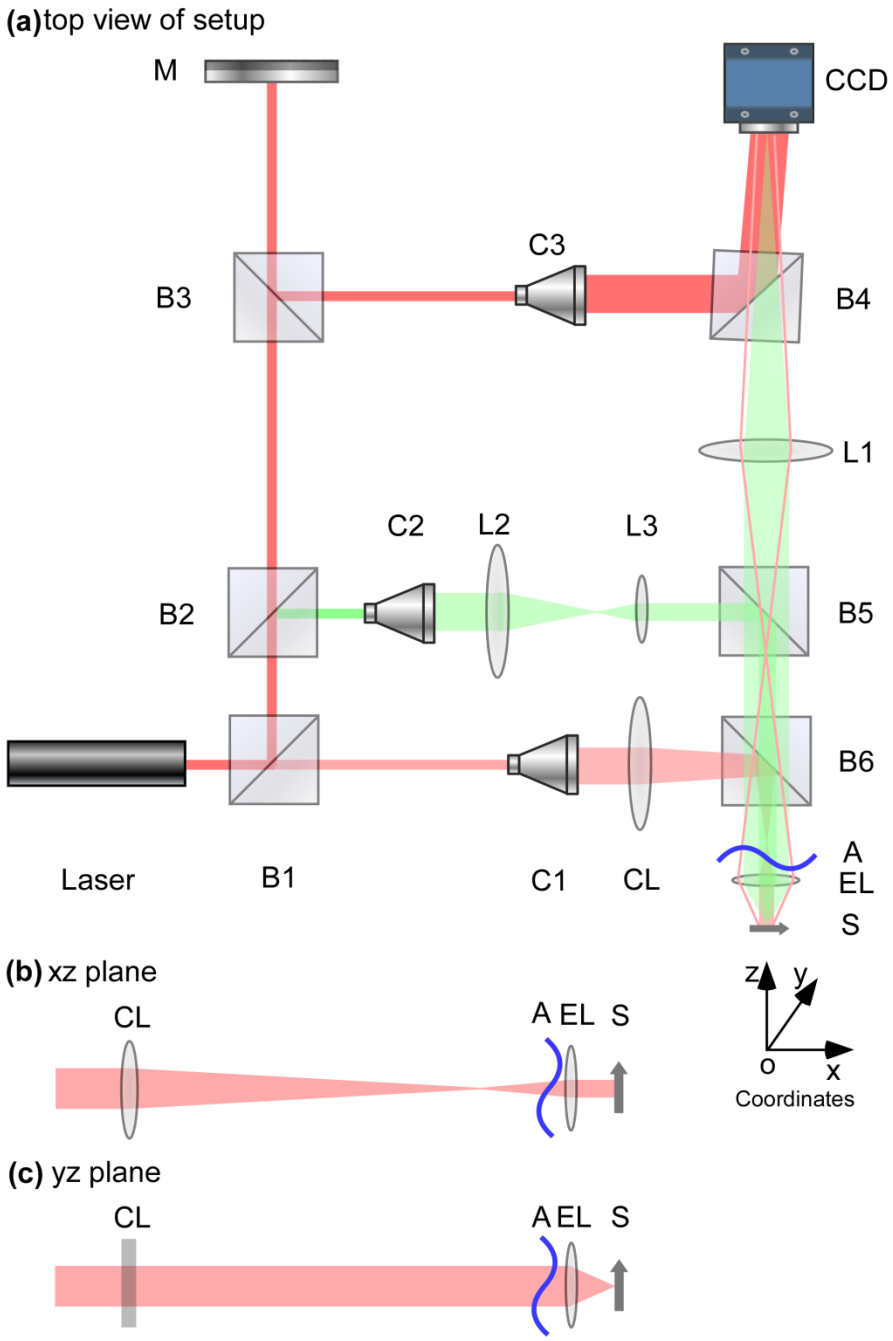

Figure 6.1. Optical system for digital adaptive optics line-scanning confocal imaging system. B1-B6: Beamsplitters, C1-C3: Collimators, M: Mirror, CL: Cylindrical lens (focal length 150mm). EL: eye lens (focal length 25mm). A:Aberrator. L1-L3: Lens.

Figure 1(a) shows the layout of the designed optical system. A model eye composed of a regular lens (EL, focal length 25mm) and an artificial aberrator (A) at the pupil plane will be used in the experiments. L1(focal length 200mm) realizes the Fourier transformation between the

optical fields at the CCD plane and the eye pupil as we detailed in chapter 3 and ref.[15]. Specifically L1 is put 200mm away from the eye pupil and the CCD is placed 200mm away from L1. Similar to the FTDHAO, DAOLCI includes three basic steps. In the first step, a narrow beam is sent into the eye lens to generate a guide star at the retina plane. The narrow beam is realized by an inverted telescope system L2(100mm) and L3(30mm). CCD takes this guide star hologram and reconstruct the aberration at the eye pupil. In the second step, the distorted line holograms are recorded. Without aberration compensation, this reconstructed lines of the object field will be blurred and the final full-field confocal image will be degrade. Lastly, each line hologram will be compensated for by the same aberration obtained from the guide star hologram, and the resultant confocal image will be improved. Different from FTDHAO, DAOLCI is a line-scanning confocal system. At a time, one line is projected on the sample and one slice of the object can be reconstructed. To get the confocal full-field image, the sample is scanned along horizontal or vertical directions. The details of the illumination are illustrated in the Fig. 6.1(b) and 6.1(c). In this system, a horizontal line will be projected on the sample. The direction of the projected line can be easily adjusted by rotating the cylindrical lens CL.

6.3 Simulations

To verify this idea, computer simulations are carried out. In the computer simulations, radiation wavelength is set to 632.8nm. We set the beam size on the cylindrical lens as 3mm in diameter to avoid the aberration in the first passage. The scanning step is set to be 3μm. The eye focal length of the lens EL is 25mm with a size of 5mm in diameter. Focal length of cylindrical lens CL is 150mm. The imaging numerical aperture (NA) is 0.1, the corresponding diffraction limited element is 3.9μm. The illumination on the sample is shown in the Fig. 6.2(a). If the

object is a perfect mirror, the image of this line is shown in Fig. 6.2(b). The profile along middle line in the Fig. 6.2(b) is shown in Fig. 6.2(c) which is a diffraction-limited line with a full width at half maximum (FWHM) 4.5μm which is a little larger than 3.9 μm due to the lower illumination N.A. which is 0.06. The profile along middle line in y direction is shown in Fig. 6.2(d). The FWHM of this curve is 428 μm which will become the height of final confocal image. The width of the final confocal image will be the number of scan times the scanning step. In our experiment, the number of scan is 256. That means the width of the final image is 768μm.

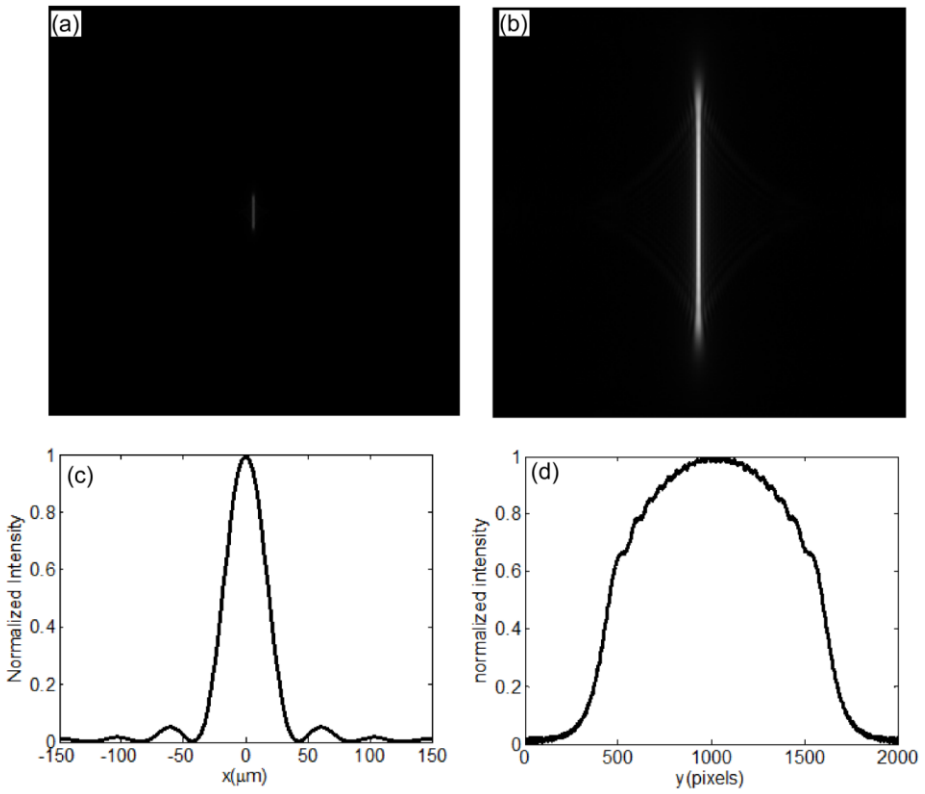

Figure 6.2. Illumination in DAOLSI. (a) Illumination on the sample. (b) Image of the one slice of a perfect mirror. (c) The x profile along middle line in (b). (d) The y profile along the middle line in (b).

The amplitude of the sample we used is part of digital resolution target and phase of the sample is an array of random phase ranging from –pi to +pi. Figures 6.3(a) and 6.3(b) show the amplitude and phase of this sample respectively. In the simulation, only one patch of the sample

bounded by the green rectangles will be scanned. The magnified view the amplitude and phase within the green rectangles in Figs. 6.3(a) and 6.3(b) are shown in Figs. 6.3(c) and 6.3(d) respectively.

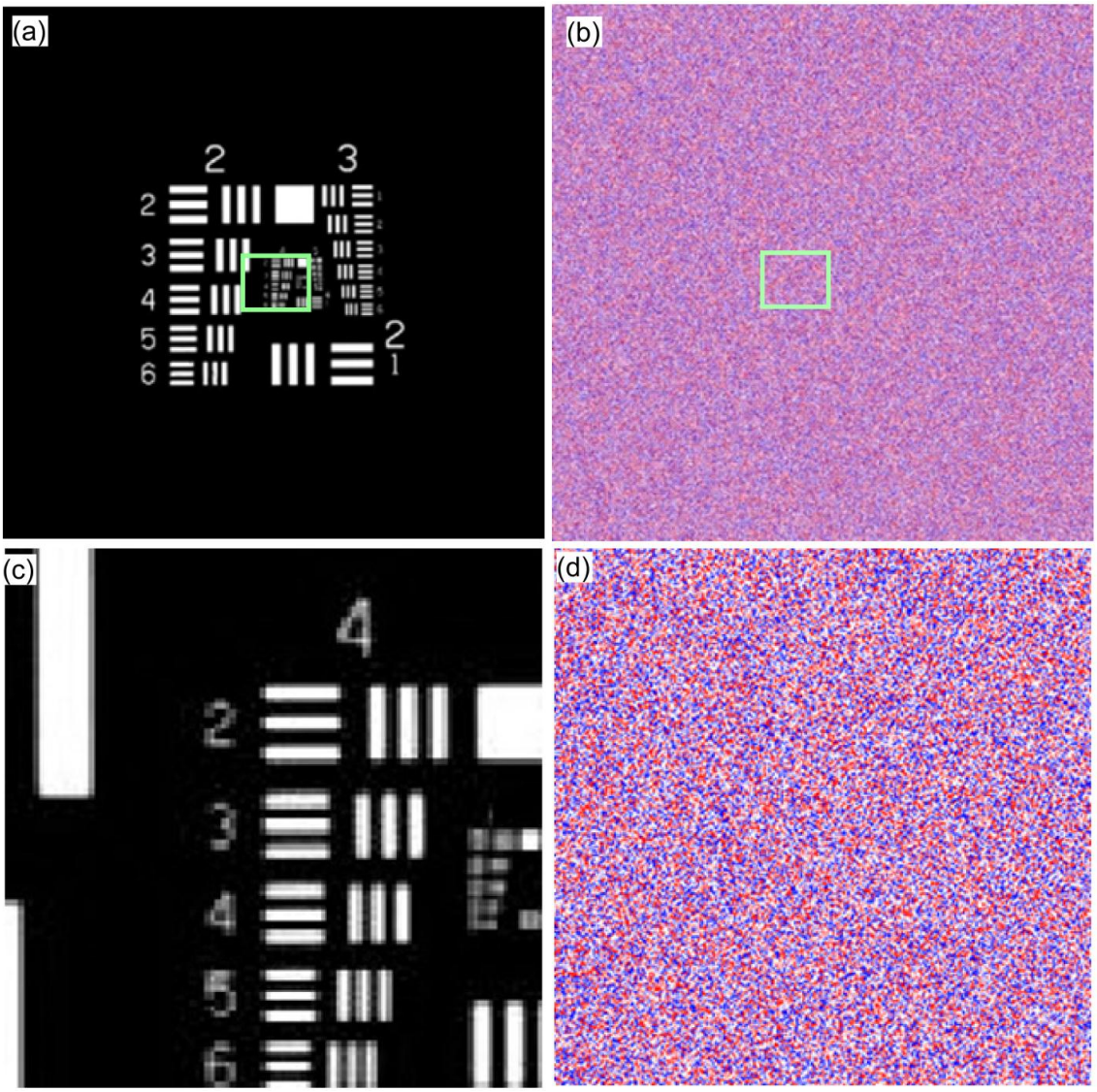

Figure 6.3. Simulated retina. (a) Amplitude of the simulated retina. (b) Phase of the simulated retina. (c) The region in (a) that is scanned by DAOLCI. (d) The region in (b) that is scanned by DAOLCI.

The adaptive optics process on this sample is illustrated in Fig. 6.4. As a baseline, one single line image at the CCD plane and the corresponding confocal image are shown in Figs. 6.4(a) and 6.4(b). The width of the numerical slit is set to be 9 pixels, which corresponds to less than one diffraction-limited element. The simulated aberration as shown in Fig. 6.4(c) is put at

the pupil plane of the lens EL. This aberration is given by $\Phi = 8\pi(3r^3 - 2r)\sin(\theta)$, where (r, θ) is the normalized polar coordinate at the pupil plane. In the simulation, the diameter of the pupil is set to be 5mm. With this aberration, the distorted line image is shown in Fig. 6.4(d). The corresponding confocal image is shown in Fig. 6.4(e) which is degraded by the aberration. Since the line image is spread, the confocal image is the best one by visual observation while moving the center of the numerical slit across the spread line image with a fixed width. To recover the Images, we perform aberration sensing using a guide star hologram. Figure 6.4(f) shows the measured wave aberration from the guide star hologram. After removing this aberration numerically, the single line image is recovered as shown in Fig. 6.4(g). The corrected confocal image is shown in Fig. 6.4(h), the resolution and contrast of which are recovered. This example clearly demonstrates the effectiveness of the DHAO.

A second example is digital image of a pelican. The simulation results of DAOLCI are shown in Fig. 6.5. As a baseline, one single line image at the CCD plane and the corresponding confocal image are shown in Figs. 6.5(a) and 6.5(b). The width of the numerical slit is set to be 9 pixels, which corresponds to less than one diffraction-limited element. The simulated aberration as shown in Fig. 6.5(c) is put at the pupil plane of the eye lens. This aberration is generated by $\Phi = 16\pi(4r^4 - 2r^2)\sin(2\theta)$. In the simulation, the diameter of the pupil is also set to be 5mm. With this aberration, the distorted line image is shown in Fig. 6.5(d). The corresponding confocal image is shown in Fig. 6.5(e) which is degraded by the aberration. Since the line image is spread, the confocal image is the best one by visual observation while moving the center of the numerical slit across the spread line image with a fixed width. To recover the Images, we the perform aberration sensing using a guide star hologram. Figure 6.5(f) shows the measured wave aberration from the guide star hologram. After removing this aberration numerically, the single

line image is recovered as shown in Fig. 6.5(g). The corrected confocal image is shown in Fig. 6.5(h), the resolution and contrast of which are recovered. This example further demonstrates the effectiveness of the DHAO.

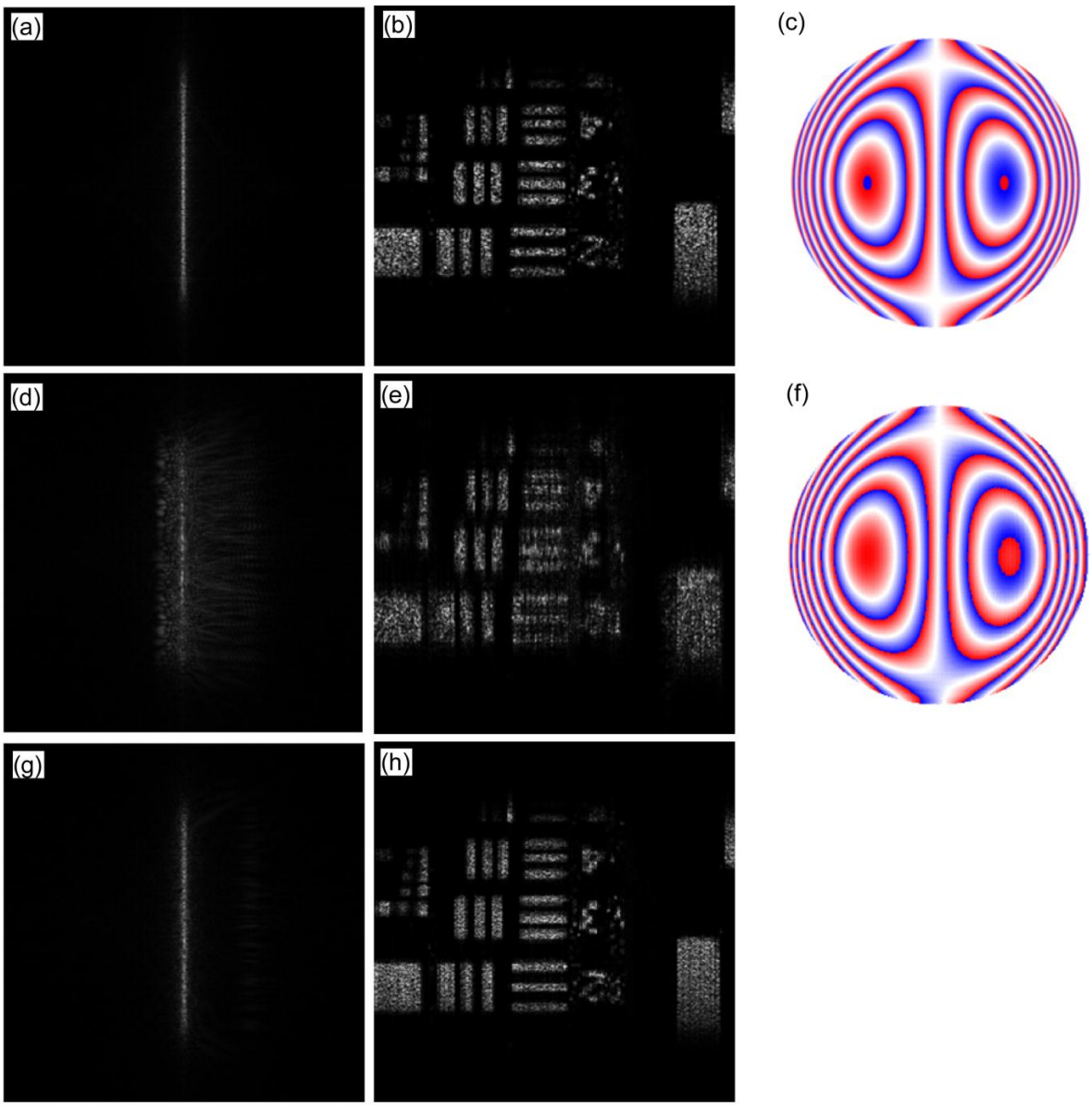

Figure 6.4. Results from the simulations on resolution target. (a) One single line image without aberration. (b) Confocal image without aberration as a baseline. (c) Added aberration at the pupil plane. (d) Distorted line image. (e) Degraded confocal image. (g) Recovered line image by DHAO. (h) Recovered confocal image.

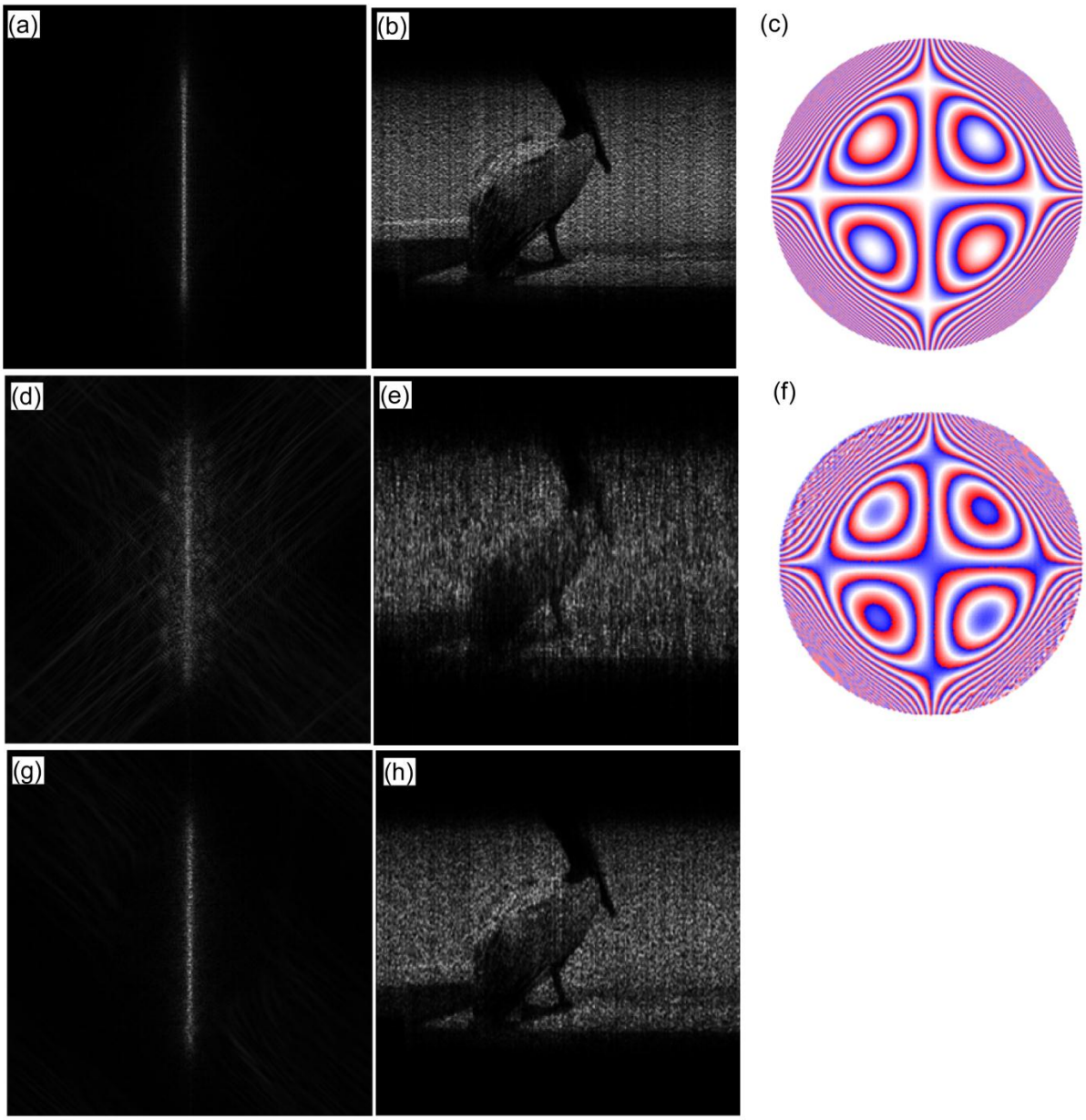

Figure 6.5. Results from the simulation on digital image of pelican. (a) One single line image without aberration. (b) Confocal image without aberration as a baseline. (c) Added aberration at the pupil plane. (d) Distorted line image. (e) Degraded confocal image. (g) Recovered line image by FTDHAO. (h) Recovered confocal image.

6.4 Experimental Results and Discussions

In this section, experimental results are presented and discussed. A He-Ne laser with a wavelength 632.8nm is used as the light source. A CCD with 1024×768 square pixels with a pitch 4.65um is used, of which 512×512 pixels are employed as active detection region. The

scanning speed is set to be 10.8μm/s so that the pixel resolutions along scanning and non-scanning directions are both 0.54um. The field of view (FOV) of retinal images are 276×276μm^2. The beam size illuminating the cylindrical lens CL is set to be ~2mm in diameter. To verify that the effect of aberration on the illumination is negligible under a narrow beam, we put a second CCD at the focal plane of the eye lens. Line focuses are shown in Fig. 6.6. Figure 6.6(a) shows the line illumination without aberration. The line illumination with aberration is shown in Fig. 6.6(b), which is slightly slanted by the aberration. This slight slanting can be easily compensated by rotating the CL. The line illumination after pre-correction is shown in Fig. 6.6(c). To quantify this process, the profiles along vertical directions of Figs. 6.6(a)-6.6(c) are given in Figs. 6.6(d)-6.6(f). FWHMs of these curves are all 9.4μm. That means the aberration does not affect the line width of the illumination. The effect of this small change in orientation is negligible in this experiment, because a slightly wide numerical slit will eliminate this effect.

In this experiment, a scattering sample is made by closely attaching a piece of Teflon tape behind a positive 1951 resolution target and tilted to remove the specular reflections from the surfaces of the resolution target. A piece of broken glass is put at the pupil plane, serving as the aberrator. Group 4 elements 4-5 are imaged. Figure 6.7(a) shows the hologram of one slice of the sample without the aberrator in place. Figure 6.7(b) shows the phase distribution at the pupil plane which is obtained by taking inverse FT of the hologram Fig. 6.7(a). The distorted line hologram due to the aberrator is shown in Fig. 6.7(c). The corresponding distorted phase at the pupil is shown in Fig. 6.7(d). To measure the aberration, a narrow beam of a size ~2mm in diameter sent through the lens EL, as shown by the green beam in Fig. 6.1. The resulting guide star hologram is shown in Fig. 6.7(e). The phase aberration obtained from this guide star

hologram is shown in Fig. 6.7(f). Figure 6.7(g) shows the corrected phase distribution at the pupil by subtracting Fig. 6.7(f) from Fig. 6.7(d) on a complex amplitude basis.

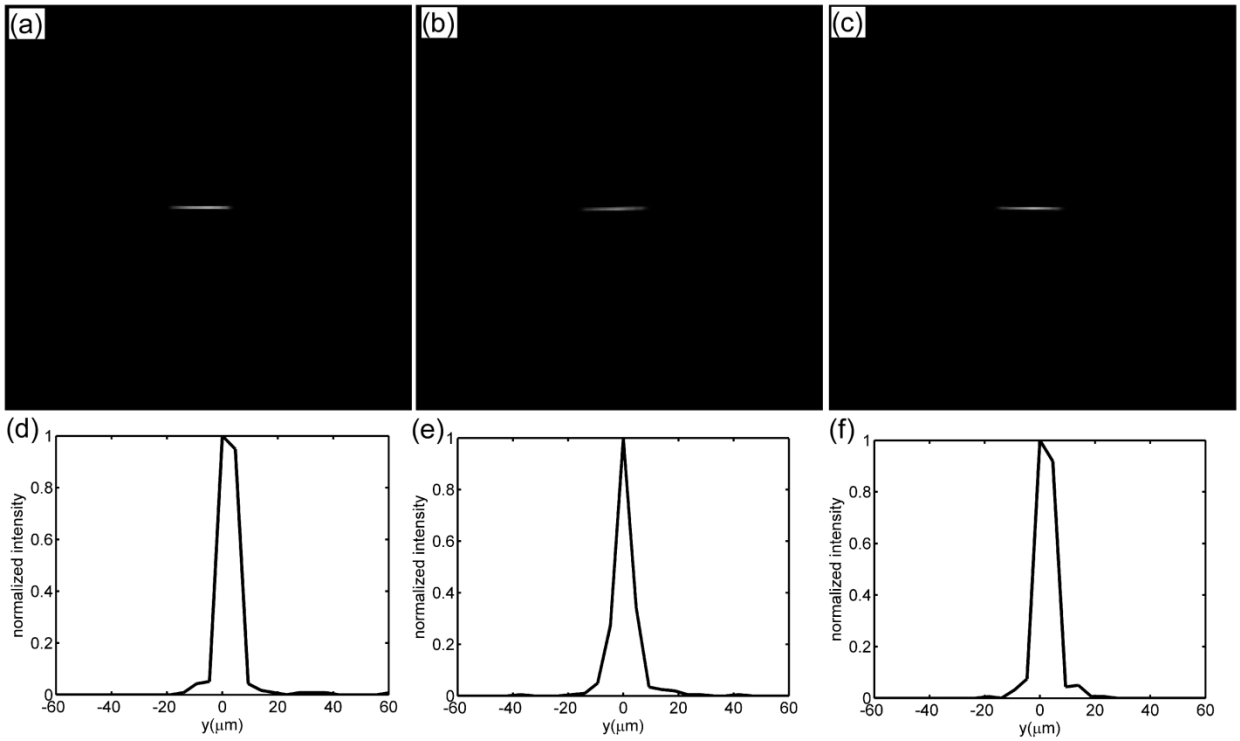

Figure 6.6. Line illuminations without aberration, with aberration and with pre-compensation.

The resultant confocal images are shown in Fig. 6.8. Figure 6.8(a) shows one line intensity without distortion as a baseline. Figure 6.8(b) shows the confocal image when a 21pixel wide slit is applied. This width corresponds to about 3 times the diffraction-limited element. For strongly scattering samples, a slightly wider slit aperture can reduce the speckle noise without sacrificing the contrast and resolutions. If we apply much wider slit, the speckle noise will be reduced further but a significant reduction in contrast will be incurred, as shown in Fig. 6.8(c) where a slit width of 210 pixels are applied. Also the optical sectioning will be compromised. The distorted images are shown in Figs. 6.8(d)-6.8(f). The aberration significantly spread the line image as illustrated in Fig. 6.8(d). The resultant confocal image with a slit width of 21 pixels is shown in Fig. 6.8(e). This confocal image is the best while we move the center of numerical slit

through the blurred line image. Increase in the slit leads to stronger cross talk due to the directional spread of the energy of the line image, as shown in Fig. 6.8(f). The corrected line image obtained by taking FT of the corrected optical field at the pupil represented by Fig. 6.8(g) is shown in Fig. 6.8(g). With correction, the width of the line image is almost completely recovered to the level of the aberration-free one. The corresponding confocal image with a numerical slit of 21 pixels is shown in Fig. 6.8(h), which illustrates almost complete recovery of the information compared to the distorted confocal image in Fig. 6.8(e). With a larger slit of 210 pixels, a confocal image with lower speckle is obtained as shown in Fig. 6.8(i) which shows more pronounced improvement compared to Fig. 6.8(f). This is because correction eliminates the strong cross talk due to the directional spread of energy within the slit. This experiment clearly demonstrates the effectiveness of digital adaptive optics line-scanning confocal imaging system. This system does not rely on the hardware pieces of adaptive optics and slit aperture in the conventional line-scanning confocal image system. The flexible setting of the numerical slit can facilitate determination of the optimal slit width according to the nature of the samples and imaging goals. Also this experiment clearly demonstrates that with complex amplitude of the object field, the aberration can be removed if aberration can be obtained.

6.5 Conclusions

In this chapter, we present a full digital adaptive optics line-scanning confocal imaging system. The optical field from each slice of the sample is recorded by a digital hologram. This hologram contains the information from the sample and the aberration of the optical system. This aberration can be measured by a guide star hologram. By numerically removing the aberration from each distorted line hologram, the optical field from each slice of the sample can

be improved and the final confocal image is restored. First, as digital line-scanning confocal imaging system, no hardware slit is used. The numerical slit width can be easily adjusted to achieve the best image in terms of the speckle noise, contrast and resolutions. Mostly importantly, digital adaptive optics is able to remove the hardware pieces and complicated control procedures required by the conventional adaptive optics system. By adopting fiber optics and better mechanical design, this idea is quite promising to become a compact digital adaptive optics laser scanning ophthalmoscope.

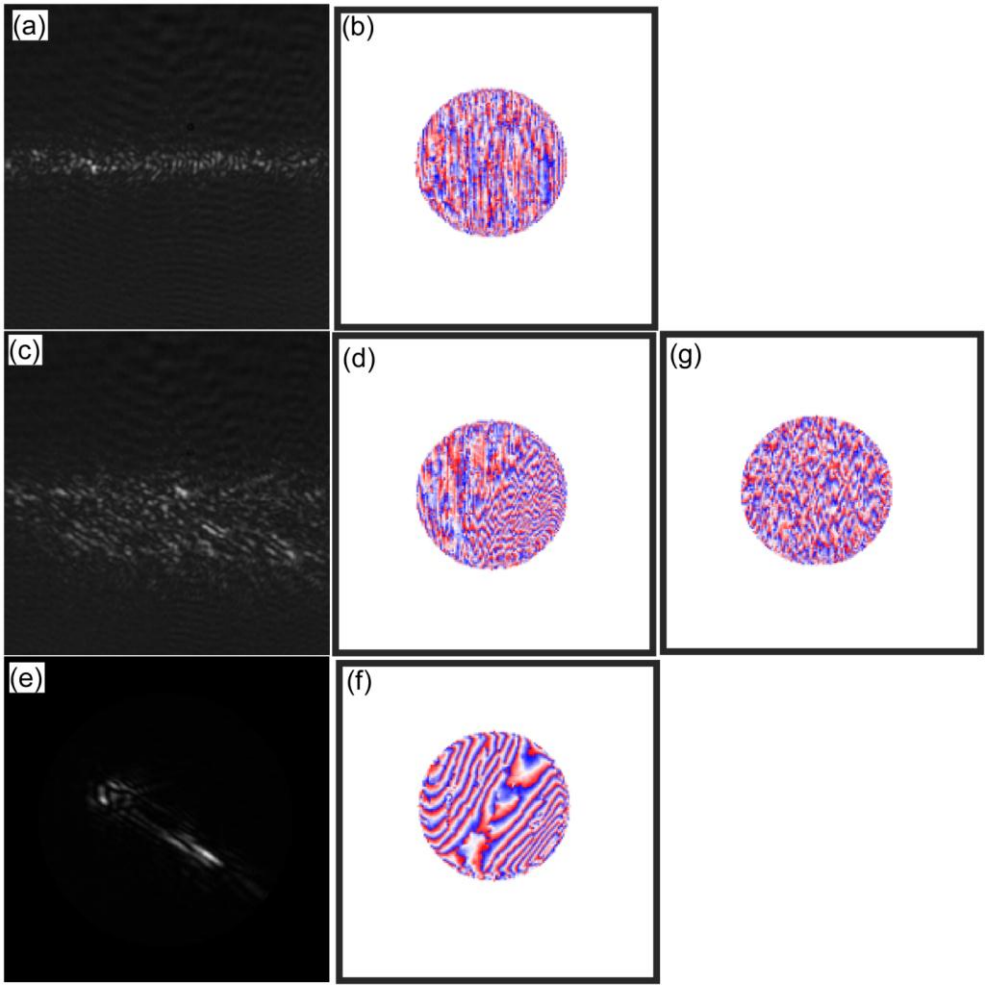

Figure 6.7 Line holograms and guide star holograms. (a) the hologram of one slice of the sample without aberration. (b) the phase distribution at the pupil plane from (a). (c) the hologram recording the distorted optical field of one slice of the sample. (d) the distorted phase distribution at the pupil from (c). (e) guide star hologram. (f) the measured phase aberration introduced by the aberrator. (g) the corrected phase distribution of (d) by subtracting (f) from it.

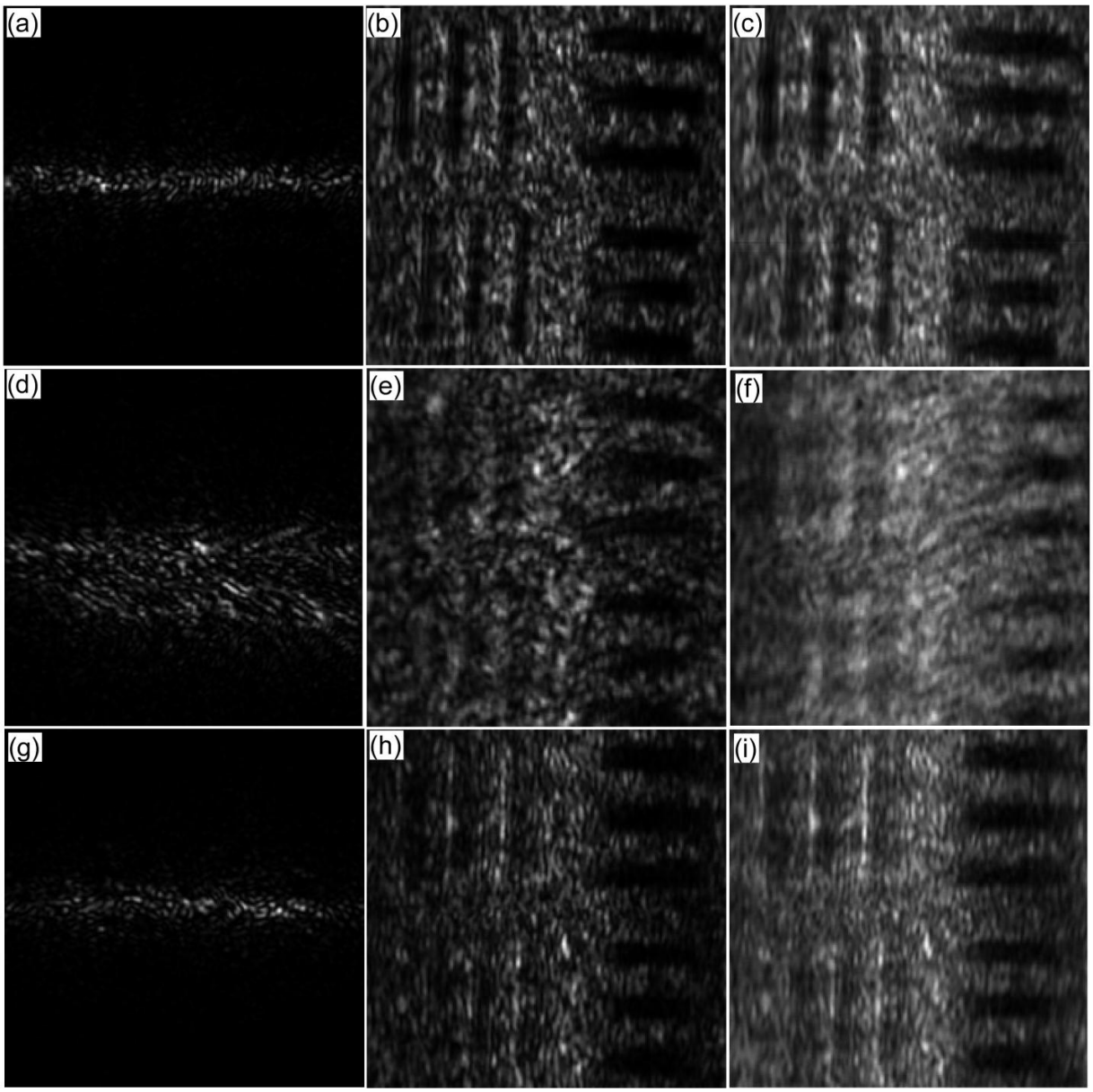

Figure 6.8. Confocal images. (a)–(c) Images without aberrator in place. (a) Line image. (b) Confocal image with a slit width 21 pixels. (c) Confocal image with a slit width 210 pixels. (d)-(f) Images distorted by the aberrator. (d) Line image. (e) Confocal image with a slit width 21 pixels. (f) Confocal image with a slit width 210 pixels. (g)-(h) Corrected images. (g) Line image. (h) Confocal image with a slit width 21 pixels. (i) Confocal image with a slit width 210 pixels.

6.6 References

1. M. Minsky, "Microscopy apparatus," U.S. patent 3,013,467 (December 1961).

2. R. H. Webb, "Confocal optical microscopy," Rep. Prog.Phys.**59**, 427-471(1996).

3. J. B. Pawley, ed. *Handbook of biological confocal microscopy* (Springer, 1995).

4. T. Wilson, ed. *Confocal microscopy* (Academic,1990).

5. T. R. Corle, and G. S. Kino, ed. *Confocal scanning optical microscopy and related imaging systems* (Academic, 1996).

6. K. Im, S. Han, Park, D. Kim, and B. Kim, "Simple high-speed confocal line-scanning microscope," Opt. Express.**13**, 5151-5156(2005).

7. P. J. Dwyer, C. A. DiMarzio, J. M. Zavislan, W. J. Fox, and M. Rajadhyaksha, "Confocal reflectance theta line-scanning microscope for imaging human skin *in vivo*," Opt. Lett. **31,** 942-944 (2006).

8. D. X. Hammer, R. D. Ferguson, T. E. Ustun, C. E. Bigelow, N. V. Iftimia, and R. H. Webb, "Line-scanning laser ophthalmoscope," J. Biomed. Opt. **11**, 041126(2006).

9. P. J. Dwyer, C. A. Dimarzlo, and M. Rajadhyaksha, "Confocal theta line-scanning microscope for imaging human tissues," Appl. Opt. **46**, 1843-1851(2007).

10. M. Mujat, R. D. Ferguson, N. Iftimia, and D. X. Hammer, "Compact adaptive optics ophthalmoscope," Opt. Express **17**, 10242-10258(2009).

11. E. Cuche, P. Marquet, and C. Depeursinge, "Digital holography for quantitative phase-contrast imaging," Opt. Lett. **24**, 291-293 (1999).

12. C. Mann, L. Yu, C. Lo, and M. K. Kim, "High-resolution quantitative phase-contrast microscopy by digital holography," Opt. Express. **13**, 8693-8698(2005).

13. M. K. Kim, "Principles and techniques of digital holographic microscopy," SPIE Reviews **1**, 1-50(2010).

14. C. Liu, and M. K. Kim, "Digital holographic adaptive optics for ocular imaging: proof of principle," Opt. Lett., **36**, 2710(2011).

15. C. Liu, X. Yu, and M.K. Kim, "Fourier transform digital holographic adaptive optics imaging system," Appl. Opt. **51**, 8449-8454(2012).

16. A. S. Goy, and D. Psaltis, "Digital confocal microscope," Opt. Express **20**, 22720-22727(2012).

17. A. S. Goy, M. Unser, and D. Psaltis, "Multiple contrast metrics from the measurements of a digital confocal microscope," Biomed. Opt. Express **4**, 1091-1103(2013).

18. C. Liu, S. Marchesini, and M. K. Kim, "quantitative phase-contrast confocal microscope," Opt. Express **22**, 17830-17839(2014).

Chapter Seven:

Summary and Future Work

7.1 Summary

In this dissertation, we first presented the concept of a new type of adaptive optics (AO) modality based on the principles of digital holography (DH). The proposed digital holographic adaptive optics (DHAO) realizes the phase aberration by a digital hologram and aberration correction by numerical processing, thus eliminating the lenslet array for aberration sensing, deformable mirror for wave corrector and complicated control procedures. In this original DHAO system, the CCD is put at the image plane of the pupil plane of the eye lens. The image of the aberration is obtained by a digital hologram or guide star hologram. The full optical field is captured by a second digital hologram. Because CCD is not at the conjugate plane of the sample, a numerical propagation is necessary to find the image of the sample after the numerical aberration compensation at the CCD plane. Different from the conventional AO system, DHAO is a coherent imaging modality which gives more access to the optical field and allows more freedom in optical system design. In fact, CCD does not have to be put at the image plane of the CCD. This idea was first explored by testing a Fourier Transform DHAO system (FTDHAO). In the FTDHAO, the CCD can directly record the point spread function (PSF) of the system, making it easier to determine the correct guide star hologram. The CCD is also at the image plane of the target. The signal will be stronger than the existing system, especially for the phase aberration sensing. Numerical propagation is not necessary. In the FTDHAO imaging system,

the phase aberration at the eye pupil can be retrieved by the inverse Fourier transform (FT) of the guide star hologram, and the correction takes place at the eye pupil, instead of the CCD plane. The successful demonstration of FTDHAO encourages us to put CCD at an arbitrary diffraction plane in the DHAO system. Through strict theoretical formulation by use of paraxial optical theory, we developed a correction method by correlation for the general optical system to perform the DHAO. In this method, a global quadratic phase term has to be removed before the correction operation. In the formulation, it is quite surprising to find that the defocus term can be naturally eliminated after the correlation operation.

To apply the DHAO to confocal retinal imaging system, we first developed a digital form of line-scanning confocal imaging system. Each line scan is turned into a digital hologram. The complex amplitude of the optical field from each slice of the sample and aberration of the optical system can be retrieved by digital holographic process. This digital line-scanning confocal image absorbs the merits of the line-scanning confocal imaging system and DH. High-contrast intensity images with low coherent noise, and the optical sectioning capability are made available due to the confocality. Phase profiles of the samples become accessible thanks to DH. The quantitative phase map is even better than that from wide field digital holography. We then explored the possibility of applying DHAO to this newly developed digital line-scanning confocal system. We have demonstrated that the phase aberration can be obtained by a guide star hologram in the wide field DHAO systems. We then apply this technique to acquire the aberration at the eye pupil, remove this aberration from the optical fields of the line scans and recover the confocal image. To circumvent the effect of phase aberration on the line illumination, a small collimated laser beam is shone on the cylindrical lens. Thus the image is solely blurred by the second passage. This way, we can clearly demonstrate the effect of DHAO on the digital line-scanning confocal

imaging system. In essence, digital line-scanning confocal imaging system is using coherent point spread function to compensate for the coherent line spread function of the system. Since line-scanning confocal image using spatially coherent light sources has proven an effective imaging tool for retinal imaging, the presented digital adaptive optics line-scanning confocal imaging system is quite promising to become a compact digital adaptive optics laser scanning confocal ophthalmoscope.

7.2 Future Work

DHAO is a coherent imaging modality. For wide-field imaging, the speckle noise is inevitable. I will apply low-coherence light source such as high power LED and degenerate laser to perform wide-field digital holography and test the feasibility of DHAO using low-coherence light sources. I am also interested in extending the imaging capability of DH for scattering tissue imaging. DH has proven an effective method of sensing the aberration in the optical system. Its application in ocular system will be explored in-vivo to eliminate the limitations imposed by the Shack-Hartmann wavefront sensor such as limited dynamic range, and limited sampling pitch. I am more interested in holographic confocal imaging system. It is a digital form of the conventional confocal imaging system and is able to get the quantitative phase information, high-contrast image and low coherence noise. I would like to continue testing the possibility of achieving phase information for tissue imaging at different sections.

Since we have demonstrated the effectiveness of digital adaptive optics line-scanning confocal imaging system which is able to correcting for the aberration in the confocal images without hardware pieces and complicated control procedures required by the conventional adaptive optics laser scanning ophthalmoscope. I will continue to study this imaging modality

and engineer it into compact full digital adaptive optics line-scanning ophthalmoscope.

Appendix A:

List of Publications

Patents

Changgeng Liu, and Myung K. Kim, "Systems and methods for performing quantitative phase-contrast confocal microscopy," patent pending (US provisional patent application: 62/017, 922,2014).

Peer-Reviewed Journal Papers

1. Changgeng Liu, and Myung K. Kim, "Digital adaptive optics line-scanning confocal imaging system," in preparation.

2. Changgeng Liu, Stefano Marchesini, and Myung K. Kim, "Quantitative phase-contrast confocal microscope," Optics Express **22**(15):17830(2014).

3. Xiao Yu, Jisoo Hong, Changgeng Liu, Michael Cross, Donald T. Haynie, and Myung K. Kim, "Four-dimensional motility tracking of biological cells by digital holographic microscopy," Journal of Biomedical Optics **19**(4):045001(2014).

4. Xiao Yu, Jisoo Hong, Changgeng Liu, and Myung K. Kim, "Review of digital holographic microscopy for three-dimensional profiling and tracking," Optical Engineering **53**(11):112306(2014).

5. Changgeng Liu, Xiao Yu, and Myung K. Kim, "Phase correction by correlation in digital holographic adaptive optics," Applied Optics **52**(12):2940(2013).

6. Changgeng Liu, Xiao Yu, and Myung K. Kim, "Fourier Transform Digital Holographic Adaptive Optics Imaging System," Applied Optics **51**(35):8449(2012).

7. Xiao Yu, Michael Cross, Changgeng Liu, David C. Clark, Donald T. Haynie, and Myung K. Kim, "Quantitative imaging and measurement of cell-substrate surface deformation by digital holography," Journal of Modern Optics **9**, 1-8 (2012).

8. Xiao Yu, Michael Cross, Changgeng Liu, David C. Clark, Donald T. Haynie, and Myung K. Kim, "Measurement of the traction force of biological cells by digital holography," Biomed. Opt. Express **3**, 153-159 (2012).

9. Changgeng Liu, and Myung K. Kim, “Digital holographic adaptive optics for ocular imaging: proof of principle,” Optics Letters, **36**(14):2710(2011).

10. Changgeng Liu, Dayong Wang, John Healy, Bryan M. Hennelly, John T. Sheridan, Myung K. Kim, “Digital computation of the complex linear canonical transform”, J. Opt. Soc. Am. **A28**(7):1379(2011).

11. Huacun Cui, Dayong Wang,Yunxin Wang, Changgeng Liu, Yan Li, and Jie Zhao, “Automatic procedure for non-coplanar aberration compensation in lensless Fourier transform digital holography,” Acta. Phys. Sin. **60**(4):044201(2011) (In Chinese).

12. Changgeng Liu, Dayong Wang and Yizhuo Zhang, “Comparison and verification of numerical reconstruction methods in digital holography,” Optical Engineering, **48**(10):105802(2009).

13. Changgeng Liu, Dayong Wang, Yizhuo Zhang., “Derivatives-based autofocus algorithms for the digital holographic imaging,” Chinese Journal of Laser, **36**(11):2989(2009) (In Chinese).

Refereed Conference Papers

1. Changgeng Liu, and Myung K. Kim, “Holographic line-scanning confocal microscope,” Oral presentation at DH&3D imaging meeting in Seattle, DM3B.3(2014).

2. Jisoo Hong, Changgeng Liu, and Myung K Kim, "Applications of incoherent digital holography," invited talk given at BISC'14 (Biomedical imaging and sensing conference), Yokohama, Japan (Apr. 2014).

3. Changgeng Liu, Xiao Yu, Jisoo Hong, and Myung K. Kim, “Image Synthesis for off axis low coherence digital holography,” Poster presentation at Frontier in Optics in Orlando, JW3A.17(2013).

4. Changgeng Liu, Xiao Yu, and Myung K. Kim, “Simulation and Experiments of Fourier Transform Digital Holographic Adaptive Optics,” in Digital Holography and Three-Dimensional Imaging, OSA Techinal Digest (CD) DW2A.18 (2013).

5. Myung K Kim, and Changgeng Liu, “Ophthalmic adaptive optics by digital holography,” SPIE BiOS (San Francisco, CA, Feb. 2013).

6. Xiao Yu, Changgeng Liu, and Myung K. Kim, "Four dimensional motility tracking of biological cells by digital holographic microscopy," in Digital Holography and Three-Dimensional Imaging, OSA Techinal Digest (CD) DM4A.6 (2013).

7. Changgeng Liu, and Myung K. Kim, “In vitro bovine imaging by Digital Holographic Adaptive Optics”, Oral presentation at Frontier in Optics at Rochester , FW5A.2(2012).

8. Changgeng Liu**,** and Myung K. Kim, “Biological imaging by Digital Holographic Adaptive Optics”, OSA: DH conference, JM3A61(2012).

9. Xiao Yu, Changgeng Liu, David C. Clark, and Myung K. Kim, " Quantitative imaging of surface deformation on substrata due to cell motility by digital holography," in Digital Holography and Three-Dimensional Imaging, OSA Techinal Digest (CD) (Optical Society of America, 2012).

10. Xiao Yu, Michael Cross, Changgeng Liu, David C Clark, Donald T Haynie, and Myung K Kim, “Quantitative imaging and measurement of cell-substrate surface deformation by digital holography,” OSA Frontiers in Optics (Rochester, NY, Oct. 2012).

11. Changgeng Liu**,** Myung K. Kim, Xiao Yu, and David C. Clark, “Digital Holographic Adaptive Optics for Retinal Imaging”, OSA: DH conference, DWC37(2011).

12. Xiao Yu, Changgeng Liu, David C. Clark, and Myung K. Kim, "Measurement of Young’s Modulus of Polyacrylamide Gel by Digital Holography," in Digital Holography and Three-Dimensional Imaging, OSA Techinal Digest (CD) (2011).

13. Changgeng Liu, Dayong Wang, Yan Li, “The Effect of Sampling on FFT-Based Direct Integration Method in Digital Holography,” Proc.of SPIE, 7513:1Q-1(2009).

About the Author

Changgeng Liu was born in November 1985 in Hunan province China. He obtained Bachelor of Science degree in applied physics with a concentration in optoelectronics and optical communication from Beijing University of technology in 2007. He was recommended to the graduate school of the same university in the same year. He obtained Master of Science degree in Physics with a concentration in Optics in 2010 from the same university. He then joined University of South Florida in the fall of 2010 and continued his interests in physical optics, particularly digital holography and its applications, under the direction of Prof. Myung K. Kim.

Changgeng Liu focused on research in the theory and algorithms of optical information processing during his graduate study in Beijing University of Technology. During this period, he published several papers in peer-reviewed journals on the numerical modeling of wave propagation in free space and autofocus algorithms for digital holographic imaging. His thesis for the Master of Science degree was selected as one of the outstanding theses of the university. Under the supervision of Prof. Myung K. Kim, he became more devoted to experimental study of digital holography, especially the development of a new adaptive optics system for wide-field and confocal ophthalmoscopes. It is this period when he became very interested in solving the real problems in biomedical optical imaging and physiological optics. His interest in computational optics won him an opportunity of studying X-ray coherent imaging in Lawrence Berkeley National Laboratory in the summer of 2013 under the supervision of Dr. Stefano Marchesini.